NAS 1.29/3-2:95-09

NASA Tech Briefs

National Aeronautics and Space Administration



Electronic Components and Circuits



Electronic Systems



Physical Sciences



Materials



Computer Programs



Mechanics



Machinery



Fabrication Technology



Mathematics and Information Sciences



Life Sciences

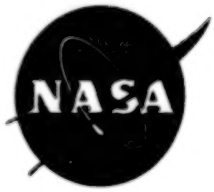
95-09

September 1995

COMPLETED

BLANK PAGE

National Aeronautics and
Space Administration



INTRODUCTION

Tech Briefs are short announcements of new technology derived from the research and development activities of the National Aeronautics and Space Administration. These Briefs emphasize information considered likely to be transferable across industrial, regional, or disciplinary lines and are issued to encourage commercial application.

Availability of NASA Tech Briefs and TSP's

Distribution of NASA Tech Briefs, a monthly periodical publication, is limited to engineers in U.S. Industry and to other domestic technology transfer agents. Requests for individual Tech Briefs or for Technical Support Packages (TSP's) announced herein should be addressed to

NASA Center for AeroSpace Information
Technology Transfer Office
800 Elkridge Landing Rd.
Linthicum Heights, MD 21090-2934
Telephone No. (301) 621-0245

Please reference the three-letter, five-digit control number located at the end of each Tech Brief. Information on NASA's Technology Utilization Program, its documents, and services is also available at the same facility.

Technology Utilization Officers and Patent Counsels are located at NASA field installations to provide technology-transfer access to industrial users. Inquiries can be made by writing to NASA field installations listed below.

Technology Utilization Officers and Patent Counsels

Ames Research Center
Technology Utilization Officer
Mail Code 223-3
Moffett Field, CA 94035

Patent Counsel
Mail Code 200-11
Moffett Field, CA 94035

Goddard Space Flight Center
Technology Utilization Officer
Mail Code 702-1
Greenbelt, MD 20771

Patent Counsel
Mail Code 204
Greenbelt, MD 20771

Lyndon B. Johnson Space Center
Technology Utilization Officer
Mail Code IC-4
Houston, TX 77058

Patent Counsel
Mail Code AL3
Houston, TX 77058

John F. Kennedy Space Center
Technology Utilization Officer
Mail Stop PT-PMO-A
Kennedy Space Center, FL 32899

Patent Counsel
Mail Code PT-PAT
Kennedy Space Center, FL 32899

Langley Research Center
Technology Utilization Officer
Mail Stop 143
Hampton, VA 23665

Patent Counsel
Mail Code 279
Hampton, VA 23665

Lewis Research Center
Technology Utilization Officer
Mail Stop 7-3
21000 Brookpark Road
Cleveland, OH 44135

Patent Counsel
Mail Code LE-LAW
21000 Brookpark Road
Cleveland, OH 44135

Jet Propulsion Laboratory
Technology Utilization Officer
Mail Stop 156-211
4800 Oak Grove Drive
Pasadena, CA 91109

NASA Resident Office-JPL
Technology Utilization Officer
Mail Stop 180-801
4800 Oak Grove Drive
Pasadena, CA 91109

Patent Counsel
Mail Code 180-801
4800 Oak Grove Drive
Pasadena, CA 91109

George C. Marshall Space Flight Center
Technology Utilization Officer
Code AT01
Marshall Space Flight Center, AL 35812

Patent Counsel
Mail Code CC01
Marshall Space Flight Center, AL 35812

John C. Stennis Space Center
Technology Utilization Officer
Code HA-30
Stennis Space Center, MS 39529

NASA Headquarters
Technology Utilization Officer
Code CU
Washington, DC 20546

Assistant General Counsel for Patent Matters
Code GP
Washington, DC 20546

Dryden Flight Research Center
Technology Utilization Officer
M/S D21-31
Bldg. 4832 Whse 7
Lilly Dr.
Edwards, CA 93523

NASA TechBriefs

National Aeronautics and Space Administration

September 1995
95-09

5 Electronic Components and Circuits

13 Electronic Systems

21 Physical Sciences

29 Materials

39 Computer Programs

45 Mechanics

53 Machinery

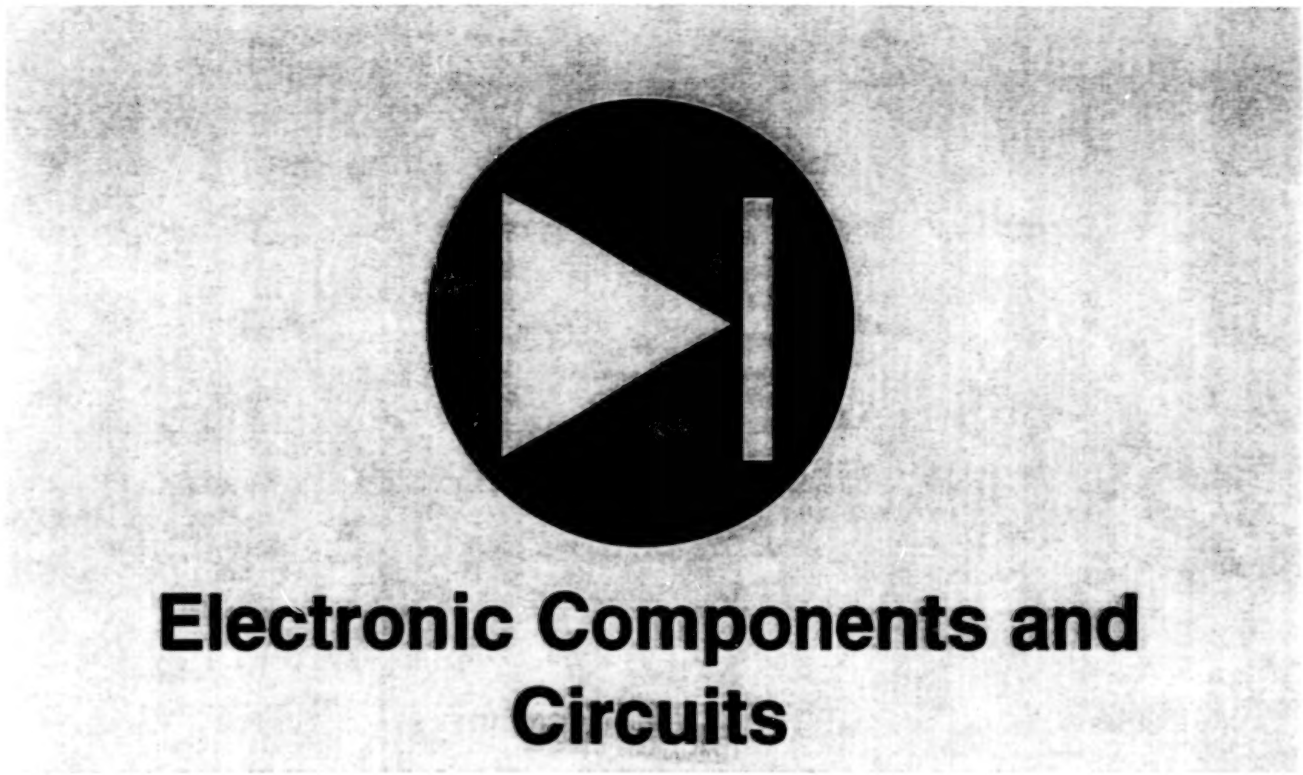
59 Fabrication Technology

63 Mathematics and Information Sciences

69 Life Sciences

This document was prepared under the sponsorship of the National Aeronautics and Space Administration. Neither the United States Government nor any person acting on behalf of the United States Government assumes any liability resulting from the use of the information contained in this document, or warrants that such use will be free from privately owned rights.

BLANK PAGE



Electronic Components and Circuits

Hardware, Techniques, and Processes

7 Embedded Temper ture-Change Sensors
7 Gas-Sensing Flip Circuits
8 Miniature Radioiso Power Source
9 Electronic Ambient-Temperature Recorder
10 Ultra-High-Density Ferroelectric Memories
10 Circular Metal/Semiconductor/Metal Photodetectors
11 Long-Wavelength-Infrared Hot-Electron Transistor

Books and Reports

12 Developing Low-Noise GaAs JFETs for Cryogenic Operation

BLANK PAGE

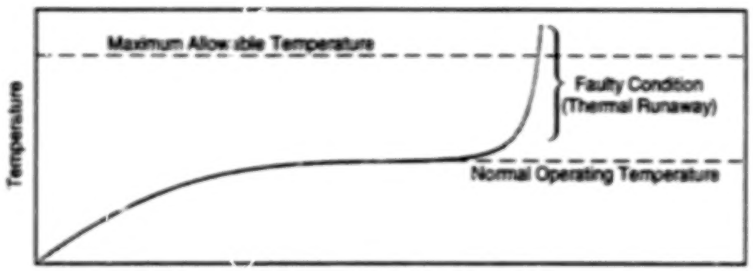
Embedded Temperature-Change Sensors

These sensors could help to prevent overheating of electronic components.

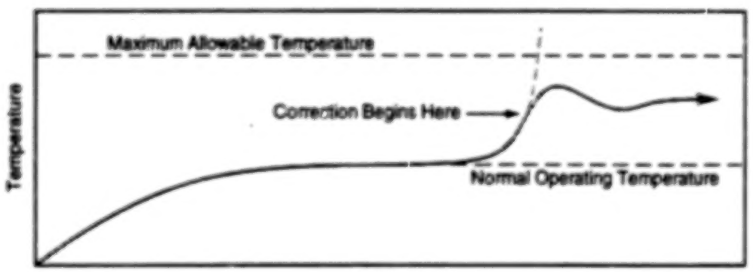
NASA's Jet Propulsion Laboratory, Pasadena, California

Transducers sensitive to rates of change of temperature would be embedded in integrated circuits and discrete electronic components that could be damaged by overheating, according to a proposal. These temperature-change sensors would be used to detect the onset of rapid heating and to trigger shutoffs of power or other corrective actions before temperatures could rise beyond safe limits (see figure). In comparison with older electronic temperature sensors that operate at the system and circuit-board levels, these sensors would respond faster and more reliably to incipient overheating because they would be in direct thermal contact with the vulnerable circuit elements.

The proposed sensors would be low-thermal-inertia, microscopic capacitors, the dielectric layers of which would be thin films of such perovskite materials as lead lanthanum zirconate titanate. These materials are ferroelectric and they exhibit the pyroelectric effect, meaning that a capacitor made with such a material generates a voltage proportional to the rate of change of temperature. The temperature-change sensors and the associated corrective or safety-shutdown circuitry could be fabricated directly on silicon integrated-circuit chips, along with the circuits to be protected against overheating: the integration of the sensing and protective circuitry with the other circuitry should result in a significant reduction in the overall area and power consumption of integrated circuits.



THERMAL RUNAWAY IN ABSENCE OF CORRECTION



THERMAL RUNAWAY STOPPED BY CORRECTION IN RESPONSE TO INITIAL TEMPERATURE RISE

Thermal Runaway in a typical power semiconductor device is a regenerative self-heating effect that can quickly lead to overheating and destructive loss if not interrupted. A temperature-change sensor embedded in the device would respond to the initial temperature rise by generating a signal that would trigger corrective action to prevent damage to the device.

This work was done by Sarita Thakoor, Anil Thakoor, and Dan Kamman of Caltech for **NASA's Jet Propulsion Laboratory**. *Further information is contained in a TSP [see page 1].*

In accordance with Public Law 96-517, the contractor has elected to retain title to this invention. Inquiries concerning rights for its commercial use should be addressed to

William T. Callaghan, Manager
Technology Commercialization
JPL-301-350
4800 Oak Grove Drive
Pasadena, CA 91109

Refer to NPO-19405, volume and number of this NASA Tech Briefs *issue, and the page number.*

Gas-Sensing Flip-Flop Circuits

The voltages of metastable states would vary with exposures of gas-sensitive resistors.

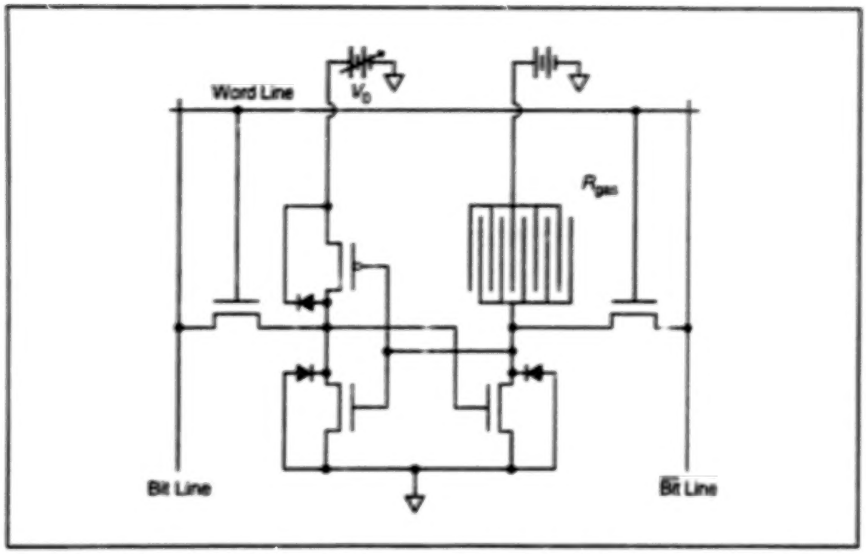
NASA's Jet Propulsion Laboratory, Pasadena, California

Gas-sensing integrated circuits that consist largely of modified static random-access memories (SRAMs) are undergoing development, building on experience gained in the use of modified SRAMs as radiation sensors. Each SRAM memory cell includes a flip-flop circuit; these sensors exploit a metastable state that lies between the two stable states (corresponding to binary logic states) of a flip-flop circuit.

The operation of a gas sensor of this type is based on the fact that the voltage of the metastable state at a suitably chosen node of a flip-flop circuit depends on the value of a resistor in the circuit. This resistor could be designed and fabricated so that its resistance would vary with the amount of a selected gas that it had absorbed or adsorbed from the atmosphere. Inasmuch as the absorbed or adsorbed amount would be related to the concentration of the gas in the atmosphere, the voltage of the metastable state would be indicative of this concentration.

A gas-sensing resistor could be fabricated as a pair of interdigitated metal electrodes in contact with a film of sensing material. Candidate sensing materials include doped tin dioxide and both metal-substituted and metal-free phthalocyanines. The electronic properties of these materials have been well characterized; these materials have been found to be suitable for detection of, and discrimination among, a number of gas species, including O_2, CO, CO_2, CH_4, NO, NO_2, H_2O, NH_3, and N_2H_4.

The figure shows a typical complementary metal oxide/semiconductor (CMOS) modified SRAM cell designed according to this concept. The gas-sensing resistor



The Value of R_{gas} Would Vary with the amount of gas it had absorbed or adsorbed, giving rise to a corresponding variation in the value of V_0 at which the logic state of the circuit would flip spontaneously.

(R_{gas}) would be connected between one of the inverters of the flip-flop and a power supply of constant voltage V_{DD}. The other inverter would be connected to a source of variable offset voltage (V_0). The voltage of the metastable state would be determined by varying and measuring V_0 and noting the value of V_0 at which the circuit flipped spontaneously from one logic state to another.

In principle, a gas sensor could contain a single flip-flop circuit. However, the use of a SRAM instead of a single flip-flop would make it possible to take advantage of the statistical distribution of metastable-state voltages among the numerous memory cells. This would be accomplished by operating in either of two modes. In one mode, V_0 would be varied to obtain a spontaneous-flip curve (a plot of the number of cells that have flipped as V_0 was lowered from an initial value to a present value). The parameters of the spontaneous-flip curve would depend on the statistical distribution of R_{gas} values and of other circuit parameters; the parameters of the spontaneous-flip curve could therefore be related to the concentration of gas via the dependence of the R_{gas} values on this concentration. The other operating mode would be based on similar concepts, but in this mode, V_0 would be held constant and the number of flipped cells would be counted and related to the concentration of gas.

Another advantage of the use of modified CMOS SRAMs is that signal-detecting circuits and analog-to-digital converters can be incorporated into the flip-flop or memory cells to provide digital outputs that can be utilized readily by a computer. Furthermore, the modified RAMs can be made by conventional CMOS fabrication techniques, with simple addition of the gas-sensing resistors.

This work was done by Martin G. Buehler, Brent R. Blaes, Roger Williams, and Margaret A. Ryan of Caltech for **NASA's Jet Propulsion Laboratory**. *Further information is contained in a TSP [see page 1].*

NPO-19389

Miniature Radioisotope Power Source

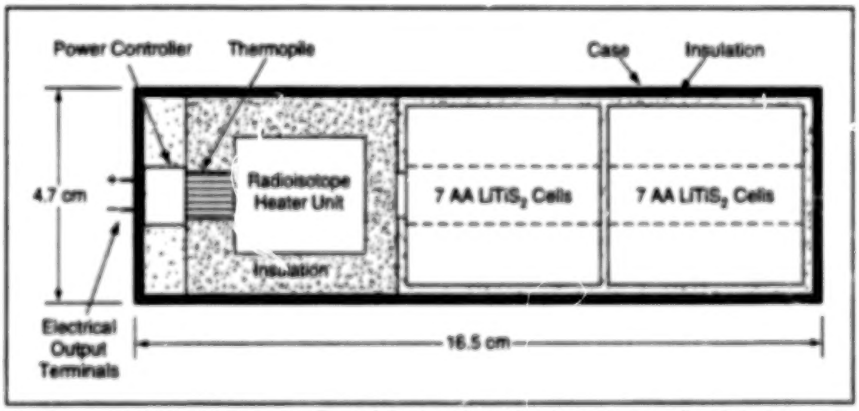
About the size of a small flashlight, a proposed unit could power small instruments for years.

NASA's Jet Propulsion Laboratory, Pasadena, California

A proposed miniature power source would generate electricity for years without addition of fuel or dependence on sunlight. Called the powerstick, it would be relatively inexpensive, lightweight, and rugged in comparison with other radioisotope thermoelectric generators that have been designed in recent years. The powerstick could supply power to small vehicles or scientific instruments in remote locations on Earth or in outer space. Some envisioned uses include Mars miniature rovers and monitoring equipment for toxic or nuclear storage sites.

The powerstick consists of a radioisotope heater unit, a thermopile made of state-of-the-art thermoelectric material, a rechargeable battery, and control circuitry (see figure). During a full discharge from an initial full charge, the battery could supply 28 W-h of energy (1 A-h at 28 V). The total mass of the power stick would be approximately 380 grams.

The radioisotope heater unit is a spot heater, produced by the U.S. Department of Energy, that contains a relatively small amount of radioisotope fuel and is commonly used on spacecraft. This unit provides 1 W of thermal power. Multilayer thermal insulation would direct most of the heat flux toward the thermopile, battery, and control circuitry, where it would not only supply energy for thermoelectric conversion, but would also maintain the battery and circuitry at the proper operating temperature. The thermopile would convert some of this thermal power to 40 mW of continuous electric power, which would be used to trickle-charge the battery. It would take about one month to fully recharge the battery after full discharge.



The Powerstick Would Generate Electricity from heat developed in a small radioisotope unit.

The thermopile consists of about 1000 bismuth telluride legs that are 3 cm long and have a square cross section of 1/3 mm on a side. The battery in the power-

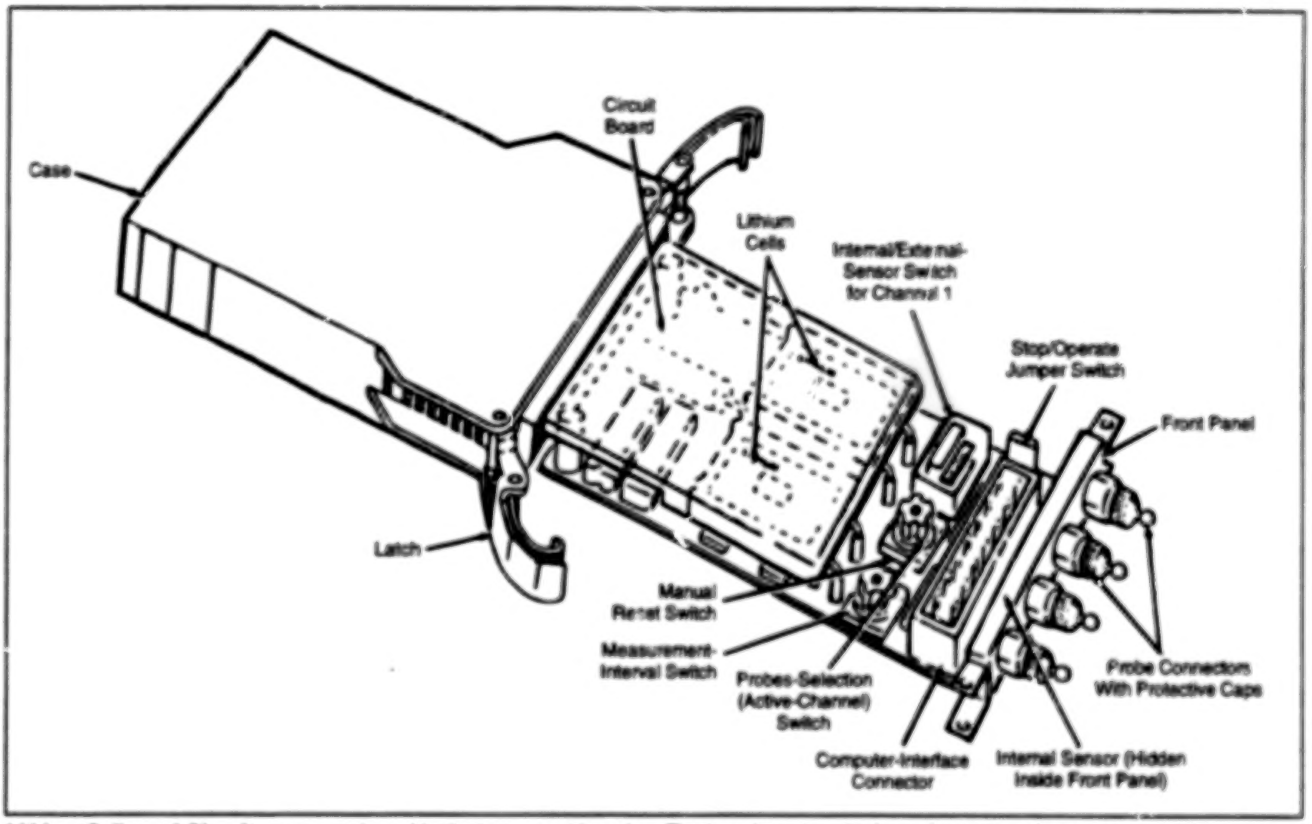
stick would consist of fourteen $LiTiS_2$ rechargeable cells of standard AA size, characterized by low self-discharge rate. The energy densities of these cells are 120 W-h/kg — about four times that of nickel/cadmium cells. The 28-V output of the battery could be downregulated by a microchip regulator or a dc-dc converter to various lesser voltages with an efficiency of about 85 percent.

This work was done by Artur B. Chmielewski of Caltech for **NASA's Jet Propulsion Laboratory**. *Further information is contained in a TSP [see page 1].*
NPO-19339

Electronic Ambient-Temperature Recorder

Data are logged in an electronic memory for later display on a computer.

Ames Research Center, Moffett Field, California



Lithium Cells and Circuitry are on a board in the instrument housing. The board can be withdrawn for setting of switches. Probe connectors are accessible from the front of the housing.

An electronic temperature-recording unit stores data in its internal memory for later readout. It records temperatures from -40 to +60 °C at intervals that range from 1.875 to 15 minutes. With all four of its data channels operating at 1.875-minute intervals, the recorder can store at least 10 days' data. For only one channel at 15-minute intervals, the capacity extends to up to 342 days' data. Two lithium cells can supply power to the unit for about 2 years (although the conservatively rated replacement interval is 1 year).

The unit was developed for recording temperatures of instruments and life-science experiments on satellites, the space shuttle, and high-altitude aircraft. It is adaptable to such terrestrial uses as recording temperatures of perishable goods during transportation and of other systems or processes over long times. It can be placed directly in the environment it is to monitor.

The unit (see figure) is light and compact: it weighs 135 grams and is housed in a 23- by 41- by 86-millimeter case. Connectors on the front of the housing accept as many as four temperature probes, one for each data channel. In addition, an internal sensor measures the ambient temperature; it can be used as input for channel 1. Switches inside the case are used to select the measurement interval and the number of active channels.

Temperature readings are digitized to 8 bits and stored in a 32 KB random-access memory (RAM). The data are read out by a desktop computer, which processes them for display in tabular and graphical form. The RAM is then reset for further measurements.

In addition to the RAM, the unit contains an oscillator/counter timing section, an input analog section, and an analog-to-digital converter (ADC). The major components of these sections are low-power complementary metal oxide/semiconductor (CMOS) integrated circuits. To conserve energy, the input analog section and the ADC, which draw 7 mA, are switched on only during measurement. The other ICs and the RAM draw about 30 μA in standby mode between measurements.

The measurement temperature range can be changed by changing offset and feedback resistors. The narrower the range, the finer the resolution. For the design range, which is 100 °C wide, the resolution is 0.4 °C.

This work was done by Larry Russell and William Berrows of **Ames Research Center**. *Further information is contained in a TSP [see page 1].*
ARC-13220

Ultra-High-Density Ferroelectric Memories

Features would include fast input and output via optical fibers.

NASA's Jet Propulsion Laboratory, Pasadena, California

Memory devices of a proposed type would include thin ferroelectric films in which data would be stored in the form of electric polarization. Assuming that one datum could be stored in a region as small as a polarization domain, the sizes of such domains would impose the upper limits on achievable storage densities. These limits would approach 1 terabit/cm^2 in all-optical versions of these ferroelectric memories and would exceed 1 gigabit/cm^2 in optoelectronic versions. These memories are expected to exhibit operational lives of about 10 years, input/output times of about 10 ns, and fatigue lives of about 10^{13} cycles.

In an all-optical version, both writing and readout would be performed at high speed by use of beams of light directed through optical fibers to the ferroelectric film. The small diameters of the fibers and the near-field optical effects at their tips would provide the resolution needed to achieve high densities in both writing and reading data. On the basis of previous experiments in near-field fiber-optic illumination and readout, it appears that the resolution of a readout beam could be as fine as 12 nm.

Writing would be done at wavelengths corresponding to photon energies greater than the bandgap of the ferroelectric material. Writing would rely on changes of the index of refraction of the ferroelectric material, which would be birefringent. This writing process would consume much less energy than is consumed in other techniques of near-field magneto-optical recording. Thus, a memory of this type would consume less power.

The polarization of any given domain produced by the writing process would affect the properties of the light reflected from that domain. Readout would be effected at wavelengths corresponding to photon energies less than the bandgap of the ferroelectric material. Thus, readout would be nondestructive; that is, it would not alter the polarization of the spot illuminated by the readout beam.

This work was done by Sarita Thakoor of Caltech for **NASA's Jet Propulsion Laboratory**. *Further information is contained in a TSP [see page 1].*

In accordance with Public Law 96-517, the contractor has elected to retain title to this invention. Inquiries concerning rights for its commercial use should be addressed to

William T. Callaghan, Manager
Technology Commercialization
JPL-301-350
4800 Oak Grove Drive
Pasadena, CA 91109

Refer to NPO-19265, volume and number of this NASA Tech Briefs *issue, and the page number.*

Circular Metal/Semiconductor/Metal Photodetectors

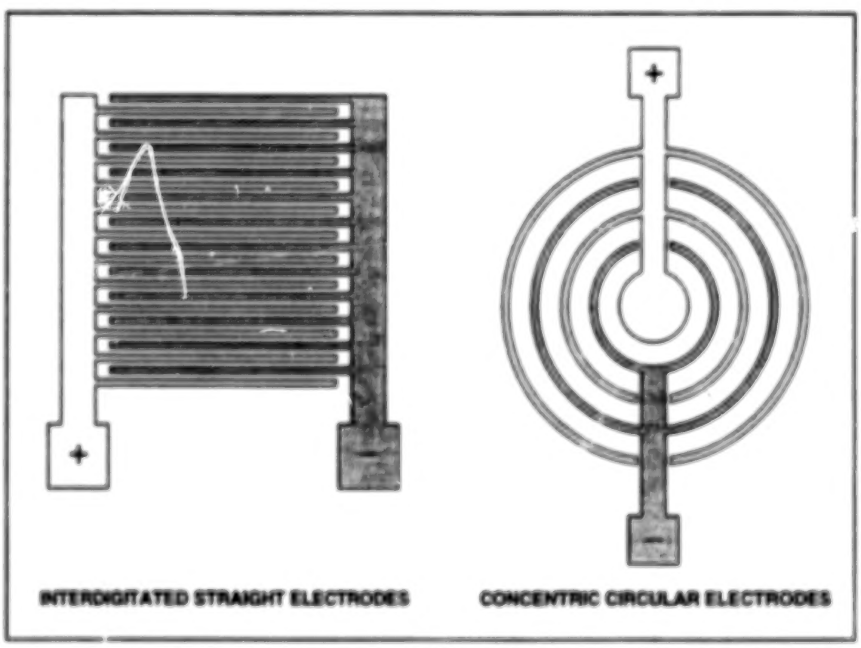
Response times should be smaller and shorter, and breakdown voltages should be larger.

Langley Research Center, Hampton, Virginia

Metal/semiconductor/metal (MSM) photodetectors with multiple concentric circular electrodes are being developed. Some of the electrical characteristics of these devices are expected to be superior to those of older MSM photodetectors that contain interdigitated straight electrodes.

Of the possible circular-electrode configurations, the split-ring configuration shown in the figure is easiest to fabricate. Theoretical analysis indicates that the size of the central disk is critical: the disk must be large enough to keep the breakdown voltage high, but not so large as to shadow a large area of the semiconductor and thereby decrease quantum efficiency. An alternative configuration of two intertwining spiral electrodes has also been proposed, but found to be undesirable.

In comparison with interdigitated straight electrodes, the concentric circular electrodes are expected to provide an improved electric-field configuration that should enable these devices to withstand higher breakdown voltages and to exhibit shorter response times if a satisfactory process can be developed that avoids the need for the split-ring configuration. The capacitance of a typical concentric-circular-electrode device is expected to be about 30 percent lower than that of a comparable straight-interdigitated-electrode device.



Concentric Circular Electrodes are expected to provide an improved electric-field configuration, with lower interelectrode capacitance and higher breakdown voltage than are possible with interdigitated straight electrodes of comparable dimensions.

The decrease in capacitance allows greater signal-detection bandwidth. This would be an important advantage in fiber-optic telecommunication systems, in

which photodetectors are the central components in receiver circuits. Increasing the bandwidth of such a photodetector would enable the receiver to handle a larger number of channels or an increased information rate in each channel.

Another advantage of the circular photodetector pattern is that it would match the circular shape of the cross sections of the light beams from many optical sources. With appropriate choice of wavelength of the optics used to focus light onto a photodetector and of the electrode spacing in the photodetector, it should be possible to locate the maximum-brightness parts of the diffraction pattern in the spaces between the electrodes to maximize the utilization of light, thereby maximizing the output of the photodetector.

This work was done by James A. McAdoo of **Langley Research Center**; *Elias Towe and William L. Bishop of the University of Virginia; and Liang-Guo Wang of the College of William and Mary. No further documentation is available.*

This invention is owned by NASA, and a patent application has been filed. Inquiries concerning nonexclusive or exclusive license for its commercial development should be addressed to the Patent Counsel, Langley Research Center [see page 1]. Refer to LAR-15172.

Long-Wavelength-Infrared Hot-Electron Transistor

Dark current is reduced by an energy-discriminating quantum filter.

NASA's Jet Propulsion Laboratory, Pasadena, California

The very long-wavelength-infrared hot-electron transistor has been developed at NASA's Jet Propulsion Laboratory. This device detects photons at wavelengths around 16 μm. It comprises a photodetector integrated with an energy-discriminating quantum filter in a multiple-quantum-well structure (see Figure 1). The device is made of variously doped and undoped layers of GaAs (quantum wells) and $Al_xGa_{1-x}As$ (the barriers between the wells).

In this transistor, a bound-to-continuum GaAs/$Al_xGa_{1-x}As$ multiple-quantum-well infrared photodetector (QWIP) serves as a photosensitive emitter. A wide quantum well serves as the base, and there is a thick barrier between the base and the collector. The combination of this barrier and the base quantum well acts as an energy-discriminating filter: electrons with higher energies pass through this filter to the collector, while those with lower energies are blocked and are diverted from the output-current path through the base contact.

The energy-discriminating filter solves one of the problems that arises in the use of QWIPs; namely, how to reduce dark current, which is relatively large and thus adversely affects performance. In developing the present device, it was found by a combination of theory and experiment that at operating temperatures below approximately 50 K, the dark current in a QWIP is dominated by quantum-mechanical tunneling. More specifically, it was found that thermionic contribution to the dark current in this temperature range is less than the contribution of quantum-mechanical tunneling (including both thermionically assisted tunneling and sequential tunneling through all of the quantum wells). It was also found that the conduction-

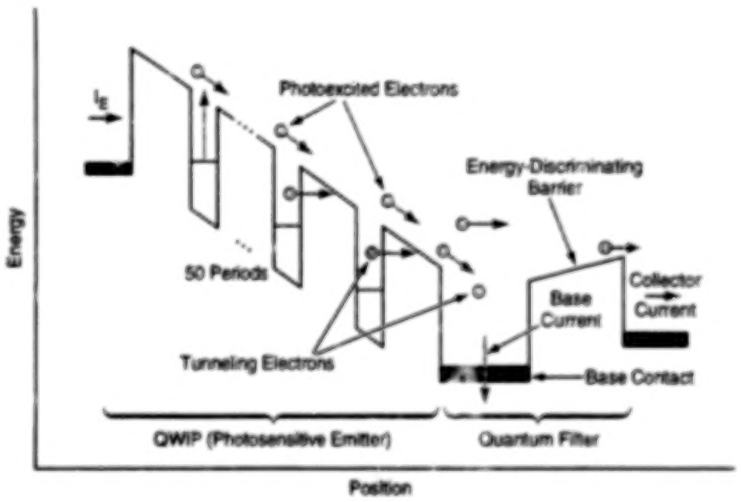


Figure 1. This **Conduction-Band Energy Diagram** illustrates the multiple-quantum-well structure. The quantum filter enhances performance by diverting low-energy electrons that contribute to dark current.

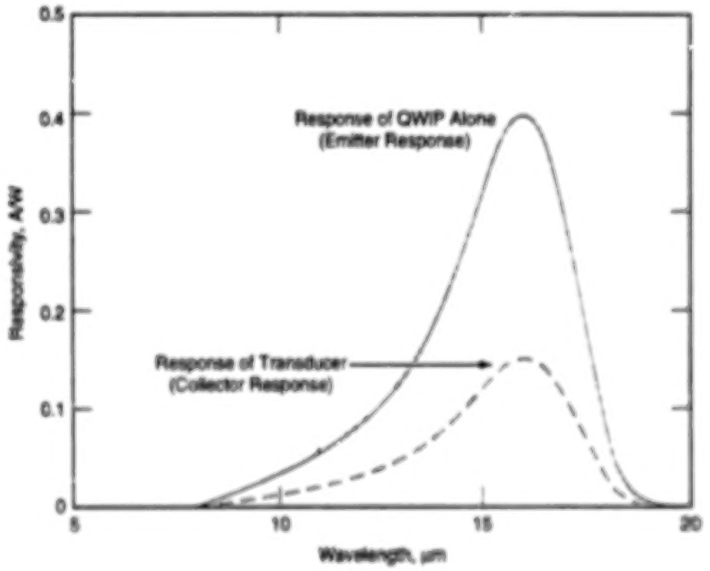


Figure 2. These **Spectral Response Curves** were obtained at a temperature of 60 K with the base and collector contacts grounded and the emitter biased at −1 V.

band electrons that participate in the tunneling current have energies less than those of the photoelectrons. Thus, an energy-discriminating filter that could prevent the lower-energy tunneling electrons from reaching the collector could reduce the output dark current significantly in a QWIP operating in this temperature range.

The present device was grown on a semi-insulating GaAs substrate by molecular-beam epitaxy. A heavily doped (10^{18} cm^{-3}) layer of GaAs 1 μm thick was deposited as the emitter contact. This was followed by a 50-period multiple-quantum-well region of 65-Å-thick doped (5×10^{17} cm^{-3}) GaAs well layers alternating with 500-Å-thick undoped $Al_{0.11}Ga_{0.89}As$ barrier layers. Next, a base-contact layer doped to 3×10^{17} cm^{-3} was grown 500 Å thick. On the base-contact layer, an energy-discriminating barrier layer of undoped $Al_{0.11}Ga_{0.89}As$ was grown 2,000 Å thick. A top collector-contact layer of GaAs was deposited to a thickness of 0.5 μm.

In tests, the device was cooled and back-illuminated at various wavelengths through a 45° polished facet, while its electrical response was measured. Figure 2 shows emitter and collector responsivity spectra measured at a temperature of 60 K. The detectivity was found to increase dramatically with temperature, reaching 10^{12} $cm \cdot Hz^{1/2}/W$ at 25 K, and higher at lower temperatures. In contrast, the detectivities of HgCdTe detectors become saturated as temperature decreases.

This work was done by Sarath D. Gunapala, John K. Liu, Jin S. Park, and True-Lon Lin of Caltech for **NASA's Jet Propulsion Laboratory**. *Further information is contained in a TSP [see page 1].*
NPO-19305

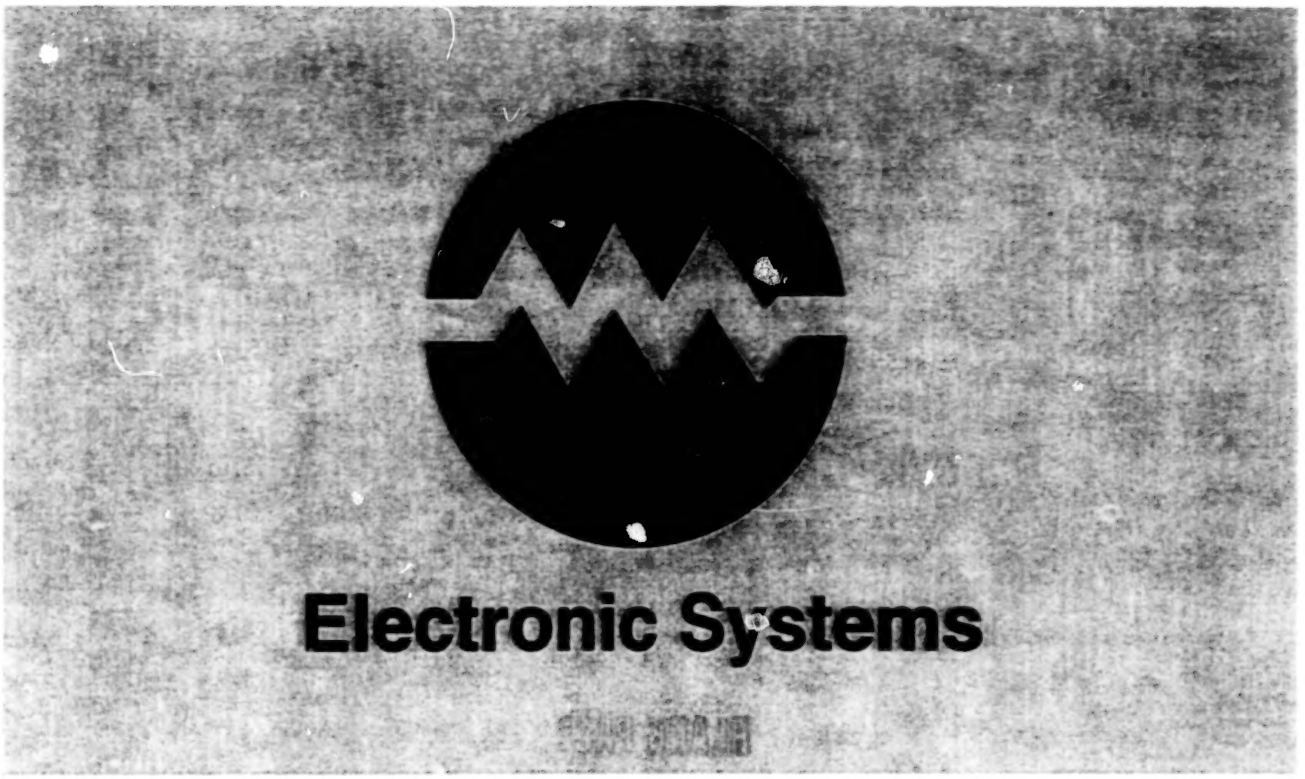
Books and Reports

Developing Low-Noise GaAs JFETs for Cryogenic Operation

Basic physical principles and development goals are outlined.

A report discusses aspects of an effort to develop low-noise, low-gate-leakage gallium arsenide-based junction field-effect transistors (JFETs) for operation at a temperature of about 4 K as readout amplifiers and multiplexing devices for infrared-imaging devices. These transistors are needed to replace silicon transistors, which are relatively noisy at 4 K. The report briefly discusses the basic physical principles of JFETs and describes a continuing process of optimization of the designs of GaAs JFETs for cryogenic operation. In this process, the design parameters (geometry and doping concentrations) of GaAs JFETs in small-scale integrated infrared-imager readout circuits are varied iteratively in response to measurements of their noise levels and leakage currents at 4 K. The iterations will be continued until the lowest noise and leakage currents are obtained and fabrication processes that can implement the low-noise designs repeatably can be found. At the time of the report, the development effort had reached the state of the prior art and was poised to go beyond it.

This work was done by Thomas J. Cunningham of Caltech for **NASA's Jet Propulsion Laboratory**. *To obtain a copy of the report, "Gallium Arsenide Junction Field-Effect Transistors for Deep Cryogenic Applications," see TSP's [page 1].*
NPO-19417



Hardware, Techniques, and Processes

15 VLSI Processor for Vector Quantization
16 Effect of Transition Density on Performance of a DTTL
17 Infrared/Ultrasonic Position-Measuring System

Books and Reports

18 Evaluation of Vibration-Monitoring Gear-Diagnostic System
18 Comparison of Full-Spectrum and Complex-Symbol Combining

BLANK PAGE

VLSI Processor for Vector Quantization

Pixel intensities in each kernel are compared simultaneously with all code vectors.

NASA's Jet Propulsion Laboratory, Pasadena, California

A prototype high-performance, low-power, very-large-scale integrated (VLSI) circuit is designed to perform compression of image data by the vector-quantization method. The circuit contains relatively simple analog computational cells that operate on the direct or buffered outputs of photodetectors grouped into blocks in an imaging array, yielding the vector-quantization code word for each such block in sequence. This scheme exploits the parallel-processing nature of the vector-quantization architecture, with a consequent increase in speed over older purely sequential-processing vector-quantization schemes implemented in software.

For the purpose of vector quantization, the photodetectors in the entire imaging array are grouped into nonoverlapping rectangular blocks called kernels. The pixel intensities or outputs of the photodetectors in each kernel are represented collectively by an m-dimensional vector $\mathbf{x} = (x_1, x_2, \ldots x_m)$, where x_i = the intensity of illumination (or an equivalent detector output) in the ith pixel and m is the number of pixels in the kernel. A set of n code vectors ($\mathbf{c}^1$, $\mathbf{c}^2$, . . . $\mathbf{c}^n$) plus a unique index number (code word) that represents each code vector constitutes a "code book."

The basic vector-quantization process is to (a) find the code vector that approximates $\mathbf{x}$ most closely according to some quantitative measure (e.g., a weighted Euclidean distance $d(\mathbf{x}, c)$ m-dimensional space), then (b) transmit the index number of the code vector, then (c) use the code book in reverse at the receiver to reconstruct an approximation of the pixel intensities in the kernel at the receiver. The advantage of vector quantization is that the index number or code word contains fewer bits than does the corresponding full specification of the pixel intensities in the kernel; that is, the image data are compressed for transmission.

In this vector-quantization scheme, the m analog pixel-intensity values in a kernel are presented simultaneously to an $m \times n$ array of computational cells. The cells are arranged (see Figure 1) so that the ith cell in the jth column represents C_j^i, which is the ith component of the jth code vector. Stated somewhat differently, each column in the array represents one of the code vectors.

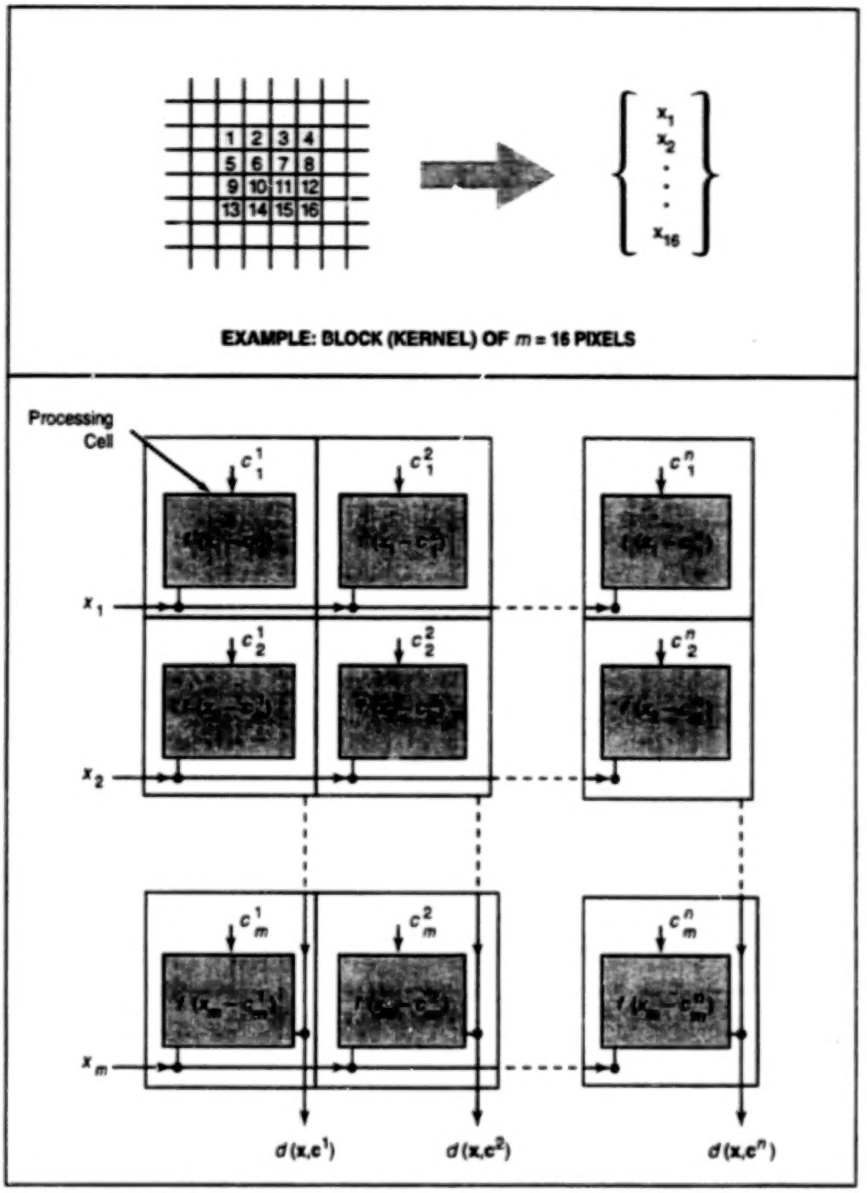


Figure 1. All m Pixel Intensities in a kernel are compared simultaneously with the components of n code vectors.

The output of each cell is a quantity proportional to the disparity between the input actual pixel intensity and the corresponding pixel intensity represented by the code vector of the column in which the cell is located. The outputs of all the cells in a column are added, and the sums from all the columns are compared: whichever column yields the smallest sum (representing the least disparity between the input and code vectors) is selected as the "winner," and the code vector for that column is chosen to represent the pixel intensities in the kernel.

The prototype VLSI circuit (see Figure 2) implements a vector-quantization scheme with m = 16 and n = 256. The circuit is fabricated in complementary metal oxide/semiconductor with feature sizes down to about 2 μm. The circuit is programmable in that a set of code vectors can be stored in the array of cells at

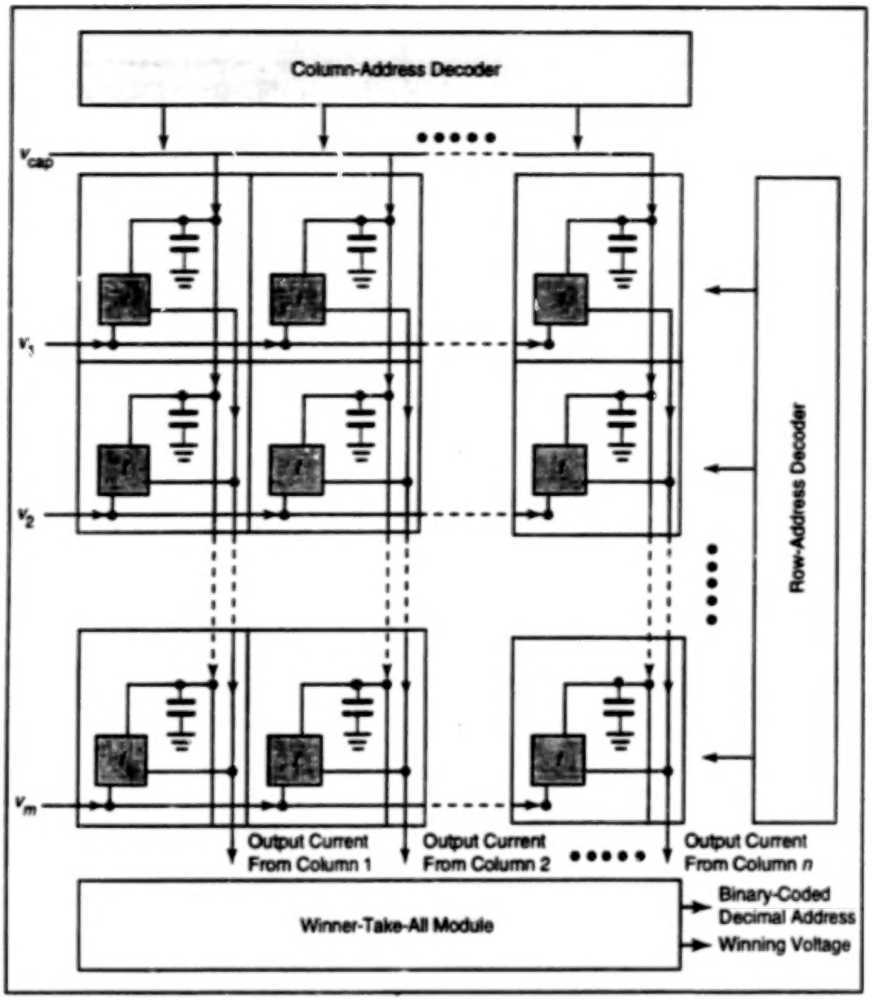


Figure 2. A **Capacitor in Each Processing Cell** stores an analog voltage that represents a component of a code vector represented by the cell.

will. It is also cascadable, so that libraries of several thousand code words can be stored.

An analog voltage that represents the value of C_{ij} in each cell is stored via a capacitor-refresh scheme. The circuit includes an address and data demultiplexer, row- and column-address decoders, capacitor-refresh circuitry, 32 analog input lines, and a winner-take-all module with winner-select output lines. This circuit has been found to compress an image of 512 by 512 pixels in 0.5 second — about 400 times as fast, and with a fraction of the power (milliwatts) and cost of a software implementation on a computer.

This work was done by Raoul Tawel of Caltech for **NASA's Jet Propulsion Laboratory**. *Further information is contained in a TSP [see page 1].*

In accordance with Public Law 96-517, the contractor has elected to retain title to this invention. Inquiries concerning rights for its commercial use should be addressed to

William T. Callaghan, Manager
Technology Commercialization
JPL-301-350
4800 Oak Grove Drive
Pasadena, CA 91109

Refer to NPO-18976, volume and number of this NASA Tech Briefs *issue, and the page number.*

Effect of Transition Density on Performance of a DTTL

One can estimate the minimum transition density needed to limit the symbol-error rate.

NASA's Jet Propulsion Laboratory, Pasadena, California

Theoretical calculations and the accompanying computer simulations provide the numerical basis for specification of the minimum data-transition density needed for adequate performance of a radio receiver that processes a noisy signal that contains a non-return-to-zero (NRZ) stream of data symbols (bits). By use of a digital-data-transition-tracking loop (DTTL), the receiver strives to synchronize its operation with the data symbols. The performance of the receiver in terms of its ability to keep the symbol-error rate (SER) in the output of the receiver below a specified level depends on the symbol signal-to-noise ratio (SSNR) of the incoming signal and on the degree of synchronization.

The ability of the DTTL to maintain synchronization depends partly on the SSNR and partly on the data-transition density. (The data-transition density is a statistical property of the data stream; it is the number of data transitions observed divided by the number of symbol periods of continuous observation time or, equivalently, the probability of a data transition during one symbol period. The maximum possible value of this probability is .5 if one assumes that the noise spectrum at the output of the loop phase detectors is independent of the transition density.) The degradation of performance of a first-order DTTL can be expressed by

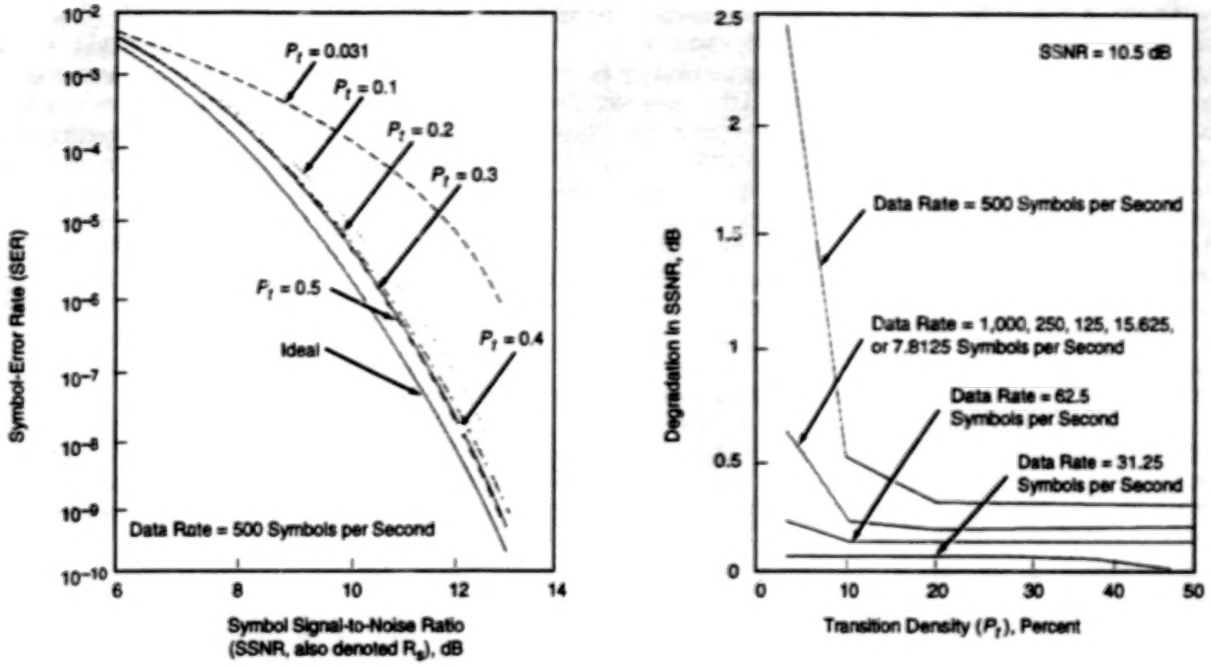
$$\frac{\sigma_e^2}{T^2} = \frac{\xi T B_L}{8 m P_t^2 R_s \mathrm{erf}^2 \sqrt{R_s}}$$

where σ_e is the root-mean-square timing error (symbol-synchronization jitter), T is the duration of the symbol period, ξ is the width of the window, B_L is the one-sided loop noise bandwidth, P_t is the data-transition density, m is the number of timing-error samples accumulated prior to correction of timing, R_s is the SSNR, and "erf" denotes the error function.

Of course, the performance of the receiver is degraded by timing error as well as by noise. The overall degradation of performance can be expressed as

$$PE(\lambda) = \frac{1}{2} P_t \mathrm{erfc}\left[\sqrt{R_s}(1 - 2|\lambda|)\right] + \frac{1}{2}(1 - P_t)\mathrm{erfc}\left(\sqrt{R_s}\right)$$

where PE is the probability of error (or, equivalently, the SER) and λ is the timing error in units of T. The timing error computed by the first equation can be inserted in this second equation, and the resulting equation can be integrated



The Degradation of Performance in terms of SER and degradation of SSNR was computed for various data rates, a window width of 1, and various values of P_t. The plot on the right can be used to select the minimum P_t needed to obtain an acceptably low degradation of SSNR at a given data rate.

numerically to obtain values for the degradation of performance in terms of SER for a given P_t and R_s. Alternatively, the contribution of the timing error to the degradation of performance can be expressed in terms of that decrease in SSNR that would produce the same SER in a perfectly synchronized receiver. The figure presents examples of results of such computations.

This work was done by Tien M. Nguyen and Sami M. Hinedi of Caltech for **NASA's Jet Propulsion Laboratory.** *Further information is contained in a TSP [see page 1].*

NPO-18999

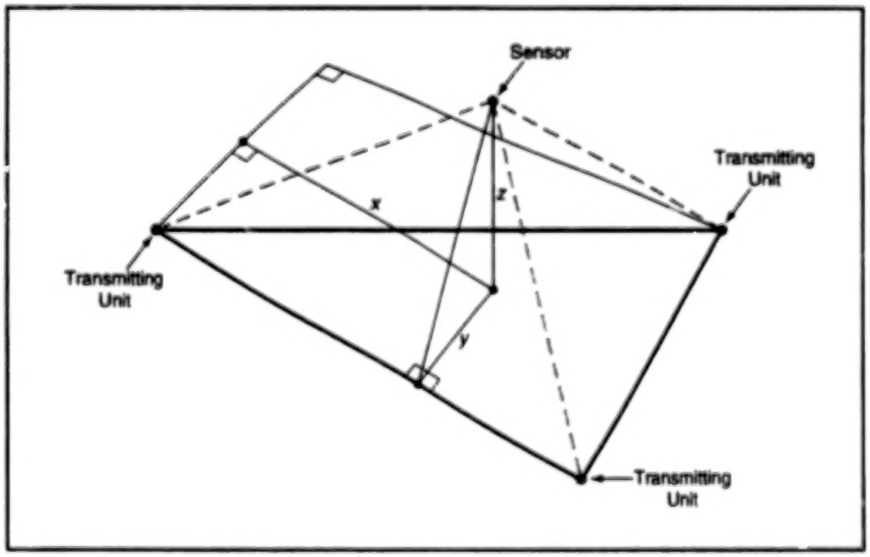
Infrared/Ultrasonic Position-Measuring System

Position coordinates are calculated from three distance measurements.

Marshall Space Flight Center, Alabama

A system for measuring the positions of sensors at designated points on a body suit is being developed. The measuring system, body suit, and sensors are to be incorporated into an interactive virtual-reality system, wherein they would provide feedback data on the positions and orientations of various parts of the wearer's body. The system is based on the straightforward concept of computing the three-dimensional coordinates of a sensor from simultaneous measurements of the distances of the sensor from three locations, the coordinates of which are known (see figure).

The principle of measurement is essentially the same as that of a popular technique that has been used for many years to estimate the distance of a lightning stroke; namely, by watching the flash and counting the time until one



Position Coordinates (x,y,z) of a sensor can be calculated, once the distances (indicated by dashed lines) to the sensor from three transmitting units at known locations have been measured.

hears the thunder. For this purpose, the system includes a transmitting unit at each of the three known locations. Each transmitting unit emits an infrared pulse (analogous to the visible flash) and an ultrasonic chirp (analogous to thunder) simultaneously.

An infrared sensor at each body location detects the infrared pulse (which travels at the speed of light) and the output of the sensor triggers a crystal-controlled timer. A short time later, an ultrasonic sensor at the same location receives the corresponding chirp (which travels at the speed of sound); the output of this sensor causes the timer to stop. Because the time of travel of the infrared pulse is negligibly small in comparison with the time of travel of the ultrasonic pulse, the interval of time thus measured is a close approximation of the distance between the transmitter and the sensor, divided by the speed of sound. Thus, multiplication of the time interval by the speed of sound gives the distance.

When pulses from the other two transmitting units have been similarly received by the sensor, the distances from the body location to the other two transmitting units can also be established. The three-dimensional coordinates of the sensor are then computed by inserting the three distances into the algebraic solution of the simultaneous equations for the spherical surfaces defined by the three distances.

In the fully developed system, all sensor pairs would watch and listen simultaneously for signals from the transmitting units. Thus, a single set of infrared pulses and chirps from each of the three transmitting units would provide sufficient data to calculate the positions of all the sensors. The timers used in a prototype of the system can be turned on and off within two microseconds of receipt of signals from the infrared and ultrasonic sensors. Inasmuch as sound travels less than one millimeter in two microseconds, the calculated position coordinates are expected to be accurate to within about a millimeter. The system operates at up to 30 samples per second and measures distances up to 12 feet (≈3.7 m).

This work was performed by Ricky J. Roberson of Tommorowtools for **Marshall Space Flight Center**. *Further information is contained in a TSP [see page 1].*

Inquiries concerning rights for the commercial use of this invention should be addressed to the Patent Counsel, Marshall Space Flight Center [see page 1]. Refer to MFS-26275.

Books and Reports

Evaluation of Vibration-Monitoring Gear-Diagnostic System

The system was found to be fairly effective in detecting surface fatigue pits.

A report describes an experimental evaluation of a commercial electronic system designed to monitor the vibration signal from an accelerometer on a gearbox to detect vibrations indicative of damage to gears. The system includes a signal-conditioning subsystem and a personal computer in which an analog-to-digital converter has been installed. The computer runs software that analyzes the digitized signals; it performs gear-rotation-synchronous averaging of the vibration signal to produce a vibration image of each tooth on any gear in the gearbox under test, generates indications of the status of the gears, and issues alarms when vibration-signal parameters characteristic of damage exceed normal limits. In the experimental evaluation, the system was used to analyze vibration signals to detect surface fatigue pits on spur gears in a spur-gear fatigue test rig. Several vibration-signal parameters were analyzed, including gear-pair stress-wave amplitudes, and raw baseband vibration amplitudes, kurtosis, peak ratios, and others. The results of the experiment showed that the system is fairly effective in detecting surface fatigue pits on spur-gear teeth.

This work was done by Dennis P. Townsend and James J. Zakrajsek of **Lewis Research Center**. *To obtain a copy of the report, "Evaluation of a Vibration Diagnostic System for the Detection of Spur Gear Pitting Failures," see TSP's [page 1].*

Inquiries concerning rights for the commercial use of this invention should be addressed to the Patent Counsel, Lewis Research Center [see page 1]. Refer to LEW-16091.

Comparison of Full-Spectrum and Complex-Symbol Combining

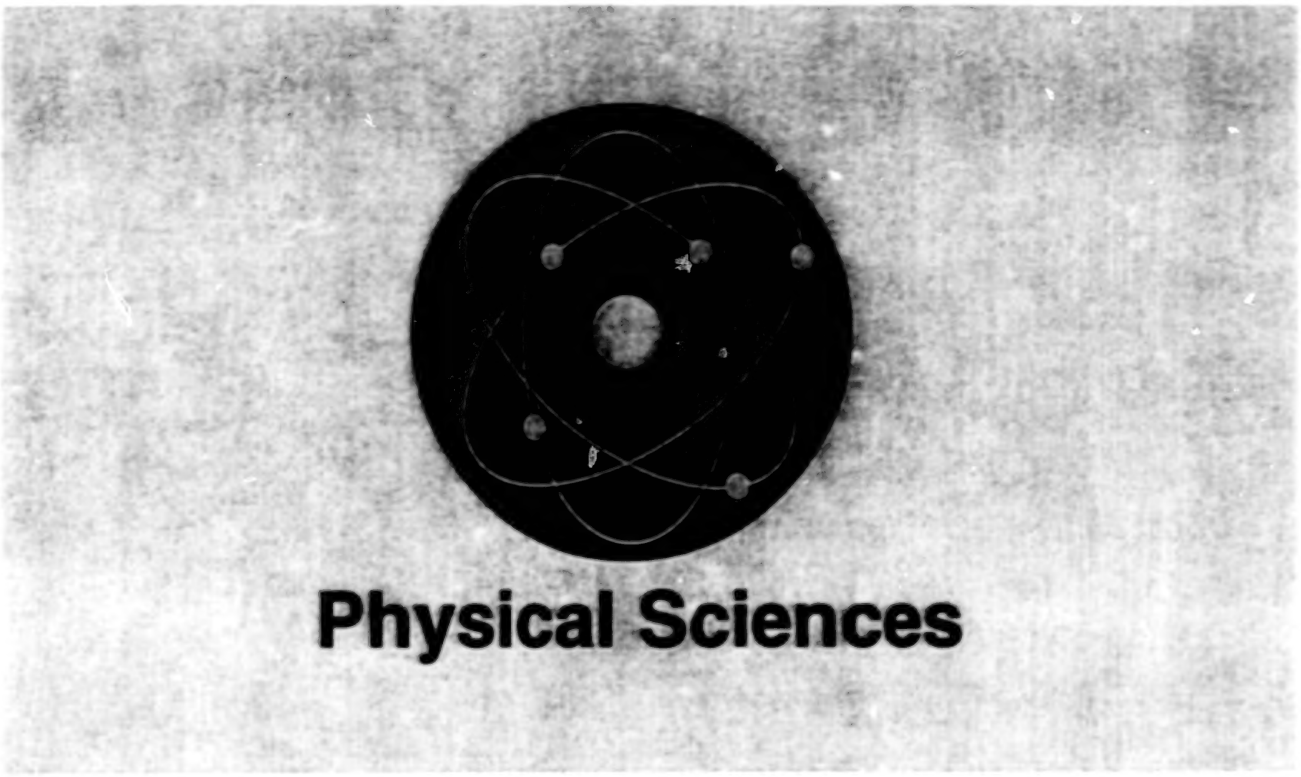
Performances of two antenna-arraying methods are compared for various combinations of antennas.

A report presents a theoretical study of the anticipated performances of two methods of combining S-band signals from the Galileo spacecraft received in multiple antennas of NASA's Deep Space Network (DSN). The signal transmitted by the spacecraft consists of a binary data signal phase-modulated onto a square-wave subcarrier that is, in turn, amplitude-modulated onto an S-band carrier. One of the methods, called "full-spectrum combining" (FSC), involves combining signals from multiple antennas at an intermediate frequency (IF), then demodulating the combined signal by use of a single receiver chain that comprises one carrier-phase-tracking loop, one subcarrier-phase-tracking loop, one data-symbol-synchronization loop, and one matched filter. The other method, called "complex-symbol combining" (CSC), has been made possible, in principle, by the advent of all-digital receivers in the DSN. In CSC, the received signal would be open-loop down-converted to IF, then open-loop down-converted to near baseband by use of the predicted carrier frequency. The baseband signal would then be used for subcarrier tracking, symbol synchronization, and matched filtering. The matched-filter output from multiple antennas would then be aligned and combined at baseband and demodulated by use of a baseband carrier loop. The key difference between FSC and CSC is that in FSC, carrier-phase alignment precedes subcarrier demodulation, symbol synchronization, and matched filtering, whereas in CSC, it would follow. In the study, the performances of FSC and CSC were analyzed for various combinations of antennas and characterized in terms of two measures. One measure was the symbol signal-to-noise-ratio degradation, D [defined as the decibel measure of the ratio between (1) the unconditional signal-to-noise ratio (SNR) at the output of the matched filter in the presence of imperfect synchronization

and (2) the SNR at the output of an ideal matched filter]. The other measure was the symbol SNR loss, *L* [defined as the decibel measure of the additional symbol SNR needed to achieve the same symbol-error as in the case of perfect synchronization]. *D* and *L* were found to be approximately equal at low values of symbol SNR but to diverge at high SNR values.

This work was done by Samson Million, Biren Shah, and Sami Hinedi of Caltech for **NASA's Jet Propulsion Laboratory**. *To obtain a copy of the report, "A Comparison of Full-Spectrum and Complex-Symbol Combining Techniques for the Galileo S-Band Mission," see TSP's [page 1].*
NPO-19392

BLANK PAGE



Physical Sciences

Hardware, Techniques, and Processes

23 Flight-Test Fixture for Aerodynamic Research
23 Dynamic Light Scattering With Improved Fiber-Optic Probes
24 Fiber-Optic/Photoelastic Flow Sensors
25 Measuring Fluxes of Heat to a Plasma-Arc Anode
26 Optical-Fiber Fluorosensors With Polarized Light Sources
27 Measuring Thicknesses With In Situ Ultrasonic Transducers

Books and Reports

27 Thermodynamic Data for 50 Chemical Elements

BLANK PAGE

Flight-Test Fixture for Aerodynamic Research

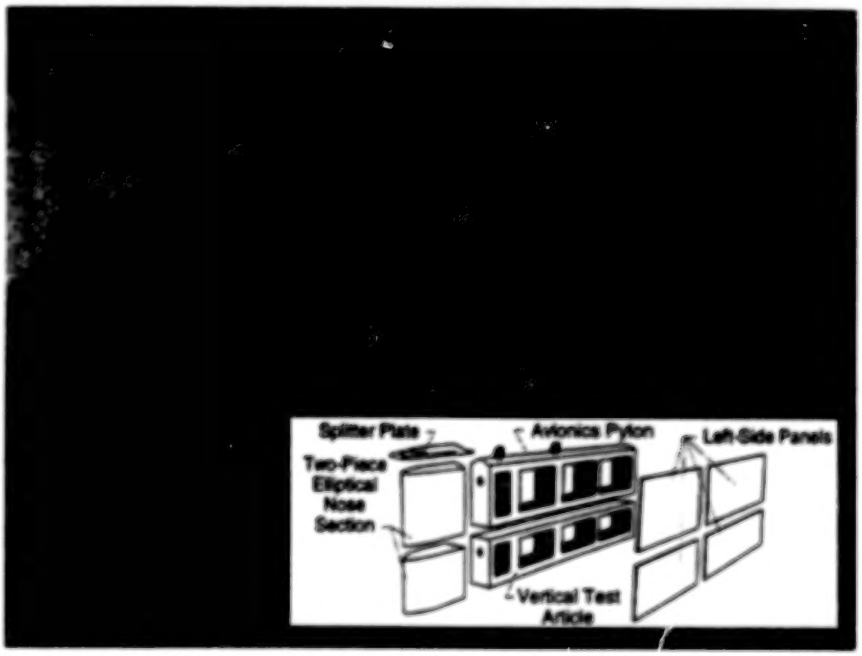
This fixture has been used at airspeeds up to mach 2.0.

Dryden Flight Research Center, Edwards, California

Engineers at the NASA Dryden Flight Research Center have developed a second-generation flight-test fixture (FTF-II) to be used as a generic test bed for research in aerodynamics and fluid mechanics. The FTF-II (see figure) is a low-aspect-ratio, finlike structure mounted on the centerline of the lower fuselage surface of an F-15B airplane. The fixture is 107 in. (272 cm) long, 32 in. (81 cm) high, and 8 in. (20 cm) wide with a 12° elliptical nose section and a blunt trailing edge. Built primarily of carbon/epoxy materials, the fixture consists of a pylon with replaceable side panels, nose section, and a vertical test article.

A modular configuration makes it possible to modify the FTF-II to satisfy a variety of flight-test requirements. The upper 19 in. (48 cm) of the FTF-II is occupied by the avionics pylon, which is a permanent structure that houses avionics, permanent research instrumentation systems, and other support equipment common to most flight experiments. The lower 13 in. (33 cm) of the FTF-II is the vertical test article, which, in the current configuration, matches the contour of the avionics pylon. The vertical test article is removable and can be replaced by vertical test articles of other aerodynamic shapes. Normally, only instrumentation specific to individual research experiments is installed in the vertical test article.

Flush external fasteners provide for quick removal of four left-side panels for access to interior compartments. Two right-side panels extend the length of the fixture and are attached by internal fasteners, which minimize discontinuities for aerodynamic experiments such as surface-flow-visualization studies. The 12° elliptical nose section is located in the forward 18.8 in. (48 cm) and comprises two pieces — one for the avionics pylon and one for the vertical test article. Each piece of the elliptical nose section can be installed or removed independently of the other. To improve the quality of the airflow around the FTF-II, a removable pylon fairing and a splitter plate were installed on the upper portion of the fixture. When needed, a removable air-data probe can be installed near the bottom of the piece of the nose section on the vertical test article.



The FTF-II is a highly instrumented finlike structure mounted on the lower fuselage surface of the F-15B airplane.

Because the FTF-II has self-contained research capabilities, the only additional external support essential for operation is electric power from the airplane. The FTF-II uses a 12-bit pulse-code-modulation system capable of multiplexing data at frequencies as high as 200 Hz, depending on the number of data channels. Flight data are transmitted to the ground for storage and postprocessing. A tape recorder in the F-15B airplane is used for backup or to record high-frequency data for a specific flight experiment. Standard FTF-II instrumentation includes a removable air-data probe, load cells to monitor in-flight side loads, flush static-pressure orifices, internal accelerometers (4), and temperature sensors.

The FTF-II has already been used in several flight-research experiments and is now operational and available for potential use by industry and universities. The FTF-II and the F-15B airplane on which it was mounted performed successfully in recent flight tests in which the maximum airspeed was increased to mach 2.0. The results of handling-quality tests of this F-15B/FTF-II combination were similar to those of an F-15 airplane configured with a centerline tank, and included sufficient aircraft directional stability. Flow-pressure surveys and flow-visualization studies revealed flows of good quality throughout the range of speeds and other flight conditions.

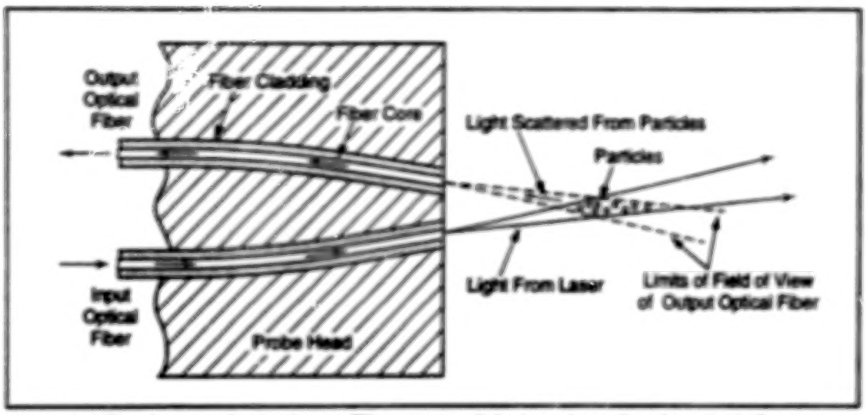
This work was done by David M. Richwine of PRC Inc. and John H. Del Frate of **Dryden Flight Research Center**. *Further information is contained in a TSP [see page 1].*
DRC-95-27

Dynamic Light Scattering With Improved Fiber-Optic Probes

Rugged probes can be used in concentrated suspensions to measure particle-size distributions.

Lewis Research Center, Cleveland, Ohio

Improved fiber-optic probes have been developed for use in dynamic light-scattering measurements. More particularly, the probes are intended for measuring dynamic backscattering of laser light from concentrated suspensions of particles in liquids, for the purpose of determining statistical distributions of sizes of the particles. Such determinations are



Particles Illuminated via the Input Fiber scatter light in various directions, including toward the output fiber. Particle-size distributions can be determined from dynamic light-scattering measurements.

important for monitoring and controlling many industrial processes.

Conventional light-scattering apparatuses are too bulky and delicate for routine use in hostile environments like those of industrial processes. Furthermore, conventional systems yield useful data on dilute suspensions only; the large amount of multiple scattering of light in concentrated suspensions complicates the light-scattering physics to such a degree that there is no practical way to interpret the light-scattering data correctly.

Fiber-optic probes offer the obvious advantages of compactness and ruggedness, and are thus more suitable for industrial environments. Fiber-optic probes can even be immersed in the suspensions to be characterized. The associated lasers, photodetectors, and signal-processing circuits can be located remotely in safer environments, coupled to the probes via optical fibers.

With improved fiber-optic probes, the backscattering regime of operation was chosen because the receiving and detection paths traveled by the photons are so short that the amount of multiple scattering is negligible in the back-scattering direction. A fiber-optic probe of older design contains a single optical fiber that both carries the laser light into the scattering medium and carries the scattered light back to the photodetectors. Many problems are associated with this design and they include mechanical complexity and fragility.

In a fiber-optic probe of the improved type, there are two monomode optical fibers: one fiber carries the laser light into the scattering medium, while the other carries the scattered laser light to a photomultiplier. A digital correlator computes the temporal correlation of intensities as represented by the photon-pulse-train output of the photomultiplier. Inversion of the autocorrelation data leads to the particle-size distribution.

The use of two fibers makes it possible to measure backscattering at an angle that differs enough from 180° to eliminate the scattered-light/laser-light ambiguity, yet is close enough to 180° to suppress multiple scattering. Also, by choice of both the angle and the distance between fibers, one can select not only the scattering angle but also the location of the center of the scattering region at the intersection of the optical axes of the two fibers.

This work was done by Harbans Singh Dhadwal of the State University of New York, Rafat R. Ansari of Case Western Reserve University, and William V. Meyer of the Ohio Aerospace Institute for **Lewis Research Center**. *Further information is contained in a TSP [see page 1].*
LEW-15461

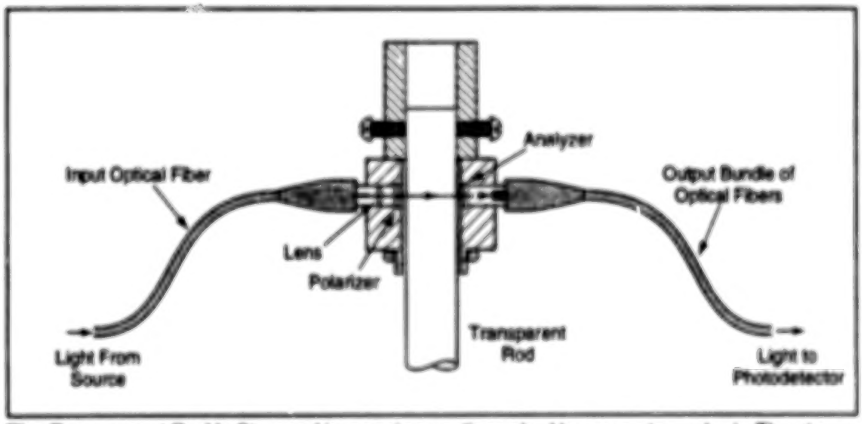
Fiber-Optic/Photoelastic Flow Sensors

Simple, rugged, lightweight transducers detect periodic vortices.

Lewis Research Center, Cleveland, Ohio

Fiber-optic-coupled transducers are being developed to measure flows over wide dynamic ranges and over wide temperature ranges in severe environments. They could be used, for example, to measure flows of fuel in advanced aircraft engines. The feasibility of these sensors has been demonstrated in tests of a prototype sensor in water flowing at various temperatures and speeds. Fiber-optic-coupled flow transducers are particularly attractive for aircraft applications because optical fibers are compact, are lightweight, and make possible the transmission of sensor signals at high rates with immunity from electromagnetic interference at suboptical frequencies.

The developmental flow sensors can be designed to exploit fully the ruggedness of fiber optics: unlike in some other sensor systems with fiber-optic coupling, there are no delicate electronic components at the transducer locations because the principle of operation of these flow sensors does not involve optical-to-electronic or electronic-to-optical conversions within the flow transducers. Instead, these sensors utilize optical-to-optical conversion via the photoelastic effect.



The Transparent Rod Is Stressed by passing vortices shed by an upstream body. The stress in the rod is measured via the photoelastic effect. The frequency of fluctuation light traveling to the photodetector is proportional to the vortex-passage frequency.

The developmental sensors are based partly on the established concept of the vortex-shedding flow sensor: A bluff body — typically a rod — is placed in the stream to be measured, oriented trans-

versely to the direction of flow. Vortices form on the downstream side of the body. At any speed within a wide range of speeds, the vortices detach alternately from opposite downstream edges or corners of the body in a regular series and travel downstream in what is called a "Karman vortex street." The vortices can be sensed at a location close to and downstream of the bluff body by use of a rod equipped with a strain sensor to measure the periodic load applied to the rod by the passing vortices. The frequency of passage of the vortices is directly proportional to the speed of flow, the factor of proportionality being a function of the density and viscosity of the fluid and thus a function of temperature.

In a transducer of the present type the downstream sensing rod (see figure) is made of a transparent material. Light from a light-emitting diode or other source is brought in by an input optical fiber, is focused by a lens, and passes through a polarizer. The linearly polarized light that emerges from the polarizer passes through the rod at a location near its clamped end, where the bending stress induced by the passing vortices is greatest. After emerging from the rod, the light impinges on a second polarizer (analyzer) with polarization perpendicular to that of the first polarizer. The portion of light that survives passage through the analyzer enters an output bundle of optical fibers, which transmits the light to a photodetector.

In the absence of stress in the rod, the polarization of light is not changed by passage through the rod; the light incident on the analyzer remains polarized perpendicularly to the polarization axis of the analyzer and consequently little or no light passes through the analyzer. When the rod is stressed, the photoelastic effect in the rod material causes a change in the polarization of the light passing through, so that some of the light becomes polarized along the polarization axis of the analyzer, giving rise to an increase in light transmitted to the photodetector. The optical power that passes through to the photodetector is proportional to $[\sin(k\sigma)]^2$, where σ is the stress in the rod and k is a constant of proportionality that depends on the rod material.

The fundamental frequency of fluctuation of the photodetector output is thus proportional to the rate of flow. Signal-processing circuitry connected to the photodetector measures this frequency. The frequency reading can be digitized and processed, along with an ancillary temperature reading, by an algorithm that corrects for the effect of temperature on the factor of proportionality between the vortex-passage frequency and the rate of flow.

This work was done by Laurence N. Wesson, and Nelle L. Cabato of Aurora Optics, Inc., and Edward F. Brooks, private consultant, for **Lewis Research Center**. *Further information is contained in a TSP [see page 1].*
LEW-15536

Measuring Fluxes of Heat to a Plasma-Arc Anode

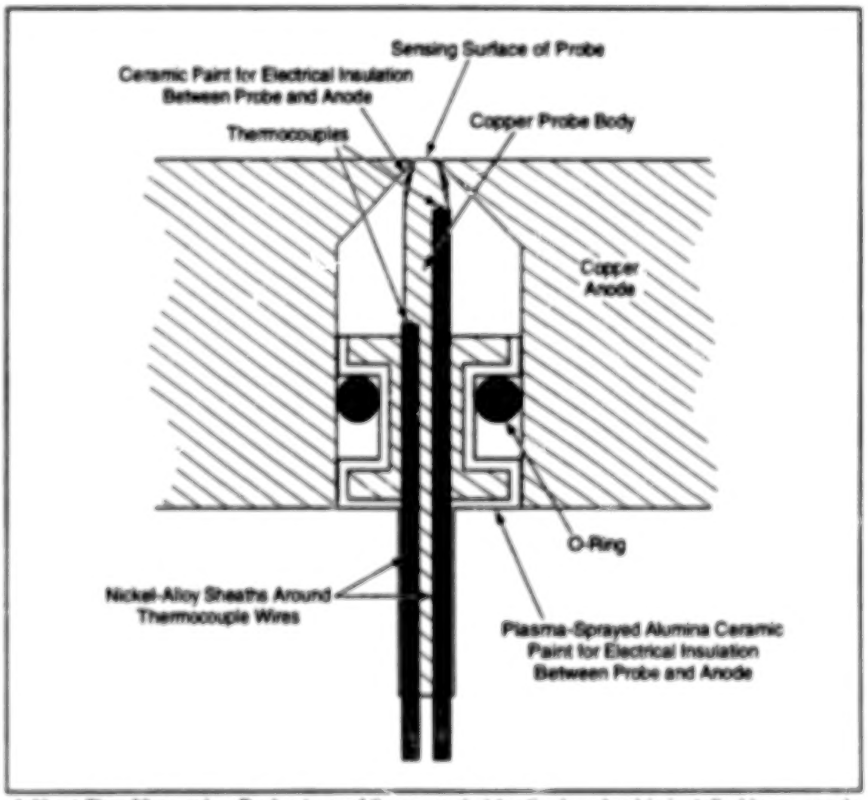
Three probes yield data on conduction, convection, and radiation of heat to the anode.

Lewis Research Center, Cleveland, Ohio

Three probes have been constructed to provide measurements indicative of the conductive, convective, and radiative transfer of heat from a free-burning plasma arc to a water-cooled copper anode used in generating the arc. During a plasma experiment, one of these probes is installed in a cavity in the anode, with the sensing surface of the probe flush with that surface of the anode that faces the plasma (see figure). The probe is electrically insulated from the anode; the potential of the probe is allowed to float at the potential of the plasma so that there is no spurious heating of the probe by impact of electrons.

Each probe consists mainly of a copper body with two thermocouples embedded at locations 4 mm apart along its length. The thermocouples provide a measure of the rate of conduction of heat along the probe and thus the transfer of heat from the plasma to the sensing surface at the tip of the probe. The three probes are identical except that the sensing surface of one is uncoated and the sensing surfaces of two of them are coated with different materials to make them sensitive to different components (conductive, convective, and radiative) of the overall flux of heat.

The probe with the uncoated (copper) tip is designed to absorb the same conductive, convective, and radiative fluxes of heat as does the surrounding area of the anode. The tip of one probe is coated with platinum to make it sensitive primarily to the conductive and convective fluxes. The tip of the third probe is coated



A Heat-Flux-Measuring Probe (one of three nearly identical probes) is installed in an anode to measure some of the components of the flux of heat from a plasma to the anode.

with carbon black to make it absorb nearly all of the incident radiant flux plus the same conductive and convective flux as that into the platinum-coated probe. The conductive, convective, and radiative fluxes of heat to the anode can be computed by computing differences among the heat-flux readings of the three probes.

This work was done by John M. Sankovic of **Lewis Research Center** *and James A. Menart, Emil Pfender, and Joachim Heberlein of the University of Minnesota. Further information is contained in a TSP [see page 1].*
LEW-16076

Optical-Fiber Fluorosensors With Polarized Light Sources

Transverse polarization would increase sensitivity.

Langley Research Center, Hampton, Virginia

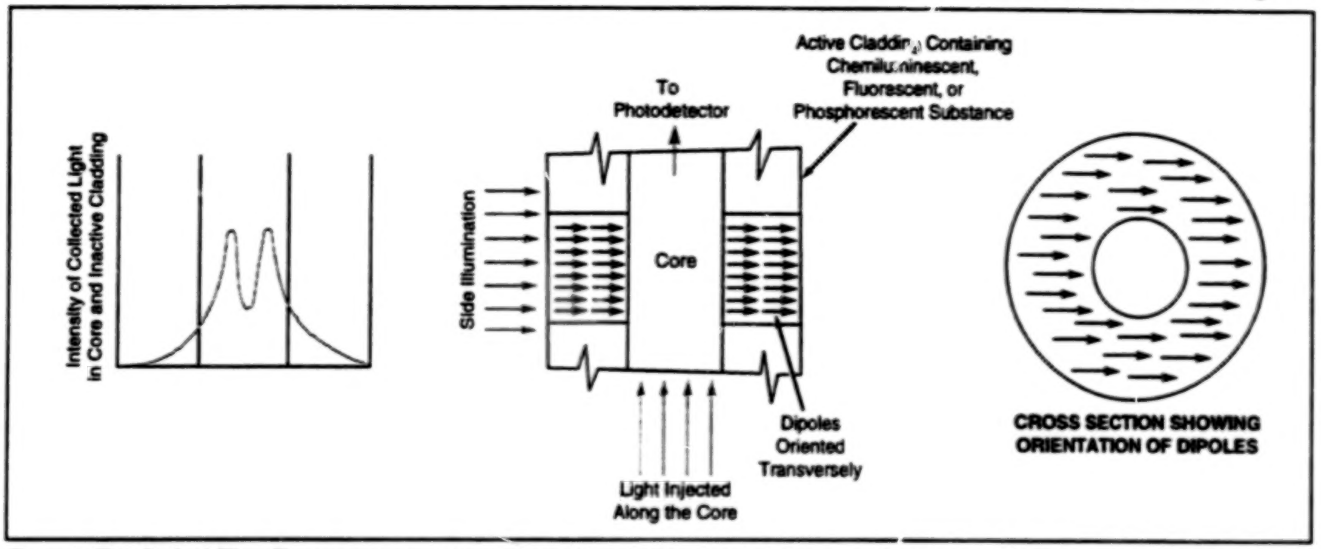


Figure 1. This Optical-Fiber Fluorosensor would contain radiating dipoles oriented along an axis perpendicular to the cylindrical axis. In other respects, it would be similar to prior optical-fiber fluorosensors in which the dipoles are oriented randomly.

The chemiluminescent and/or fluorescent molecules in optical-fiber fluorosensors would preferably be oriented with their light-emitting dipoles along the transverse axis, according to a proposal. In comparison with an otherwise identical optical-fiber fluorosensor in which the same number of dipoles were oriented randomly, a sensor of the proposed type would capture a greater fraction of the chemiluminescence or fluorescence and transmit it to a photodetector; that is, it would be more sensitive.

The basic principles of optical-fiber fluorosensors were described in "Making Optical-Fiber Chemical Sensors More Sensitive" (LAR-14525), *NASA Tech Briefs*, Vol. 17, No. 3 (March 1993), page 77; "Improved Optical-Fiber Chemical Sensors" (LAR-14607), *Laser Tech Briefs*, Vol. 2, No. 2 (Spring 1994), page 61; and "Improved Optical-Fiber Temperature Sensors" (LAR-14647), *Laser Tech Briefs*, Vol. 1, No. 1 (September 1993), page 54. As explained in more detail in those articles, a typical optical-fiber fluorosensor would include a sensing length in which the cladding or the core of the fiber would contain molecules that fluoresce or chemiluminesce in the presence of a substance to be detected or would contain molecules that change their fluorescence with different temperatures. For cladding

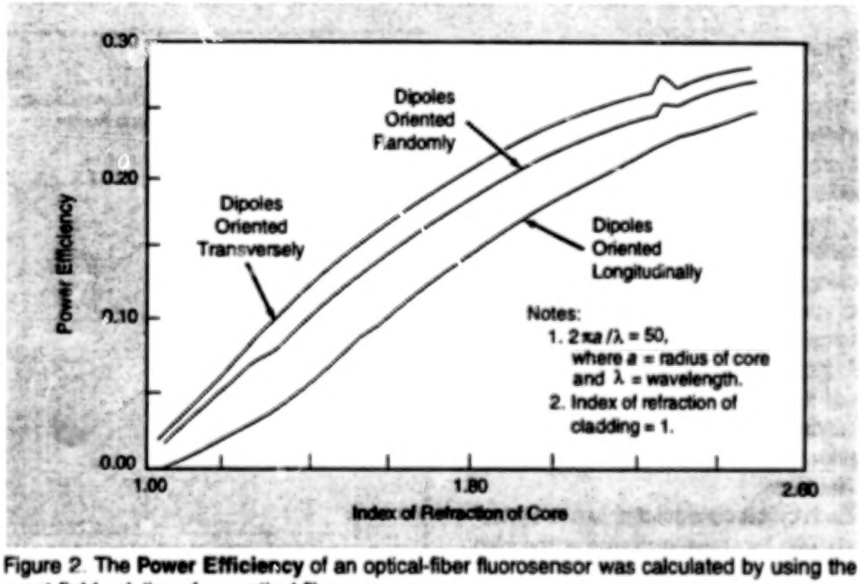


Figure 2. The Power Efficiency of an optical-fiber fluorosensor was calculated by using the exact field solution of an optical fiber.

sources, part of the fluorescence, chemiluminescence, or phosphorescence would be coupled, via the evanescent-wave interaction, into the core and transmitted along the core to a photodetector.

Figure 1 shows the proposed optical-fiber fluorosensor with transversely oriented dipoles. As in the case of randomly oriented dipoles, illumination to excite fluorescence could be supplied from the side or by injection along the core with evanescent-wave absorption by the cladding.

For the purpose of comparison among different designs, a principal figure of merit is the power efficiency, which is the ratio between the power of the light captured by the core toward the photodetector and the total power of light emitted by the dipoles (which is the sum of the power radiated away by the fiber and the power captured by the core in both directions). The power efficiency can be calculated by using the exact field solution of an optical fiber and

solved for given distribution of radiating dipoles. As shown in the example of Figure 2, the calculated power efficiency is greater when the dipoles are oriented transversely.

This work was done by Claudio O. Egalon of Analytical Services and Materials, Inc., and Robert S. Rogowski of **Langley Research Center.** *Further information is contained in a TSP [see page 1].*

Inquiries concerning rights for the commercial use of this invention should be addressed to the Patent Counsel, Langley Research Center [see page 1]. Refer to LAR-14652.

Measuring Thicknesses With In Situ Ultrasonic Transducers

Ultrasonic transducers would be semipermanently attached to a workpiece.

Marshall Space Flight Center, Alabama

Several pulsed ultrasonic transducers would be attached to a workpiece for measurement of changes in the thicknesses of the workpiece at the transducer locations during grinding and polishing, according to a proposal. Once attached, each transducer would remain attached at its original position until all grinding and polishing operations were complete.

In a typical application, the workpiece would be a glass or ceramic blank destined to become a component of an optical system. Heretofore, it has been common practice to measure thicknesses of such a workpiece at different positions by use of a single ultrasonic transducer, which is placed on the workpiece at each measurement location in sequence. The nonrepeatability of placement inherent in this practice has been a source of large errors in thickness measurements. By using several transducers and cementing them at the measurement positions (see Figure 1), one would eliminate placement errors.

Figure 2 illustrates a computer-controlled ultrasonic measurement system that would implement this concept. The ultrasonic transducers would be connected via a multiplexer to a commercial ultrasonic-testing circuit. Under computer control, the multiplexer would connect the transducers to the instrument in sequence. The ultrasonic-testing circuit would thus produce thickness readings for the various transducer locations in sequence, and these readings would be sent to the computer.

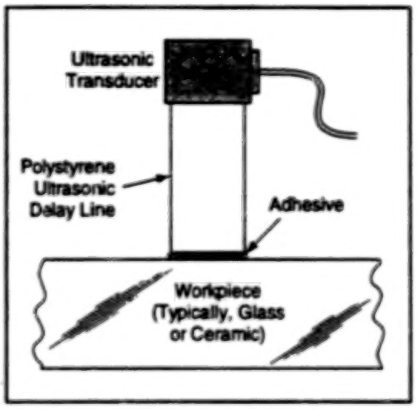


Figure 1. Each Ultrasonic Transducer would be attached mechanically to a commercial polystyrene delay line, which would be cemented to the workpiece with a thin film of acoustically conductive adhesive.

Such a system was implemented for the grinding and polishing of the AXAF mirror elements. Eight sites per optic were multiplexed. The average rms repeatability was 0.19 μm, about 10 parts per million for the thicknesses measured.

This work was done by Daniel E. Dunn and Joseph R. Cerino of Hughes Danbury Optical Systems, Inc., for **Marshall Space Flight Center.** *Further information is contained in a TSP [see page 1].*
MFS-28892

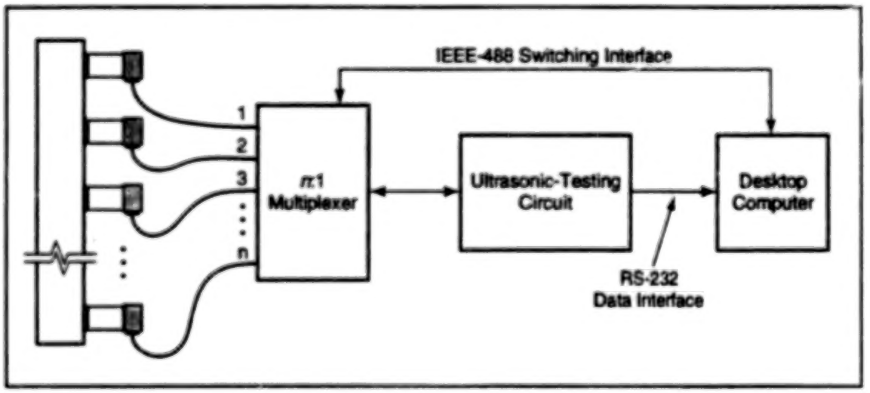


Figure 2. The Computer-Controlled Ultrasonic Testing System would take readings via the semipermanently bonded ultrasonic transducers and map out changes in the thickness of the workpiece.

Books and Reports

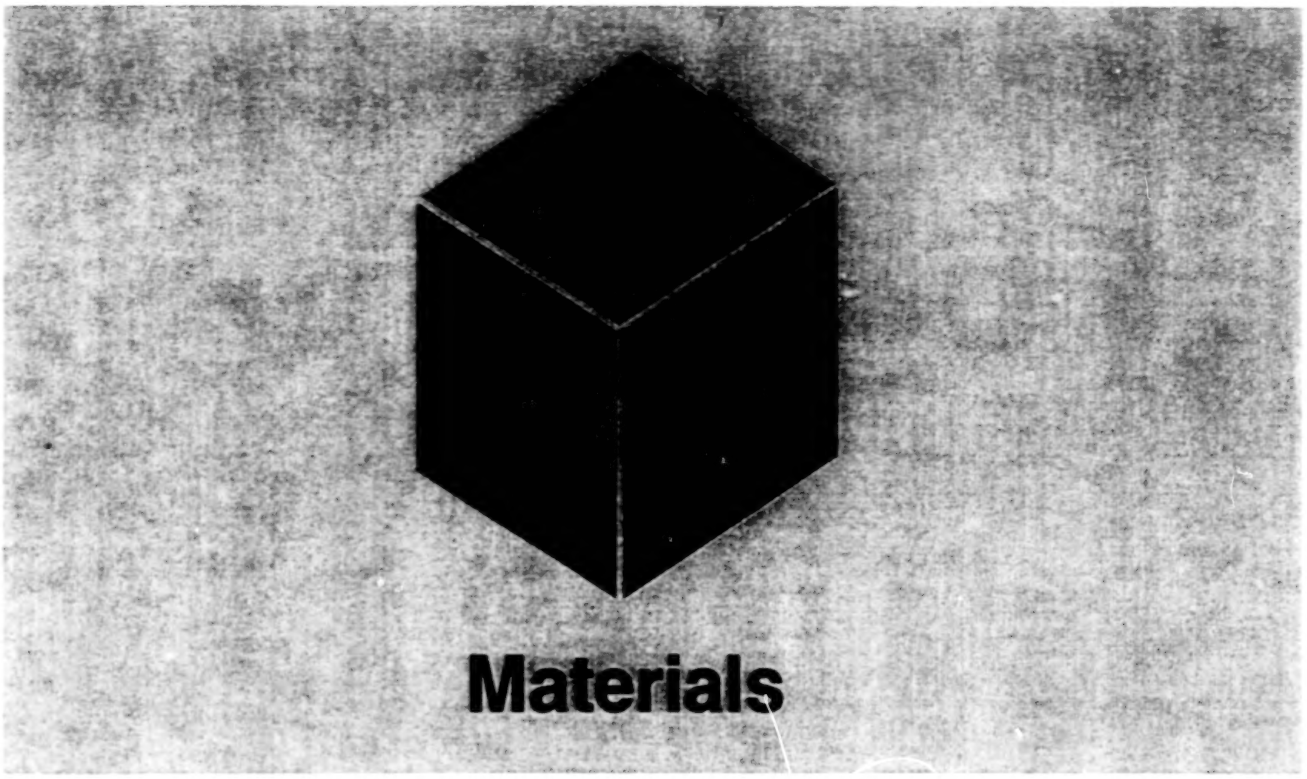
Thermodynamic Data for 50 Chemical Elements

Data are given in tabular and functional form.

A report presents data on the thermodynamic properties of 50 chemical elements, an isotope (deuterium) of one of the elements, and electron gas, all in standard reference states. The data are tabulated as functions of temperature; they are also given in the form of least-squares-fit coefficients of two functional forms for heat capacities (specific heats) at constant pressure (C_p^o) in standard states, with constants of integration for enthalpy and entropy. One functional form for C_p^o is a fourth-order polynomial in absolute temperature (T). The other functional form includes two additional terms; one with T^{-1}, the other with T^{-2}. The properties of the gases Ar, D_2, e^-, H_2, He, Kr, N_2, Ne, O_2, and Xe are tabulated for temperatures from 100 to 20,000 K. The properties of the remaining gases Cl_2 and F_2 are tabulated for temperatures from 100 to 6,000 K. The polynomial functional form for C_p^o for all these gases is split into the two temperature intervals of 200 to 1,000 K and 1,000 to 6,000 K. For those gases, the properties of which are tabulated for temperatures up to 20,000 K, the second functional form of C_p^o is specified in an additional temperature interval of 6,000 to 20,000 K. The least-squares fits are constrained so that the properties calculated by the functional forms match at the common tempera-

ture end points. The temperature ranges for the condensed species vary with ranges of the data, phase changes, and shapes of the C_p^0 curves.

This work was done by Bonnie J. McBride of **Lewis Research Center**, *Sanford Gordon of Sanford Gordon and Associates, and Martin A. Reno of Heidelberg College. To obtain a copy of the report, "Thermodynamic Data for Fifty Reference Elements," see TSP's [page 1].*
LEW-15978



Materials

Hardware, Techniques, and Processes

31 Improved Preparation of Solid-Electrolyte Films
31 Mathematical Model of Curing Behavior of a Polymer
32 Hydrophobic Catalysts for Removal of NO_x From Flue Gases
33 Wire-Arc-Sprayed Aluminum Protects Steel Against Corrosion
34 Eutectic-Free Superalloy Made by Directional Solidification
34 Polyimides Made From PDMDA

Books and Reports

36 Stress in a Fiber During Curing of Surrounding Matrix Resin
37 Performance of Perfluoropolyalkylether Lubricant System

BLANK PAGE

Improved Preparation of Solid-Electrolyte Films

A modified process ensures compatibility among components.

NASA's Jet Propulsion Laboratory, Pasadena, California

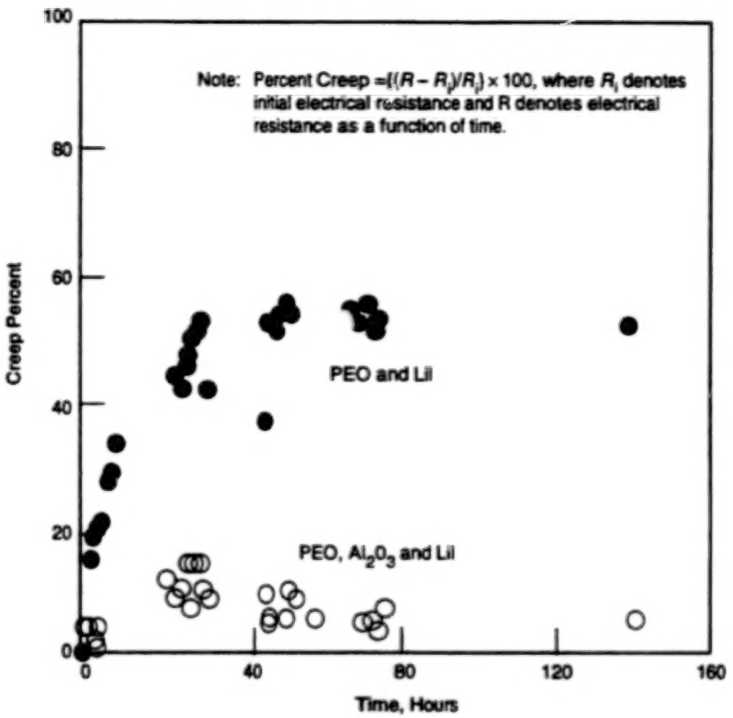
An improved chemical-blending procedure produces a composite material for thin, large-area solid-electrolyte films for lithium batteries. The films have uniform compositions and are dimensionally stable. The transport number of their lithium cations is high, close to unity. Batteries made with these films are expected to have energy and power densities up to about 100 W•h/kg and 100 W/kg, respectively.

A previous version of the composite material was described in "Composite Solid Electrolyte for Lithium Cells" (NPO-18694), *NASA Tech Briefs*, Vol. 18, No. 7 (July 1994), page 49. The composite material is a combination of polyethylene oxide, alumina, and lithium iodide ($PEO/Al_2O_3/LiI$). Previous attempts to make the composite by dissolving constituents one at a time in an acetonitrile solution were only partially successful in that as soon as PEO was added to the mixture containing the other ingredients, the alumina particles became agglomerated into balls covered with PEO. Therefore, the films made with the composite material did not have a uniform composition.

An experiment showed that agglomeration could be prevented by adding isopropyl alcohol to the mixture before adding PEO. The alcohol apparently inhibits the scavenging action of PEO.

The experiment involved the following steps:

- Appropriate amounts of LiI, Al_2O_3, and PEO were weighed out separately.
- The LiI was dissolved in 50 mL of acetonitrile.
- The alumina was added to the LiI/acetonitrile solution and stirred for 5 min.



Composite of Polyethylene Oxide, Alumina, and Lithium Iodide exhibited much less creep than did a composite that did not include alumina.

- 80 mL of isopropyl alcohol were added to the solution and stirred well. Another 120 mL of acetonitrile were stirred in, followed by 80 mL more of the alcohol.
- While the solution was stirred vigorously, the PEO was added. Stirring was continued overnight to dissolve the PEO.

The particles of alumina in the resulting mixture were found to be suspended uniformly. An electrolyte film cast from this mixture exhibited remarkable dimensional stability. In thermal-creep measurements, the $PEO/Al_2O_3/LiI$ film was found to be more stable than was a similar film that did not contain alumina particles (see figure).

This work was done by Ganesan Nagasubramanian and Alan Attia of Caltech for **NASA's Jet Propulsion Laboratory**. *Further information is contained in a TSP [see page 1].*

This invention is owned by NASA, and a patent application has been filed. Inquiries concerning nonexclusive or exclusive license for its commercial development should be addressed to the Patent Counsel, NASA Resident Office-JPL [see page 1]. Refer to NPO-18877.

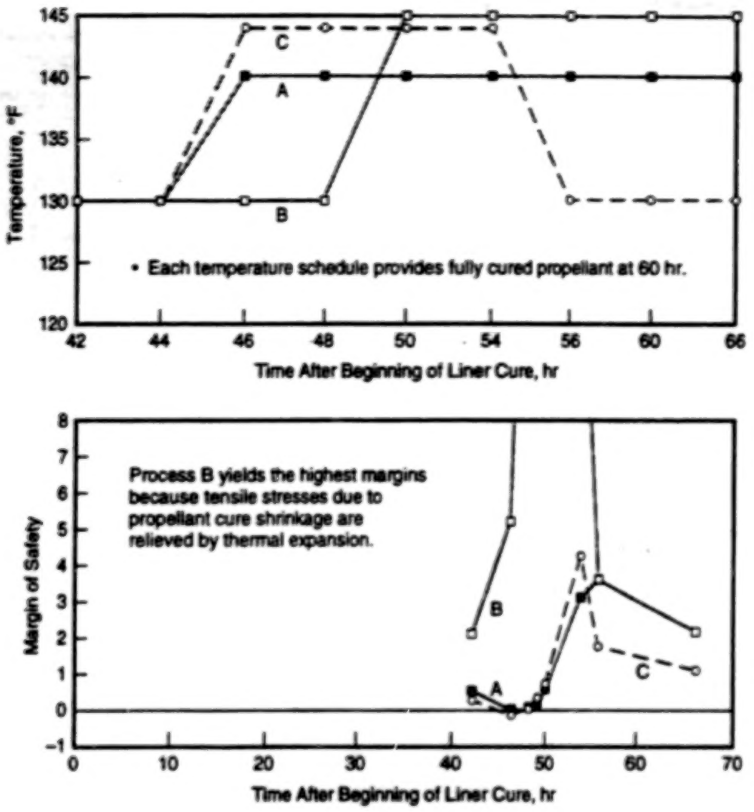
Mathematical Model of Curing Behavior of a Polymer

The model predicts chemical, thermal, and mechanical responses.

Marshall Space Flight Center, Alabama

A mathematical model predicts selected aspects of the chemical, thermal and mechanical responses of polymeric liner and propellant materials during a curing process. Predictions can be made both prior to processing and during the process in quasi-real time. The model was developed specifically for use in designing and analyzing a process in which bondline materials (including polymeric liners) and propellant are cast and cured in a rocket motor. With modifications, the model should be applicable to curing of other polymeric materials.

The one-dimensional model is incorporated in a computer program having three basic modules: (1) a process environment model (PEM) that predicts the current state of cure of the material as well as its chemical and thermal responses; (2) a process mechanical model (PMM) that uses data calculated by the PEM to predict stresses, strains and displacements; and (3) a process assess-



Three Equivalent Curing Processes defined by different temperature schedules were applied to a conceptual rocket motor and analyzed by use of the mathematical model described in the text. The lower plot shows the predicted critical margin of safety history for each process (failure is indicated when the margin of safety falls to zero). Process B would be selected.

ment model (PAM) that evaluates the chemical, thermal and mechanical responses.

The model can be used to design curing processes that can potentially help reduce the variability of properties often observed in both propellant and bondline materials. This is accomplished by using the model to assess trial process temperature schedules that can alleviate tensile stresses that develop in the bond system due to propellant cure shrinkage. Proper selection of a process schedule will ensure that propellant and bondline tensile stresses due to chemical shrinkage are sufficiently counterbalanced by compressive thermal stresses (caused by increasing the cure temperature after the gel point is reached). To avoid possible processing problems, any net tensile stresses must be kept below the current propellant and bondline strengths. This may necessitate the use of nonisothermal process schedules (see figure). Until now, standard practice in the industry has been to process materials at constant temperatures.

Inasmuch as the simulation of an entire process takes only a few minutes, whereas the actual process often takes days, it is possible to make in-process predictions in quasi-real time. This is done using the actual process temperature to drive model predictions of conditions at the locations of dielectric gauges, thermocouples and stress sensors. Comparison of predicted and measured responses then provides a more comprehensive understanding of bondline property variations and stress states during the process. Further development may provide a direct "in-line" program for calculations, including comparisons, in real time. This will constitute a basis for more sophisticated control of the process.

This work was done by Willard C. Loomis of Science Applications International Corp., Rodney B. Beyer of Atlantic Research Corp., and Edmund K. S. Liu of GenCorp Aerojet for **Marshall Space Flight Center**. *Further information is contained in a TSP [see page 1].*

Inquiries concerning rights for the commercial use of this invention should be addressed to the Patent Counsel, Marshall Space Flight Center [see page 1]. Refer to MFS-28876.

Hydrophobic Catalysts for Removal of NO_x From Flue Gases

These catalysts would not be adversely affected by water vapor and sulfur oxides.

NASA's Jet Propulsion Laboratory, Pasadena, California

Improved catalysts for the removal of nitrogen oxides (NO and NO_2) from combustion flue gases would be formulated as composites of vanadium pentoxide in carbon molecular sieves. These catalysts are expected to promote the highly efficient selective catalytic reduction of NO_x at relatively low temperatures while not being adversely affected by the presence of water vapor and sulfur oxide gases in the flue gas. An apparatus that utilizes a catalyst of this type could be easily integrated into the exhaust stream of a power plant (see figure) to remove nitrogen oxides, which are generated in the combustion of fossil fuels and which contribute to the formation of acid rain and photochemical smog (or ozone, which is a pollutant in the lower atmosphere).

Similar to catalysts that have been developed previously for the same purpose, these would promote the reduction of NO_x by ammonia that had been injected into the flue gas. The main chemical reactions for the removal of NO_x are

$$6NO + 4NH_3 \rightarrow 5N_2 + 6H_2O,$$

$$4NO + 4NH_3 + O_2 \rightarrow 4N_2 + 6H_2O,$$

and

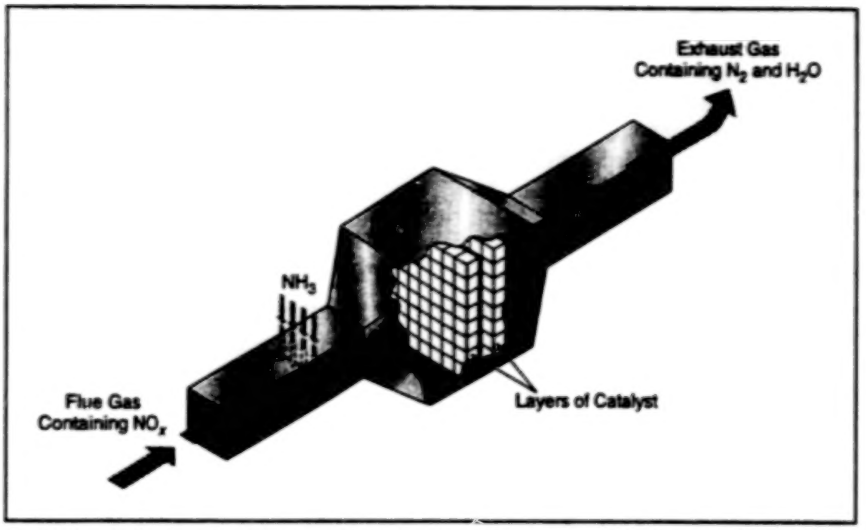
$$NO + NO_2 + 2NH_3 \rightarrow 2N_2 + 3H_2O.$$

Vanadium pentoxide (V_2O_5) is known to be a good catalyst for these reactions. However, the water vapor produced in these reactions has an unfavorable effect on the reduction equilibrium. In addition, the combustion of fuels that contain sulfur produces SO_2, and the catalyst promotes the conversion of a small amount of the SO_2 to SO_3. Then the reaction of NH_3 with SO_3 and H_2O produces $(NH_4)_2SO_4$ and NH_4HSO_4, which eventually accumulate in sufficient quantity to clog the pores of the catalyst support and thereby deactivate the catalyst. This process limits the life of the catalyst which requires either the

replacement or regeneration of the catalyst. Thus, it would be desirable to develop a hydrophobic catalyst to minimize the effect of water vapor and at the same time make the catalyst minimally susceptible to clogging by sulfates and thereby extend the life of the catalyst.

Although not usually hydrophobic, activated charcoal can catalyze the reduction of NO_x at temperatures as low as 100 °C. Recently, carbon molecular sieves (which are hydrophobic) have been put to new use in separation and purification of gases. Carbon molecular sieves offer an improvement over activated charcoal because of their molecular-sieving characteristics, hydrophobicity, and potentially larger surface areas. Thus, it is proposed to disperse V_2O_5 on high-surface-area supports to obtain fast chemical kinetics and to use carbon molecular sieves as such supporting materials to obtain very effective catalysts for the reduction of NO_x.

It should be possible to prepare the proposed catalysts by a modified version of a method used previously to make a hydrophobic composite of silicalite and carbon molecular sieve for removal of selected organic compounds. In addition, carbon molecular sieves can be made with pore sizes of 3 to 4.0 Å, so that it should be impossible for SO_2 and SO_3 (and heavy aromatics, if present) to enter the pores, as their respective sizes are greater than 4.0 Å. This will prevent the formation of sulfates inside the pores.



A Catalyst in the Flue would promote the reduction of NO_x by ammonia to harmless N_2 and H_2O.

It is expected that V_2O_5/carbon-molecular-sieve catalysts will function in the temperature range 175 to 350 °C, where there is a significant reduction of NO_x. Operation at the low end of this temperature range should be possible without encountering plugging of pores or poisoning of the catalysts. The high temperature limit reflects the possible oxidation of carbon in the catalyst at temperatures above 350 °C.

This work was done by Pramod K. Sharma, Gregory S. Hickey, and Gerald E. Voecks of Caltech for **NASA's Jet Propulsion Laboratory**. *Further information is contained in a TSP [see page 1].*
NPO-19474

Wire-Arc-Sprayed Aluminum Protects Steel Against Corrosion

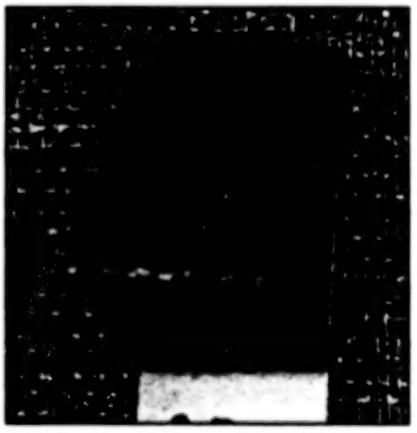
Unlike some paints, aluminum coatings do not emit chromium and volatile organic compounds.

Marshall Space Flight Center, Alabama

Aluminum coatings wire-arc sprayed onto steel substrates have been found to be effective in protecting the substrates against corrosion. These aluminum coatings also satisfy stringent requirements for adhesion and flexibility, both at room temperature and at temperatures as low as that of liquid hydrogen [–423 °F (–253 °C)]. The wire-arc-sprayed aluminum coatings were developed as alternatives to corrosion-inhibiting primers and paints that are required by law to be phased out because they contain and emit such toxic substances as chromium and volatile organic compounds.

Wire-arc spraying offers important advantages over other thermal deposition processes and over painting. Unlike in painting, there is no need for drying or curing time. In comparison with other thermal processes, the substrates can be kept at relatively low temperatures, and rates of deposition are high.

An aluminum coating forms a galvanic cell with a steel substrate, the steel acting as the cathode and the aluminum as the anode. In this arrangement, the aluminum corrodes preferentially, thus protecting the steel.



This Specimen Was Bent and subjected to a tape-pull test, without cracking or loss of adhesion of its wire-arc-sprayed aluminum coating.

In an experiment, aluminum coatings were wire-arc-sprayed on plates and on a duct made of 21-6-9 corrosion-resistant steel, then the plates and duct were tested as follows:

- Adhesion and flexibility at room temperature. The aluminum coating did not crack when the plate was bent around a mandrel of 0.3-in. (7.6-mm) diameter. The plate was then subjected to a tape-pull test, and the coating continued to adhere (see figure).
- Adhesion and flexibility at low temperature. A plate submerged in liquid nitrogen at –320 °F, (–196 °C) was bent around a mandrel of 2.8-in. (71-mm) diameter without cracking or loss of adhesion of the aluminum coat.
- Resistance to corrosion. Plates survived 120 days in a salt fog, without corrosion or pitting of the substrate.
- Thermal shock. By turning a flow of liquid hydrogen on and off, the duct was thermally cycled to –423 °F (–253 °C) 17 times in 16 hours. The aluminum coating did not crack or lose adhesion.

The optimum aluminum-coating thickness has been found to lie between 0.004

and 0.008 in. (between 0.1 and 0.2 mm). Thicker coats are less flexible and tend to blister in salt-fog tests. Grit blasting to prepare substrates for adhesion of wire-arc sprayed aluminum is unnecessary and may be unacceptable in situations in which substrates are required to be smooth; hand sanding has been found to result in the required degree of adhesion.

This work was done by Frank R. Zimmerman and Richard Poorman of **Marshall Space Flight Center** *and Heather L. Sanders, Timothy N. McKechnie, James W. Bonds, Jr., and Ronald L. Daniel, Jr., of Rockwell International Corp. Further information is contained in a TSP [see page 1].*

Inquiries concerning rights for the commercial use of this invention should be addressed to the Patent Counsel, Marshall Space Flight Center [see page 1]. Refer to MFS-30044.

Eutectic-Free Superalloy Made by Directional Solidification

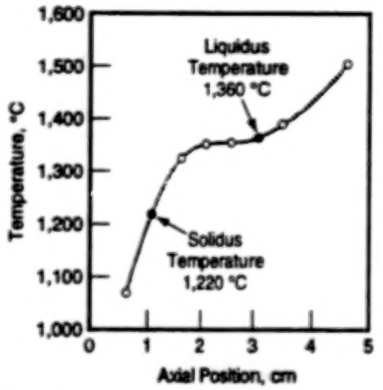
Resistance to fatigue is enhanced.

Marshall Space Flight Center, Alabama

By suitable control of the thermal conditions in a directional-solidification process, superalloy structural and machine components (e.g., turbine blades) can be cast with microstructures that enhance resistance to fatigue. The specific version of the process and the thermal conditions are chosen to reduce microsegregation during solidification and to minimize or eliminate script carbide and eutectic-phase inclusions, which are brittle inclusions that have been found to decrease resistance to fatigue.

Numerous variations on the basic directional-solidification theme have been described previously in *NASA Tech Briefs*. Typically, a batch of the alloy in question is melted under an inert atmosphere in a cylindrical crucible, then progressively resolidified, from one end to the other. This is accomplished by use of a hollow cylindrical furnace that fits closely but loosely around the crucible and translates along the crucible.

The melt-zone temperature and the axial gradient of temperature at and near the moving solidification front affect the microstructure of the solidified alloy. To make it possible to tailor the spatial distribution of temperature to optimize the microstructure, the furnace is constructed with a chilling block at one end, plus multiple, axially spaced heaters that can be maintained at different temperatures. The speed of translation also affects the outcome and should be adjusted accordingly.



This Axial Temperature Profile, translated along a specimen of Mar-M246(Hf) at a speed of 30 cm/h, produces a eutectic-free microstructure that imparts high resistance to fatigue.

The concept has been verified in experiments on the nickel-base superalloy Mar-M246(Hf). The figure shows the axial temperature profile that, along with a rate of translation of 30 cm/h, has been found to give the best results for this alloy. Specimens that were directionally solidified under these conditions exhibited microstructures with small, closely spaced dendrite arms (which inhibit microsegregation); fine, blocky carbides; and no eutectic phase. These directionally solidified specimens were also heat treated and subjected to high-cycle-fatigue tests. Statistical analysis of the results of these tests revealed that these specimens had fatigue lives about ten times those of other specimens of the same alloy that were directionally solidified in the same furnace with a nonoptimum temperature profile.

This work was done by Deborah Dianne Schmidt of **Marshall Space Flight Center**. *Further information is contained in a TSP [see page 1].*

MFS-31030

Polyimides Made From PDMDA

Advantages over commercial polyimides include lower dielectric constants and greater degrees of transparency.

Langley Research Center, Hampton, Virginia

Thermally stable linear aromatic polyimides with improved optical, electrical, and processing characteristics have been made from 3,3′-bis(3,4-dicarboxyphenoxy)diphenylmethane dianhydride (PDMDA). These polyimides can be made in the form of powders that can be dissolved to cast thin films. They are potentially useful as coating and matrix materials. Films made of these polyimides vary from transparent to pale yellow, whereas typical commercial polyimides are bright yellow. The dielectric constants of these polyimides at a frequency of 10 GHz range from 2.7 to 3.1 (vs. 3.2 to 4.0 for typical commercial polyimides). The greater degrees of transparency and lower dielectric constants make these polyimides more suitable for use in some electronic and optical applications; e.g., as insulating materials on wires and protective films on solar photovoltaic cells.

Figure 1 illustrates the synthesis of PDMDA. In the first three steps, 3,3′-diaminophenylmethane is converted to a disodium bisphenol salt. The salt is reacted with 4-nitro-N-phenylphthalimide, the products of this reaction are refluxed in NaOH to remove the bis-aniline, and the remaining product is hydrolyzed to convert it to a tetracarboxylic acid. The acid, in turn, is reacted with acetic anhydride. The PDMDA precipitates and is dried in vacuum.

Figure 2 illustrates the synthesis of a polyimide from PDMDA. An aromatic diamine in an amide solvent is mixed with an equal molar portion of PDMDA and the mixture is stirred at ambient temperature in a closed vessel. The reaction between the aromatic diamine and the PDMDA forms a polyamic acid, which can be converted to the polyimide and used in either of two ways: The solution of polyamic acid and amide solvent can be cast into a thin film, then heated to evaporate the solvent and thermally convert the polyamic

acid film to the desired polyimide film. Alternatively, the polyamic acid in solution can be chemically imidized and precipitated to obtain the polyimide in the form of a powder, which can later be redissolved and applied as a coating or film.

This work was done by Anne K. St. Clair of **Langley Research Center** *and Harold G. Boston and John R. Pratt of Lockheed Engineering & Sciences Corp. Further information is contained in a TSP [see page 1].*

This invention has been patented by NASA (U.S. Patent No. 5,218,077). Inquiries concerning nonexclusive or exclusive license for its commercial development should be addressed to the Patent Counsel, Langley Research Center [see page 1]. Refer to LAR-14487.

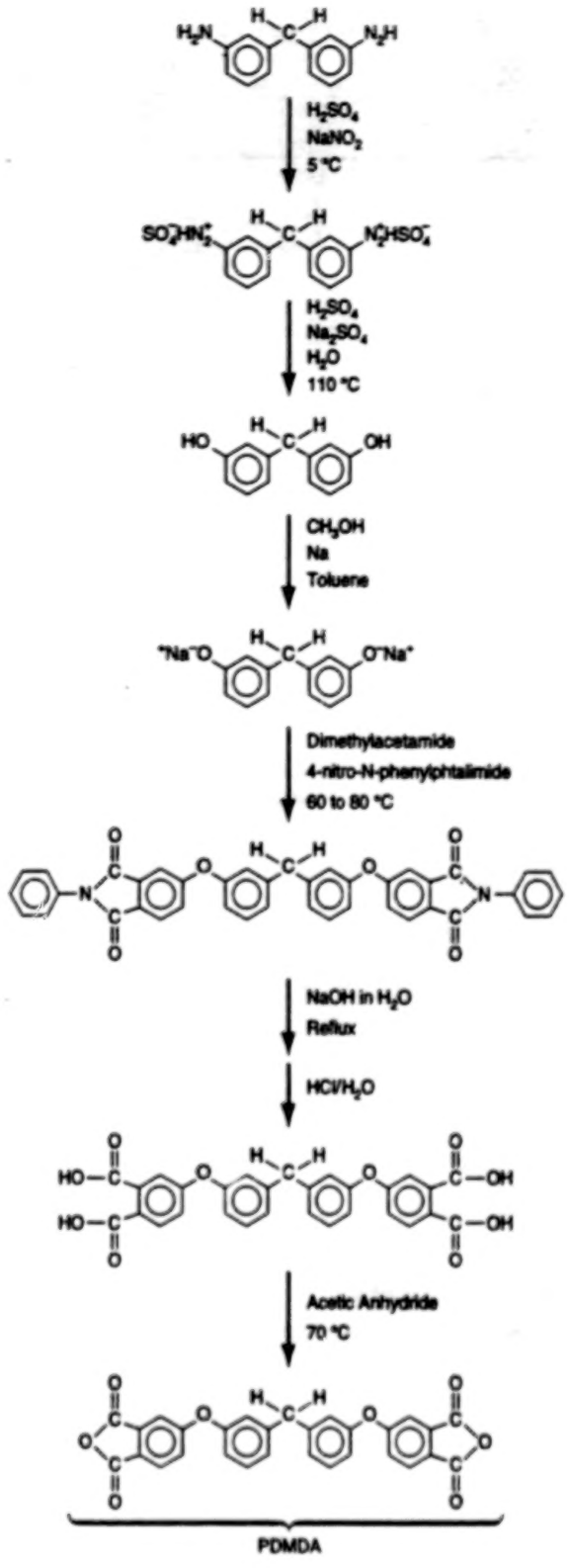


Figure 1. The **Cyclic Dianhydride PDMDA** is produced in this sequence of reactions. The PDMDA is used as a monomeric ingredient in the synthesis of novel linear aromatic polyimides that have relatively low dielectric constants and enhanced optical clarity.

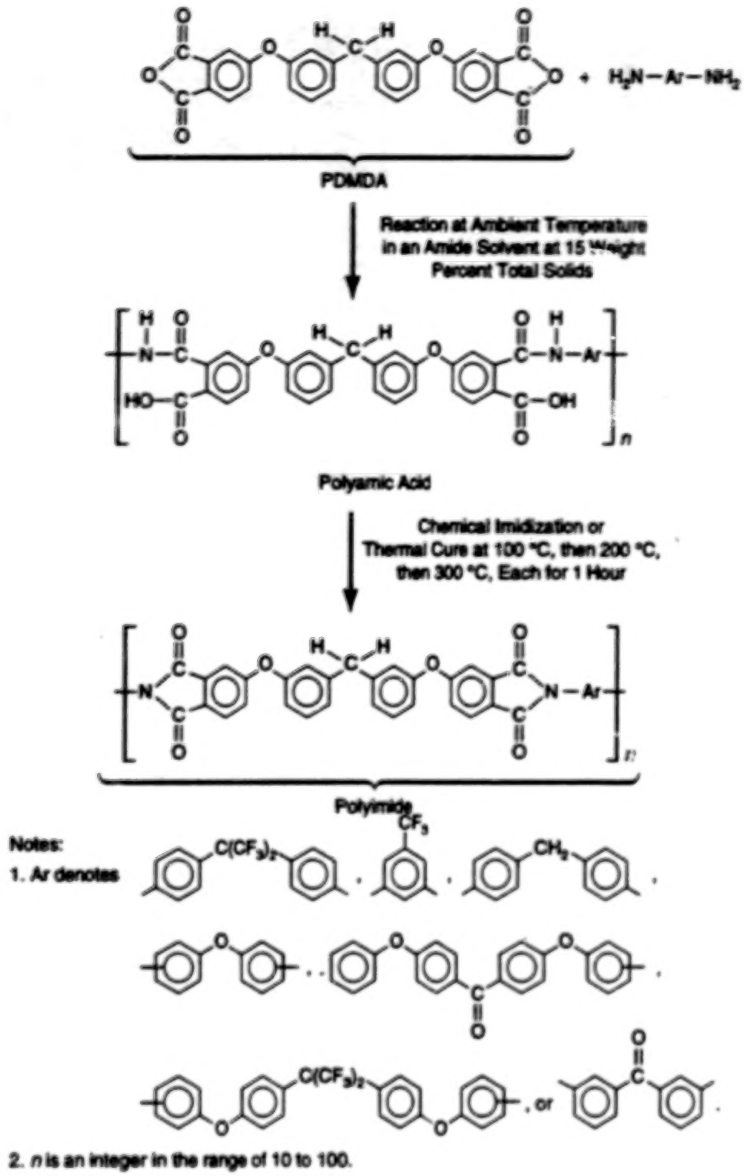


Figure 2. A **Linear Aromatic Polyimide** is synthesized from PDMDA in this sequence of reactions.

Books and Reports

Stress in a Fiber During Curing of Surrounding Matrix Resin

Causes of residual stresses in matrix/fiber composites are investigated.

Experiments were run to determine the variation in tensile stress in a single fiber during curing of a matrix resin that surrounds the fiber. This study is part of an effort to understand the physical mechanisms that affect residual stresses in matrix/fiber composites, with a view toward optimizing curing cycles (in particular, optimizing the temperature-vs.-time schedules of final cooldowns to ambient temperature) to minimize the residual stresses. In each experiment in this study, a single glass or graphite fiber was laid out straight in a silicone mold with its ends sticking out, and the ends were gripped to place the fiber under a prescribed initial tension between two anchor points, one of which was a load cell used to measure tension. A two-part (resin/hardener) epoxy mixture was poured into the mold, and the variation in tension with time was measured as the mold was heated electrically according to a curing schedule that called for 2 h at a temperature of 75 °C followed by 2 h at 125 °C followed by cooldown to room temperature. The results of these experiments were interpreted as signifying that the primary mechanisms that affect the residual stress in fibers are (1) thermal expansion and contraction and (2) cure shrinkage of the matrix material.

This work was done by Kenneth J. Bowles of **Lewis Research Center** *and Madhu S. Madhukar and Ranga P. Kosuri of the University of Tennessee. No further documentation is available.*
LEW-15995

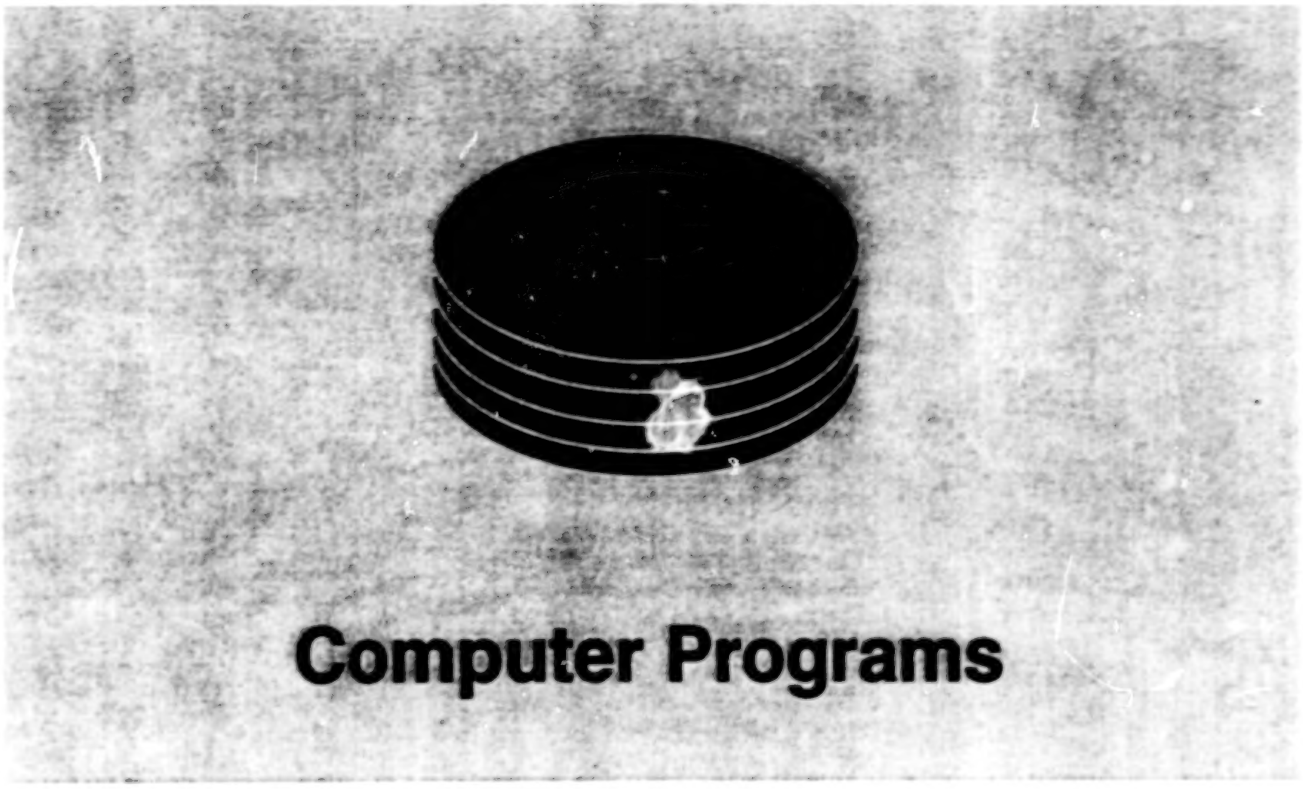
Performance of Perfluoropolyalkylether Lubricant System

Liquid and solid lubricants can both be utilized to reduce friction and wear of bearing surfaces. Liquid lubricants have some advantages which include long life in high cycle applications, high thermal conductivity and low coefficients of friction. Liquid lubricants can also be resupplied as they are consumed. Natural liquid lubricants, while being readily available have some severe shortcomings, e.g., temperature limitations and viscosity fluctuations. The U. S. space program has traditionally used liquid lubricants, but their shortcomings have been a catalyst in the development of a series of synthetic liquid lubricants. Perfluoropolyalkylethers (PFPAE) constitute a class of such fluids. These PFPAE fluids have characteristics that include (1) high thermal oxidative stability, (2) good viscosity-temperature characteristics, (3) good elastohydrodynamic film-forming capabilities, (4) low volatility, and (5) nonflammability. One unfortunate drawback is that PFPAE causes severe metal corrosion and fluid degradation when used in an oxidizing atmosphere.

The reports of interest that are the subject of this brief deal with the synthesis of PFPAE-type liquids and the development of an additive to reduce oxidizing atmosphere degradation. The first report deals with the development of a modified phospha-s-triazine that is hydrolytically stable. When used as an additive to PFPAE, it prevents fluid degradation and metal corrosion in an oxidizing environment. The second report describes the synthesis of four high molecular weight PFPAE-type fluids using a direct fluorination process. The properties and molecular structures are reported in detail. Lubricant performance over a range of conditions is reported in detail.

This work was done by K. Paciorek, S. Masuda, and Wen-Huey Lin of Technolube Products Co. and T. Bierschenk, H. Kawa, T. Juhlke, and R. Lagow of Exfluor Research Corp. for **Lewis Research Center**. *To obtain copies of the reports, "Phospha-S-Triazines of Improved Hydrolytic and Thermal Oxidative Stability" and "Physical and Chemical Properties of Some New Perfluoropolyalkylether Lubricants Prepared by Direct Fluorination," see TSP's [page 1].*
LEW-15603

BLANK PAGE



Computer Programs

Electronic Components and Circuits

41 Program Predicts Mixer Intermodulation Products

Materials

41 Program Helps Generate Boundary-Element Mathematical Models

Mechanics

42 P-Finite-Element Program for Analysis of Plates

Mathematics and Information Sciences

42 Program Computes SLM Inputs To Implement Optimal Filters

43 Program for Analyzing Failures in a Complex System

43 Mapping Vegetative Ground Cover from Polarimetric SAR Data

Computer Programs

These programs may be obtained from COSMIC. Please contact

COSMIC®
Computer Services Annex
University of Georgia
Athens, GA 30602
Telephone No. (404) 542-3265.

Electronic Components and Circuits

Program Predicts Mixer Intermodulation Products

This interactive program aids design and analysis of frequency converters.

IMODP is a computer-aided-design (CAD) software tool useful in the analysis and design of frequency-conversion schemes. Frequency conversion or mixing is an essential function in communication receivers, down-converters, and transmitters. IMODP analyzes the intermodulation products created by mixing of (1) harmonics of a local-oscillator (LO) signal with (2) harmonics of another radio-frequency (RF) signal. Such mixing results in signal components in the intermediate-frequency (IF) range above the required rejection level.

IMODP is highly interactive with the user. The user is prompted for inputs and is provided outputs in real time on the screen. In addition, IMODP creates a file in which the output is saved. The inputs that IMODP accepts are the ranges and increments of the frequencies of the LO and the other RF signal, the nominal IF and the IF bandwidth, the shape of the IF filter, the required level of rejection of intermodulation products, the highest (up to 10) order of harmonic to be calculated, and the specific mixer intermodulation-product-suppression table. The user can insert a new table (guided by the program) or select one of the standard tables provided.

In order to facilitate the efficient iteration process necessary for complex frequency schemes, the program provides configuration files that store last-run inputs. The program offers last-run values as default inputs so that the only parameters that must be entered are those with new values.

Output from IMODP consists of a list of all input parameters and a list of all the frequencies and levels of all intermodulation products, the levels of which exceed the required suppression levels. The suppression that is calculated includes the mixer suppression as well as the IF-band-pass-filter rejection. This filter is assumed to have zero loss in the pass band and linear slopes with respect to frequency.

IMODP is written in Microsoft FORTRAN for IBM PC-series and compatible computers running MS-DOS. This software package includes a sample executable code compiled by use of Microsoft FORTRAN v4.0. IMODP requires approximately 36K of random-access memory for execution. The standard distribution medium for this program is a 3.5-in. (8.89-cm), 1.44MB, MS-DOS-format diskette. Documentation is included in the price of the program. IMODP was developed in 1993 and is a copyrighted work with all copyright vested in NASA.

This program was written by Dalia McWatters of Caltech for **NASA's Jet Propulsion Laboratory**. *Further information is contained in a TSP [see page 1].*
NPO-19379

Materials

Program Helps Generate Boundary-Element Mathematical Models

Time and effort are reduced significantly.

The Composite Model Generation-Boundary Element Method (COMGEN-BEM) computer program, which was developed in PATRAN Command Language (PCL), can significantly reduce the time and effort needed to construct boundary-element mathematical models of continuous-fiber composite materials at the micromechanical (constituent) scale. Heretofore, in conducting a boundary-element analysis, it was necessary to expend much time and effort in constructing such a model, either manually or by use of a graphical preprocessor. As it saves time and reduces effort, COMGEN-BEM generates boundary-element models that are compatible with the BEST-CMS boundary-element code for analysis of the micromechanics of a composite material.

COMGEN-BEM operates within the computing environment of the PATRAN graphical preprocessor software. COMGEN-BEM generates boundary-element models based on several parameters supplied by the user. Geometric data input includes type of model, fiber volume fraction, diameter of fibers, and thickness of the model. Data on the density of the computational mesh are entered by the user, along with data on properties of materials, orientations (that is, angles) of fibers, and boundary conditions. On the basis of these data, COMGEN-BEM executes the PATRAN model-generation commands required to generate an appropriate boundary-element model.

To request data from the user, COMGEN-BEM issues interactive prompts during execution. The program automatically checks, in most cases, to ensure that a valid parameter has been supplied, and at several points it echoes input data and prompts the user to indicate whether the entered parameters are correct. Once the program completes execution, the generated model is plotted on the computer video screen, and the user can then apply the user's own translator program to convert the model data into an appropriate BEST-CMS input-file format.

COMGEN-BEM is written in PATRAN Command Language (PCL) for use on any computer running PATRAN v2.5. For information on PATRAN v2.5, write to MacNeal-Schwendler Corporation, 815 Colorado Blvd. Los Angeles, CA 90099. This program requires 360K of random-access memory for execution. The documentation for COMGEN-BEM consists of NASA Technical Memorandum 105548 and an addendum, and is available in hard copy as well as in ASCII electronic form on the distribution medium. The figures included in the NASA Technical Memorandum, however, are not included in the electronic documentation. The standard medium for distribution of COMGEN-BEM is a 3.5-in. (8.89-cm) diskette in UNIX tar format. Alternate distribution media and formats are available upon request. COMGEN-BEM was developed in 1993.

This program was written by R. K. Goldberg of **Lewis Research Center**. *Further information is contained in a TSP [see page 1].*
LEW-15874

Mechanics

P-Finite-Element Program for Analysis of Plates

Results can be more accurate than in the h-finite-element method.

BUCKY is a p-finite-element computer program for highly accurate analysis of structures. BUCKY can be used to analyze the buckling, bending, and in-plane stress-and-strain behaviors of plates. BUCKY provides elastic-plastic solutions for isotropic plates in states of plane stress, and an axisymmetric solution sequence that can be used to treat three-dimensional problems. BUCKY computes the response of a plate to a variety of loading and boundary conditions by use of a higher-order displacement function in the p-finite-element method. Several h-elements can be replaced by a single p-element. In addition, the high order of the displacement functions enables the user to obtain results more accurate than those obtained by the use of traditional h-finite elements.

The user can choose among plane stress, plate bending (Kirchhoff or Reissner-Mindlin theory), plate buckling, two-dimensional plane-stress plasticity, and three-dimensional axisymmetric analysis. In the current version of BUCKY, the thickness of a plate can vary linearly in the spatial coordinates. In addition, the user can prescribe pressure loads, distributed edge moments, or edge tractions that are constant, linear, or quadratic in behavior. For plate bending, loads can also be applied in the form of concentrated point loads. BUCKY also supports orthotropic as well as isotropic material properties at the element level.

BUCKY is written in FORTRAN 77 for UNIX-based computers. It has been successfully implemented on HP9000-series 700/800 computers running HP-UX 8.07, Sun4-series computers running SunOS 4.1.1, SGI IRIS-series computers running IRIX 5.2, and CRAY Y-MP-series computers running UNICOS 5.1. COSMIC was unsuccessful in implementing BUCKY on a DECstation 3100 computer running DEC RISC ULTRIX 4.3. BUCKY requires 5MB of disk space for installation. The amount of random-access memory (RAM) needed varies with the size of the problem being solved; however, 10MB of RAM is needed for this version of the source code. In addition to primary output files, BUCKY produces PATRAN and I-DEAS Universal output files for post-processing. An electronic version of the documentation is included on the distribution medium in PostScript format. The standard distribution medium for BUCKY is a 0.25-in. (6.35-mm) streaming-magnetic tape cartridge (Sun QIC-24) in UNIX tar format. BUCKY was originally developed in 1992 and released in 1994.

This work program was written by James P. Smith of **Johnson Space Center.** *Further information is contained in a TSP [see page 1].*
MSC-22470

Mathematics and Information Sciences

Program Computes SLM Inputs To Implement Optimal Filters

MEDOF optimizes values for filters in optical correlators.

The Minimum Euclidean Distance Optimal Filter (MEDOF) program generates filters for use in optical correlators. The algorithm implemented in MEDOF follows the theory put forth by Richard D. Juday in "Optimal realizable filters and the minimum Euclidean distance principle," *Applied Optics*, Vol. 32 (September 10, 1993), pp. 5100-5111. This program analytically optimizes filters on arbitrary spatial light modulators (SLMs) of such types as coupled, binary, fully complex, and fractional-2π-phase. MEDOF optimizes filters constructed on these modulators for a number of metrics including the following:

- Intensity of the correlation peak at the origin for the centered appearance of the reference image in the input plane,
- The signal-to-noise ratio (SNR), including the correlation-detector noise as well as the colored additive input noise;
- The peak-to-correlation-energy ratio (PCE) defined as the fraction of the signal energy passed by the filter that shows up in the correlation spot; and
- The peak-to-total-energy ratio, which is a generalization of PCE in which the passed colored input noise is added to the passed energy of the input image.

The user of MEDOF supplies the functions that describe the following quantities:

- The reference signal;
- The realizable complex encodings of both the input and filter SLM;
- The noise model, possibly colored, as it adds at the reference image and at the correlation detection plane; and
- The metric to analyze, here taken to be one of the analytical ones like SNR or PCE. MEDOF does not directly optimize such nonanalytic metrics as the peak-to-secondary ratio.

MEDOF examines the statistics of the noise of the encoded input (if SNR or PCE is selected) and the available values of the filter SLMs. These statistics are used to determine a range for searching for the magnitude and phase of k, a pragmatically based complex constant necessary for computing the optimal filter. The filter is produced for the mesh points of k and the value of the metric that results from these points is computed. When the search is concluded, the values of amplitude and phase of that k, the metric of which is largest, as well as consistency checks, are reported.

A finer search can be done in the neighborhood of the optimal k if desired. The filter finally selected is written to disk in terms of voltages to be applied to SLMs, not in terms of the complex transmittance of the filter. Optionally, the impulse response of the filter can be created to enable the user to examine the responses in the cases of the features the algorithm selects as important to the recognition process under the selected metric, limitations of the filter SLM, etc. Because MEDOF uses the filter SLM to its greatest potential, the filter competence is not compromised for simplicity of computation.

MEDOF is written in C language for Sun-series computers running SunOS. With slight modifications, it has been implemented on DEC VAX-series computers using the DEC-C v3.30 compiler, although the documentation does not currently support this implementation. MEDOF can also be compiled by use of Borland International, Inc., Turbo C++ v1.0, but IBM PC memory restrictions greatly reduce the maximum size of the reference images from which the filters can be calculated. MEDOF requires a two-dimensional fast Fourier transform (2DFFT). One 2DFFT routine that has been used successfully with MEDOF is a routine found in "Numerical Recipes in C: The Art of Scientific Programming," which is available from Cambridge University Press, New Rochelle, NY 10801. The standard distribution medium for MEDOF is a 0.25-in. (6.35-mm) streaming-magnetic-tape cartridge (Sun

QIC-24) in UNIX tar format. MEDOF was developed in 1992-1993.

This program was written by R. Shane Barton, Richard D. Juday, and Jennifer L. Alvarez of **Johnson Space Center**. *Further information is contained in a TSP [see page 1].*
MSC-22380

Program for Analyzing Failures in a Complex System

CRANS facilitates rapid logic-tree analysis.

The Configurable Real-Time Analysis System (CRANS) computer program provides means for representing logically interconnected items (e.g., modules of equipment in a complicated system) in a matrix format. Capabilities like those provided by CRANS can be helpful in a real-time environment (e.g., the operational environment of such a system), in which there is a need for quick evaluation of the results of changes or failures.

Tabulations that show the effects of changes and/or failures of a given item in the system are generally useful only for a single input, and only with regard to that item. Subsequent changes become more difficult to evaluate as combinations of failures produce a cascade effect. In the presence of multiple indicated failures in the system, it becomes necessary to determine a single cause. In this case, failure tables are not very helpful.

CRANS can interpret a logic tree that has been constructed by the user to describe a complex system and can determine the effects of changes and failures in the system represented by the logic tree. Items in the tree are related to each other by Boolean operators. The user is then able to change the states of these items (ON/OFF FAILED/UNFAILED). The program then evaluates the logic tree as thus amended and determines any resultant changes to other items in the tree. In this way, CRANS exceeds the capability of a simple failure table since multiple failures/changes can be input simultaneously. CRANS can also search for a common cause of failures of multiple items, and enables the user to explore the logic tree from within the program.

Display output is in the form of a matrix or matrices of colored boxes defined by the user, each box representing an item or set of items from the logic tree. Input is via mouse selection of the matrix boxes, using the mouse buttons to toggle the state of each affected item.

CRANS is written in C language and requires revision 4 or revision 5 of version 11 of the MIT X Window System. It requires 78K of random-access memory for execution (the amount of memory needed depends on the size of the logic tree), and a three-button mouse. It has been successfully implemented on Sun4 workstations running SunOS, HP9000 workstations running HP-UX, and DECstations running ULTRIX as well as on DEC Alpha, Silicon Graphics, and Masscomp 6600. No executable code is provided on the distribution medium; however, a sample makefile is included. Sample input files are also included. The standard distribution medium is a 0.25-in. (6.35-mm) streaming-magnetic-tape cartridge (Sun QIC-24) in UNIX tar format. Alternate distribution media and formats are available upon request. This program was developed in 1992. (The original version was developed in 1989.)

This program was written by R. Kevin McCluney of **Johnson Space Center**. *Further information is contained in a TSP [see page 1].*
MSC-21845

Mapping Vegetative Ground Cover from Polarimetric SAR Data

Three-frequency quad-polarization data are used to distinguish among different types of cover.

The MAPVEG computer program performs a first-level classification of NASA/JPL AIRSAR polarimetric synthetic-aperture-radar (SAR) data into simple ground-cover types. Classification images generated by MAPVEG can be used to separate vegetated from nonvegetated areas; this separation may be useful in determining the soil moisture in areas free of vegetation. MAPVEG classification can separate forests from the surrounding vegetation, and can be used to identify clear-cut areas, for example. Urban areas and potential marshlands are examples of other identifiable classes. MAPVEG images can be used in the first stage of a classification scheme more specific to a user's application. For example, having classified an area as one of low vegetation in an agricultural region, one might wish to go on to separate the area into crops of different types.

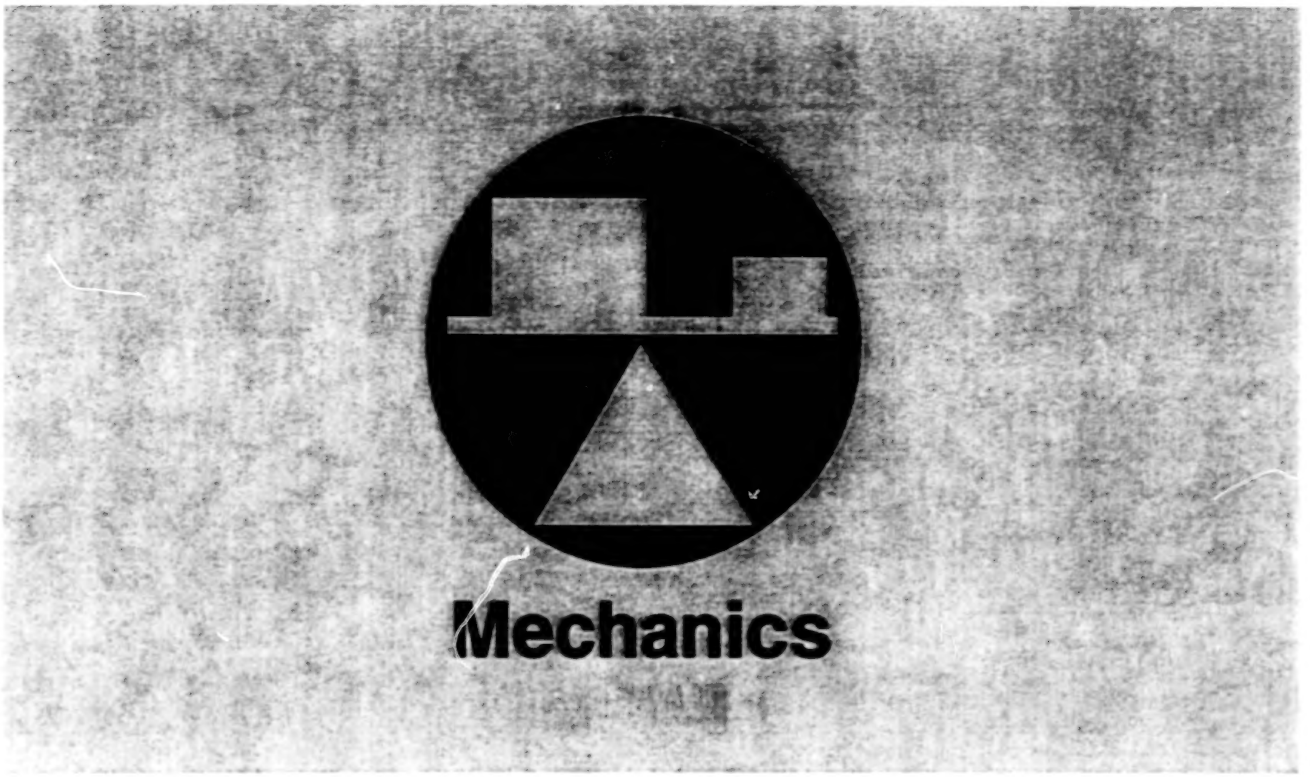
The classification algorithm in MAPVEG is based on a model fit to the AIRSAR data. This fit provides estimates of the contributions of surface, double-bounce, and volume scatter to the observed polarimetric radar signatures for each of the three wavelengths measured by the AIRSAR. After the model fit has been applied to the data, simple rules (established by training on different ground-cover signatures in just three AIRSAR images) are used to classify the results into one of several different ground cover types. The algorithm used is capable of distinguishing among areas with no vegetation cover, areas with low- and medium-level vegetation cover, forested areas, and urban areas. The three vegetated classes of ground cover are further subdivided into areas where double-bounce scatter is significant and areas where it is not.

The output from MAPVEG consists of a byte image with each class assigned to a different numerical value, plus a header that provides information on the dimensions of the image, a key to the numerical values, and a list of the percentages of the image assigned to each class. The image data are typically much fewer than are the original AIRSAR data (e.g., a 330KB image from 39MB of typical AIRSAR data) and can be easily displayed on a PC or on a Macintosh computer by use of standard image-processing software.

MAPVEG is written in FORTRAN 77 for Sun and DEC VAX computers. It has been successfully implemented on Sun4-series computers running SunOS 4.1.3 and Solaris 2.3, and DEC VAX-series computers running VMS 5.5. The program consists of a single source-code file to be compiled on the appropriate platform, and it requires 2MB of random-access memory for execution. MAPVEG is designed to be used with calibrated three-frequency-polarimetric NASA/JPL AIRSAR radar data in Stokes matrix format. The standard distribution medium for MAPVEG is a 0.25-in. (6.35-mm) streaming-magnetic-tape cartridge (Sun QIC-24) in UNIX tar format. Upon request, MAPVEG is also available in DEC VAX BACKUP format on a 1,600-bit/in. (630-bit/cm), 9-track magnetic tape or a TK50 tape cartridge. MAPVEG was developed in 1992 and is a copyrighted work with all copyright vested in NASA.

This program was written by Bruce Chapman and Anthony Freeman of Caltech for **NASA's Jet Propulsion Laboratory**. *Further information is contained in a TSP [see page 1].*
NPO-19335

BLANK PAGE



Hardware, Techniques, and Processes

47 Preload-Release Mechanism for Mounting Electronics Boxes
48 Self-Regulating Shock Absorber
49 Portable Device Measures Perpendicularity of Threaded Hole
50 Zip Boom

Books and Reports

50 Designing an Adaptor To Connect Rocket Stages
51 Vacuum Door for Testing a Spacecraft X-Ray Camera
51 Radiation Propulsion for Maintaining Orbits

BLANK PAGE

Preload-Release Mechanism for Mounting Electronics Boxes

The mechanism would maintain preload only briefly.

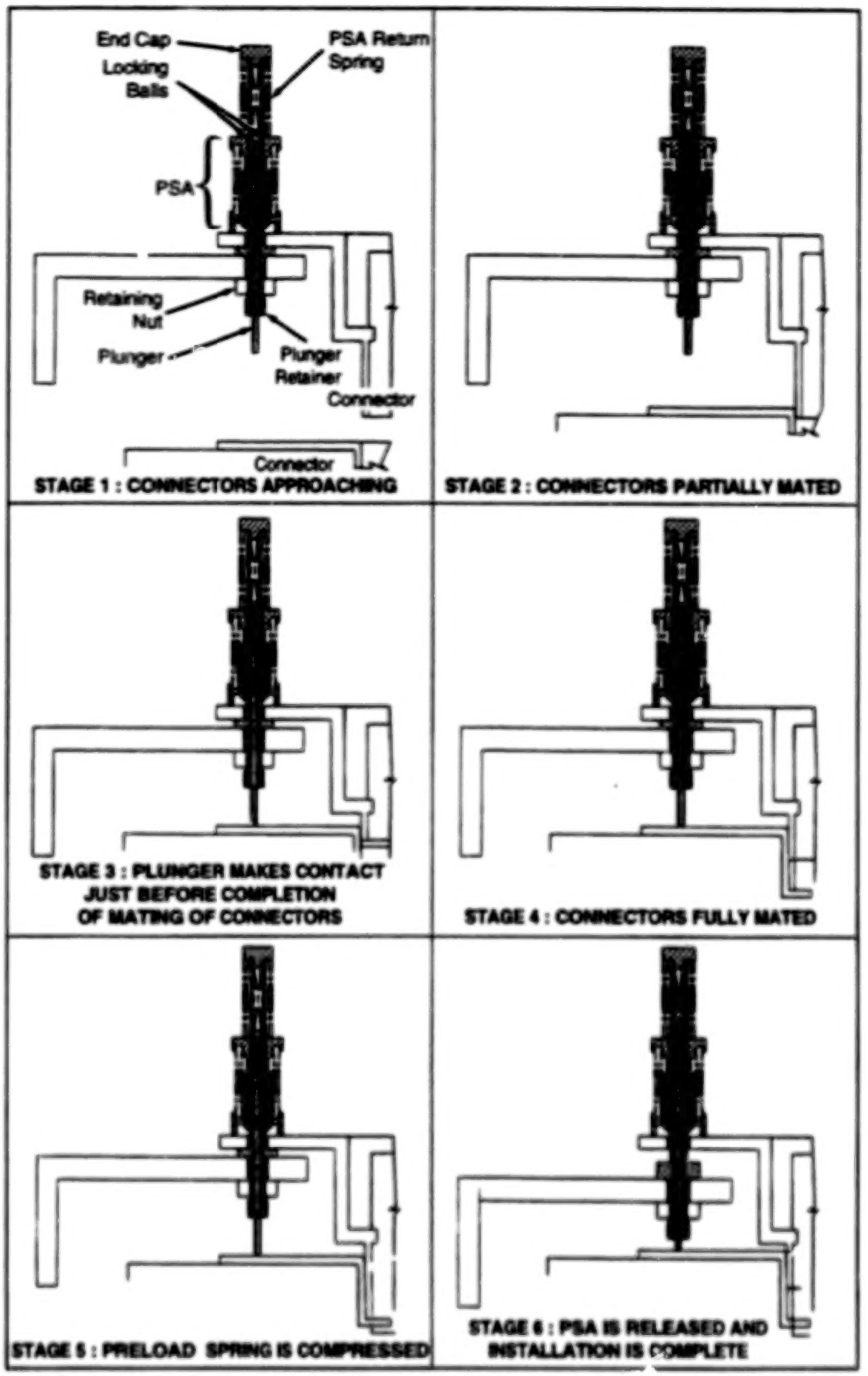
Lyndon B. Johnson Space Center, Houston, Texas

A proposed mechanism would apply a spring preload to an electrical connector only while it was needed — during insertion of an electronics box into a supporting frame. Once the connector was fully mated, the mechanism would relieve the preload. As a result, the supporting structure could be sized to handle only the individual load applied briefly by each connector on the box during insertion.

In electronic-equipment racks of the "blind-mate" design, spring forces are applied to the supporting structure as long as the boxes remain installed, even though preload is not needed once the connectors are fully engaged. The preload forces can be large, especially due to the dimensional tolerances in the boxes which the compression springs must be designed to accommodate. The force per spring can easily reach 85 lb (378 N), with as many as eight springs required for a large connector. The supporting structure must withstand the combined force of the springs in all connectors. Therefore, the structure must be stiffer, stronger, and heavier than it would have to be if the preload were removed once a box was installed.

In the proposed mechanism, the preload would be applied to a connector by a spring captured by a pair of bushings in a preload spring assembly (PSA). The PSA would slide on a shaft that would contain a plunger-operated release mechanism, much like the quick-release ball-lock-pin mechanisms commonly used in aerospace and military equipment.

Before installation of the box, the PSA would be locked in place on the shaft by locking balls (see figure). As the connectors began to mate, the PSA would remain locked, providing support for a connector plate. The external end of the plunger would make contact with the rear surface of the shortest possible electronics box approximately 0.03 to 0.06 in. (0.76 to 1.52 mm) before the connectors become fully engaged. As the box traveled the final 1/8 in. (about 3 mm) to its installed position, the preload spring would become compressed, and the plunger would be depressed. The resulting motion of the plunger would allow the locking balls to drop into the shaft; this would release the PSA, the resulting motion of which would, in turn, release the preload. The only remaining load on the connector support would be the few pounds (of the order of 10 N) provided by the PSA return spring. Boxes that were on the long side of the tolerance range would be accommodated by travel of the PSA beyond the locked position.



This Sequence of Events occurs during installation of an electronics box and mating of connectors. The mechanism is designed to accommodate the full dimensional range of manufacturing tolerances for a box of a given nominal size.

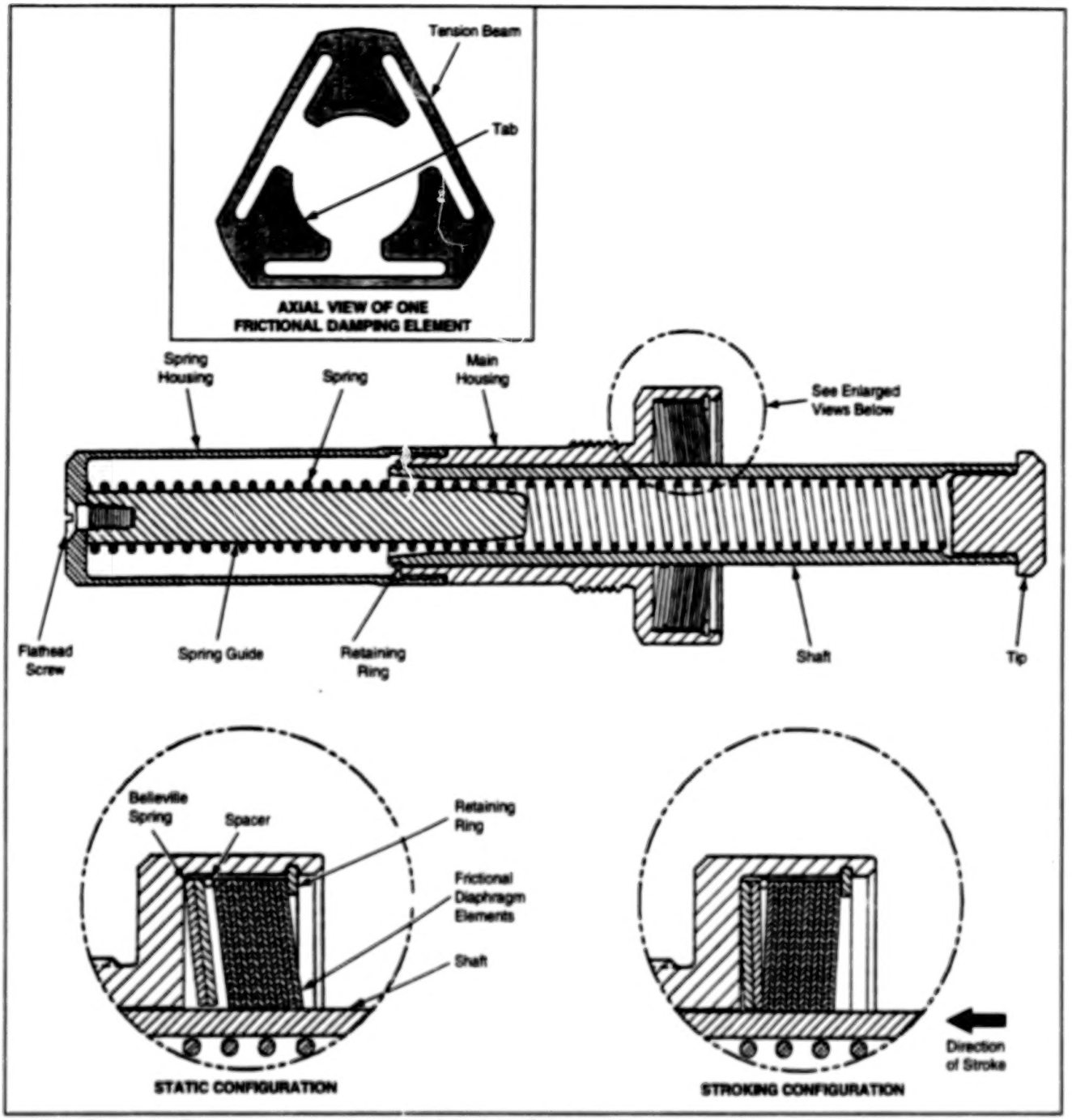
This work was done by Robert M. Generoli and Harry J. Young of McDonnell Douglas Corp. for **Johnson Space Center**. *Further information is contained in a TSP [see page 1].*

This invention is owned by NASA, and a patent application has been filed. Inquiries concerning nonexclusive or exclusive license for its commercial development should be addressed to the Patent Counsel, Johnson Space Center [see page 1]. Refer to MSC-22327.

Self-Regulating Shock Absorber

This device reduces its frictional damping force under overload.

Lyndon B. Johnson Space Center, Houston, Texas



Frictional Diaphragm Elements are tilted when the shaft is at rest. They are driven more nearly perpendicular to the shaft during stroking. Under excessive applied stroking load, they tilt in the opposite direction, reducing the frictional damping force.

A mechanical shock absorber keeps its frictional damping force within a tolerable limit. Unlike in other mechanical shock absorbers, its damping force does not increase with the coefficient of friction between its energy-absorbing components; rather, the frictional damping force varies only slightly—typically by 15 percent at most—as the coefficient of friction increases beyond a typical threshold value of about 0.1.

This shock absorber is relatively insensitive to manufacturing variations and environmental conditions that alter friction. Moreover, unlike some other mechanical shock absorbers, it does not exhibit high breakaway friction and the consequent sharp increase followed by a sharp decrease in damping force at the beginning of stroking. Also, unlike in hydraulic shock absorbers, the damping force in this shock absorber does not vary appreciably with speed of stroking. Of course, in addition, it is not vulnerable to leakage of hydraulic fluid.

The shock absorber (see figure) includes a main housing with a threaded

section that mates with the moving body to be stopped. The stroking component is a shaft that extends from the housing. A tip at the outer end of the shaft makes contact with a stationary hard stop. A retaining ring holds the shaft in the main housing. A spring in another housing is fastened to the opposite end of the main housing. The spring returns the shaft to its original position after stroking.

Frictional diaphragm elements held in the main housing rub on the shaft to dissipate energy. A Belleville spring helps to regulate the damping force. These components function together as follows: When the shaft is at rest, the frictional diaphragm elements remain tilted as shown in the lower left part of the figure. When the shaft strokes, these elements are forced to become more nearly perpendicular to the shaft, thereby squeezing the shaft and exerting the frictional damping force. As these elements are deflected from the static tilted configuration, they come into contact with the Belleville spring. As the frictional force continues to grow, the Belleville spring resists the further deflection of these elements, thereby helping to limit the squeezing and frictional forces. If these elements become deflected beyond perpendicularity toward a tilt opposite that of the static condition, then further tilting results in a decrease of frictional force. Thus, the shock absorber regulates itself, regardless of the coefficient of friction.

Each frictional diaphragm element contains three tabs that ride on the shaft. The tabs are joined by tension beams. The inner diameter of each such element is made slightly smaller than the outer diameter of the shaft, so that they tend to remain tilted at rest and to squeeze the shaft increasingly as they are forced toward perpendicularity to the shaft. The tension beams accommodate the displacement of the tabs during stroking.

This work was done by Clarence J. Wesselski of Lockheed Engineering & Sciences Co. for **Johnson Space Center.** *Further information is contained in a TSP [see page 1].*

This invention is owned by NASA, and a patent application has been filed. Inquiries concerning nonexclusive or exclusive license for its commercial development should be addressed to the Patent Counsel, Johnson Space Center [see page 1]. Refer to MSC-22111.

Portable Device Measures Perpendicularity of Threaded Hole

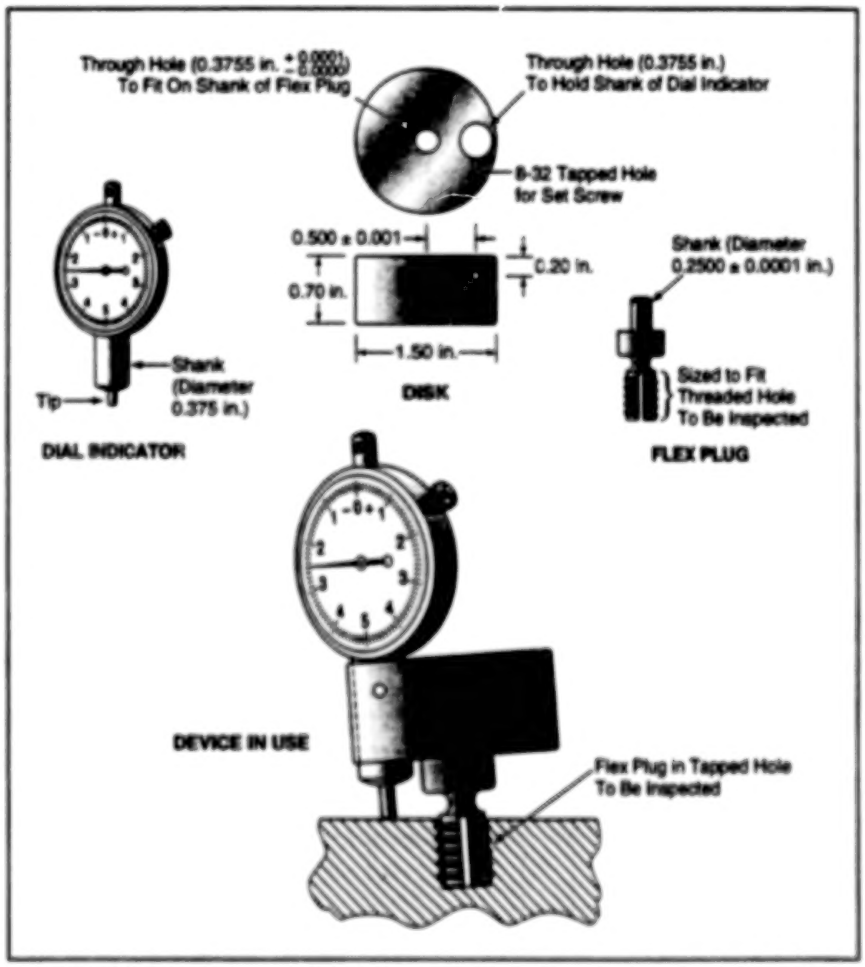
Measurements can be made easily in factory, shop, or field.

Lewis Research Center, Cleveland, Ohio

A simple portable device gives quantitative information on the amount by which the axis of a threaded hole in a workpiece deviates from perpendicularity to the adjacent exterior surface of the workpiece. The device can be used in place of more cumbersome inspection equipment like surface plates, optical comparators, and coordinate-measuring machines, all of which require elaborate setup and are unsuited to use in the field. Inasmuch as neither elaborate additional equipment nor elaborate setup is necessary to use this device, it is well suited for measurements in the field as well as in the shop or laboratory.

The device is an assembly of three relatively inexpensive components (see figure):

- A commercial dial-indicator linear-travel gauge that has a shank of 0.375-in. (9.525-mm) diameter, a total travel of about 1.00 in. (25.4 mm), and scale increments of 0.0005 in. (0.0127 mm);
- A commercial centerline flex plug, chosen to match the size and thread of the hole to be inspected; and
- A disk made of bearing bronze, custom-machined with a central axial hole that mates with the plug, an outer axial hole that fits the shank of the dial indicator, and a hole tapped for a set screw that holds the dial indicator in place.



A Standard Dial Indicator and flex plug are combined with a simple custom-machined disk to make a simple, easy-to-use device for measuring the obliquity of a threaded hole.

Use of the device begins with screwing the flex plug into the threaded hole to be inspected. Next, the disk is placed on the flex plug so that its central axial hole engages the shank of the flex plug. The disk is thereby centered on, and oriented

perpendicular to, the threaded hole to be inspected. The dial indicator is inserted in the 0.3755-in. (9.5377-mm) outer axial hole in the disk so that its tip makes contact with the workpiece and indicates displacement of 0.030 in. (0.762 mm). The set screw is lightly tightened to hold the shank of the dial indicator in place, and the dial is set to zero.

The disk is then turned, so that the contact point at the tip of the dial indicator traces out a circle around the hole to be inspected. During this procedure the dial indicator is observed for any deflection from the zero point position. Any deflection in the dial indicator from the zero point gives the amount of deviation from perpendicular in units of 1.000 in. (25.4 mm). In order to calculate the amount of deviation for a specific depth, the formula is as follows: If the total indicator reading is 0.0045 in. (0.1143 mm), and the feature tolerance is 0.003 in. (0.076 mm) at 0.375 in. (9.525 mm) of depth, the threaded hole is out of perpendicular 0.0016 in. (0.0406 mm) in 3/8 of an inch (9.525 mm). The calculation would be 0.0045 (total indicator reading) × 0.375 (length of feature) = 0.0016875 (deviation from perpendicular).

This work was done by August R. Scarpelli and Daniel W. Buttler of **Lewis Research Center**. *Further information is contained in a TSP [see page 1].*
LEW-15444

Zip Boom

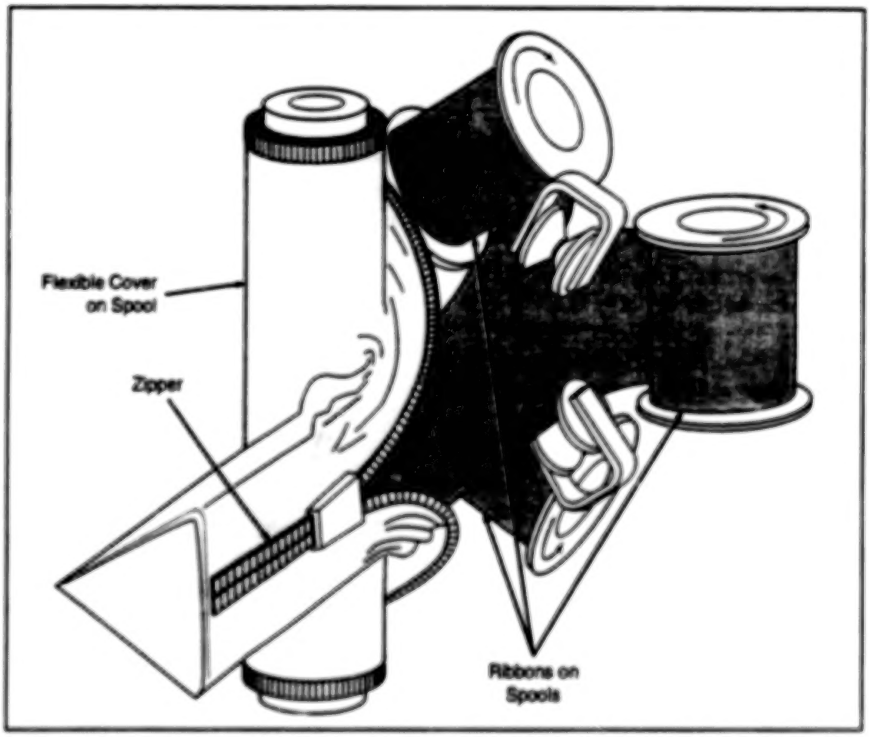
Lightweight deployable structural elements are combined in a stiff geometry.

Lyndon B. Johnson Space Center, Houston, Texas

The zip boom is a lightweight, stiff structural member that can be extended to a great length or retracted into a compact package. It includes three spools of spring-steel ribbon (or other springy ribbon material) arranged so that the ribbons join in a beam of triangular cross section as they unfurl from the rotating spools (see figure). A zippered case extends with the beam, along with a slider that continuously closes the zipper to keep the three extended ribbons wrapped. The tightly fitting case ensures that the edges of the three ribbons always abut each other, without overlapping or slipping. The ribbons thus act as a unit with a triangular cross section that ensures great stiffness.

Each ribbon has to flex around only one axis — that of its spool. Therefore, the ribbon can be made thick, further increasing the stiffness of the boom.

This work was done by Scott Swan of **Johnson Space Center** *and Richard Smallcombe of ILC Space Systems. Further information is contained in a TSP [see page 1].*
MSC-22262



Three Ribbons of Spring Material are joined at their edges to form a triangular boom. A flexible case zips around the extending boom to keep it triangular.

Books and Reports

Designing an Adaptor To Connect Rocket Stages

A lightweight truss structure would consist mostly of round tubes.

A report describes design of a lightweight truss structure to serve as an adaptor to connect two rocket stages, subject to a stringent requirement to minimize cost. The larger stage is a Centaur rocket, on which are provided eight attachment points arranged in a circle 111.77 in. (283.90 cm) in diameter. The smaller stage is a Thiokol Star 48b rocket, which includes a round attachment flange, 45 in. (114.3 cm) in diameter. The conventional adaptor structure for this purpose would have been a thin, stiffened conical shell. By use of finite-element analysis, the design of the truss structure was optimized with respect to the number and geometry of struts and the overall weight of the structure. For mating with the attachment flange, the design provides for grooved slots at the upper ends of the struts. The weight of the truss structure would be less than that of the corresponding stiffened conical shell.

This work was done by Lisa L. Genn and Michael T. Hicks of Harvey Mudd College for **NASA's Jet Propulsion Laboratory**. *To obtain a copy of the report, "Pluto Fast Flyby Probe: Interstage Adaptor Designs for Thiokol 48b and Centaur and for Thiokol 48b and Thiokol 27 Stages," see TSP's [page 1].*
NPO-19468

Vacuum Door for Testing a Spacecraft X-Ray Camera

A report describes a vacuum door to provide environmental protection of an x-ray camera aboard a spacecraft, and to provide access to the camera for prelaunch testing. The door seals one side of a chamber and encloses a vacuous or dry gas environment that is needed to protect the camera. To reduce weight and cost and possibly increase reliability, a paraffin actuator is used instead of a motor to open the door. The mechanism can be activated automatically.

This work was done by Donald H. McQueen, Jr., of **Marshall Space Flight Center**. *Further information is contained in a TSP [see page 1].*
MFS-28963

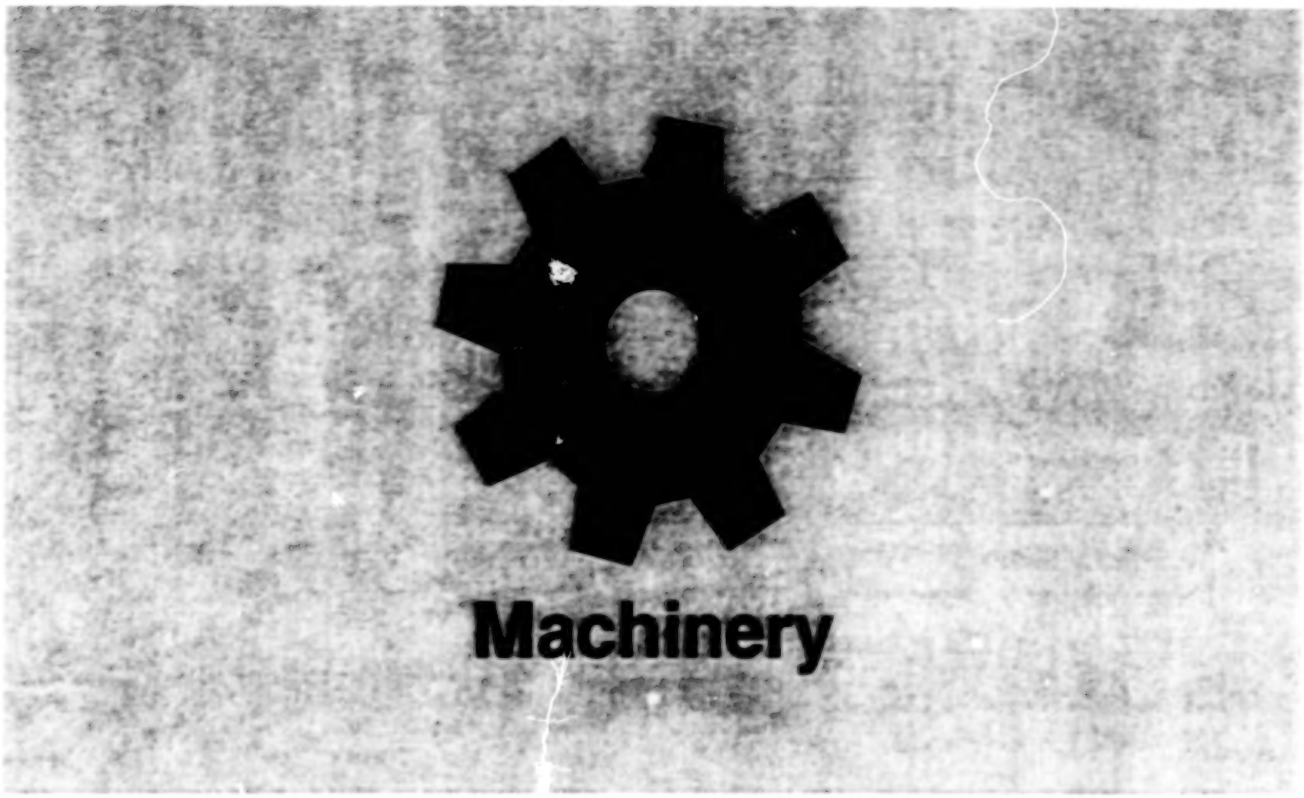
Radiation Propulsion for Maintaining Orbits

Small heaters would compensate for drag on satellites.

A brief report proposes radiative propulsion systems for maintaining precise orbits of spacecraft. Radiation from electrical heaters would be directed outward by paraboloidal reflectors to produce small forces to oppose the uncontrolled drag and solar-radiative forces that perturb orbits. This would minimize or eliminate the need to fire rocket thrusters to correct orbits. For example, infrared radiated power of only 150 W would compensate for a typical drag force of 0.5 μN. The power would come from surplus electrical energy generated by a solar photovoltaic array or stored in a battery.

This work was done by Robert Richter of Caltech for **NASA's Jet Propulsion Laboratory**. *To obtain a copy of the report, "Radiative Propulsion System for Satellites," see TSP's [page 1].*
NPO-19276

BLANK PAGE



Machinery

Hardware, Techniques, and Processes

55 Direct-Circulation Stirling-Cycle Refrigerator
56 Stepping-Motor Drive Suppresses Torsional Oscillation
57 Automated Positioner for a Specimen in a Vacuum Chamber
58 Brake Stops Both Rotation and Translation

Books and Reports

58 Human Interfaces in Teleoperations and Virtual Environments
58 Historical Survey of Flight-Testing Accidents

BLANK PAGE

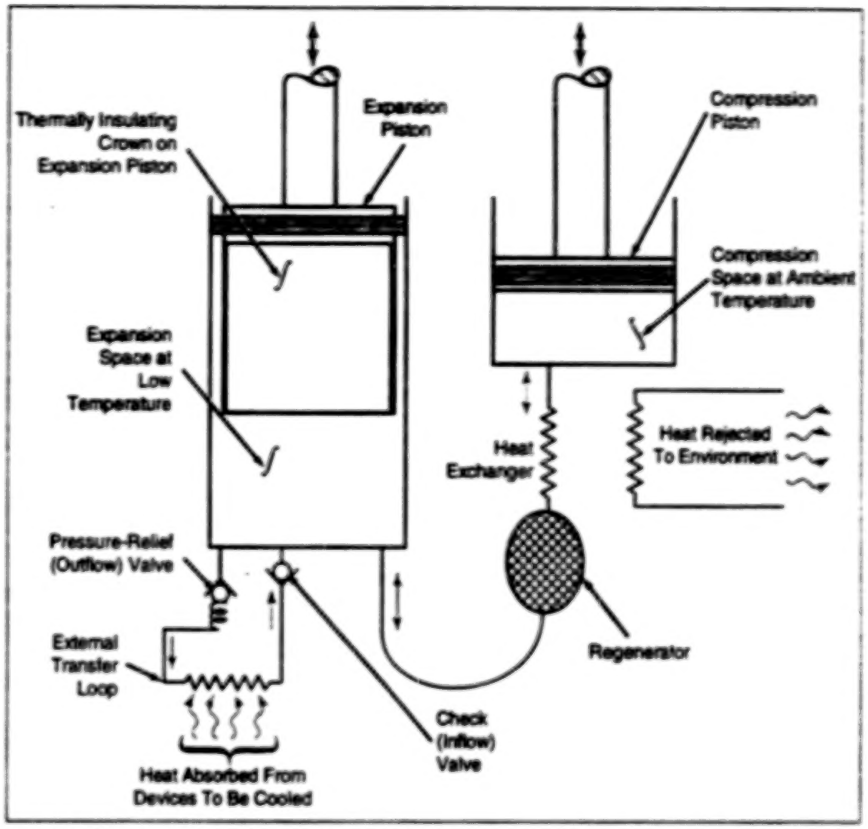
Direct-Circulation Stirling-Cycle Refrigerator

Advantages include less complexity, smaller size, lighter weight, and lower power consumption.

Marshall Space Flight Center, Alabama

In a proposed cryogenic system, the cold working fluid (helium) would be circulated directly from Stirling-cycle refrigerator machinery through a loop of tubing to provide 15 W of cooling power at a temperature of 80 K to scientific instruments or other devices located at some distance from the machinery. (Separation of the cooled devices from the machinery may be dictated by engineering requirements including, notably, the need to isolate the cooled devices from the vibrations of the machinery.) Heretofore, the separation of cooled devices from the refrigerator would have been accomplished by use of (1) an intermediate heat exchanger between the refrigerator and an external transfer loop plus (2) an additional pump to circulate cryogenic fluid within the external cooling transfer loop. In comparison with older Stirling-cycle refrigerators of equal cooling power, the proposed refrigerator would have to be designed oversized with respect to volumetric displacement to provide for direct external circulation of the working fluid. However, the increase in size should be more than offset by the reductions in the number of components, size, weight, and power consumption that would be afforded by elimination of the intermediate heat exchanger and external coolant pump.

In the ideal Stirling refrigeration cycle, the working fluid takes on heat at constant volume as it passes through a regenerator from a cold expansion space to a warm compression space (at ambient temperature in this case). The regenerator acts as a thermodynamic analog of a sponge, cyclically absorbing heat from and releasing heat back to the working fluid. Heat is rejected from the system through a heat exchanger during an isothermal compression in the compression space. The working fluid then passes back through the regenerator in a constant-volume regenerative cooling process. Heat is stored in the regenerator for transport out in the next cycle. Finally, refrigeration occurs in an isothermal expansion process in the expansion space, where heat is absorbed by the working fluid. The ideal Stirling cycle has the same theoretical thermodynamic performance as does the Carnot cycle. Both ideal cycles are impossible to achieve in practice. Practical Stirling refrigerators can achieve up to 40 percent of the ideal Carnot performance.



The Working Fluid Would Be Circulated Directly through the external transfer loop by exploiting the pressure cycle in the Stirling working space (the expansion and compression spaces and the plumbing between them).

In the proposed system (see figure), an expansion piston and a compression piston would reciprocate in parallel cylinders, synchronously but with the expansion piston about 90° ahead in phase. The working fluid would therefore shuttle through the regenerator between the compression and expansion spaces, and the total volume available to the working fluid would also vary cyclically. Compression would occur when the working fluid was mostly in the compression space. Similarly, expansion would occur when the working fluid was mostly in the expansion space.

A portion of the Stirling pressure cycle would be used to pump the cold working fluid between the expansion space and the external transfer loop: this would be a new operating mode for a Stirling machine. Ingress and egress of the working fluid would be accomplished by spring-loaded, pressure-regulating valves that would operate automatically as the pressure in the working fluid varied cyclically; the effect on the pressure cycle would be to clip the pressure peak somewhat. At the beginning of a cycle, both valves would be closed, and pressure would be increasing. After the pressure reached a preset relief setting, a pressure-actuated outflow valve would open, allowing working fluid to flow into the external loop, which would be maintained at the minimum cycle pressure. The outflow would continue until the volume in the Stirling working space reached its minimum, and then both valves would close.

As the cycle continued, the volume in the Stirling working space would increase, causing refrigeration by expansion. The pressure in the Stirling working space would decrease during this expansion until it became equal to the pressure in the external coolant loop. Further increase in volume would

cause working fluid in the external transfer loop to flow through a check valve back into the expansion space, carrying with it the heat that it had absorbed from the devices to be cooled.

This work was done by Woody Ellison and Randall Kohuth, Sr., of General Pneumatics Corp. for **Marshall Space Flight Center.** *Further information is contained in a TSP [see page 1].*

Inquiries concerning rights for the commercial use of this invention should be addressed to the Patent Counsel, Marshall Space Flight Center [see page 1]. Refer to MFS-26244.

Stepping-Motor Drive Suppresses Torsional Oscillation

Steps are equal and paired at half the period of torsional oscillation.

Goddard Space Flight Center, Greenbelt, Maryland

Figure 1 illustrates a stepping-motor drive that rotates an antenna, solar photovoltaic array, or similar flexible structure to a commanded angle. The amplitude and timing of the rotational steps of the stepping motor can be controlled in such a way as to suppress the torsional oscillations excited in the structure by these steps.

The top part of Figure 2 shows what happens when the rotational step excitations are applied in a conventional manner; namely, as single steps at intervals of T. (T is a time chosen consistent with the commanded rate of rotation and is typically much greater than the period of torsional oscillation.) In the absence of damping, each step excitation contributes to the amplitude of torsional oscillation; this effect can be especially pronounced if T is an integral multiple of the oscillation period.

The excitation in this stepping-motor drive differs from the conventional excitation in that each step is divided into two equal smaller steps separated by a small interval, τ. This interval is chosen to equal half the period of torsional oscillation, so that the second step excitation is equal in amplitude but opposite in phase to the first step excitation. Thus, although the first step unavoidably excites a torsional oscillation, the second step deexcites the oscillation at the end of its first half cycle (see Figure 2). The interval τ can be preset, or else the command unit in the stepping-motor drive can be designed to measure residual torsional oscillations repeatedly to update τ when the torsional oscillatory characteristics are subject to change.

This work was done by Mahabaleshwar K. P. Bhat of Ford Aerospace and Communications Corp. for **Goddard Space Flight Center.** *Further information is contained in a TSP [see page 1].*

GSC-13100

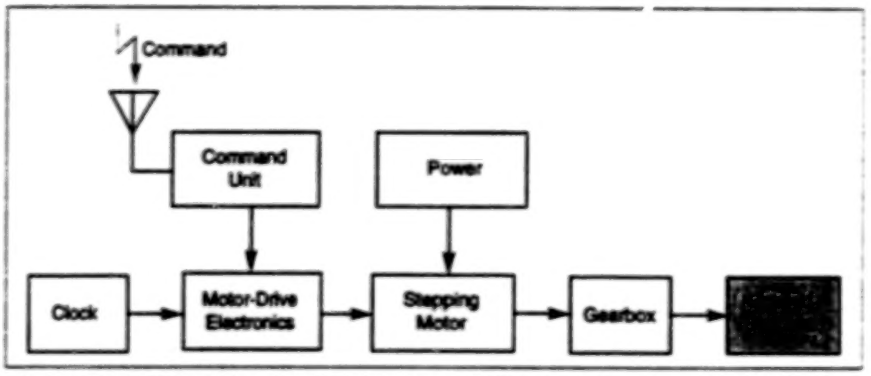


Figure 1. This Stepping-Motor Drive implements a paired-step excitation scheme in which the steps in each pair apply equal rotational excitations at opposite phases of the torsional oscillation.

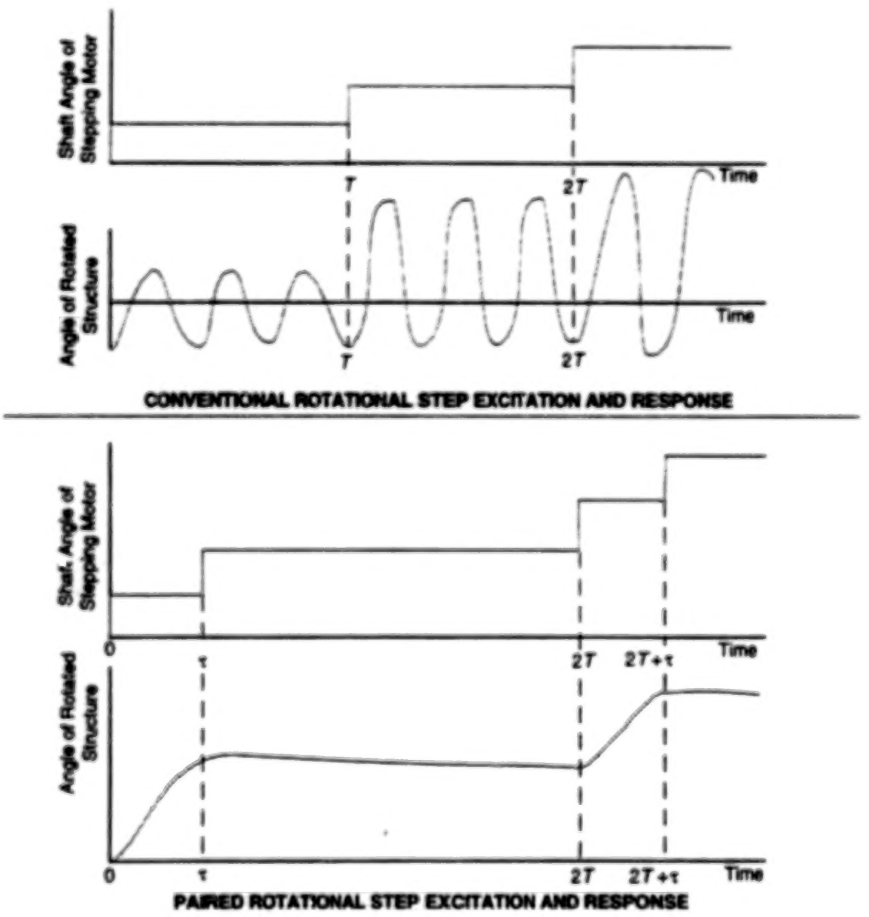
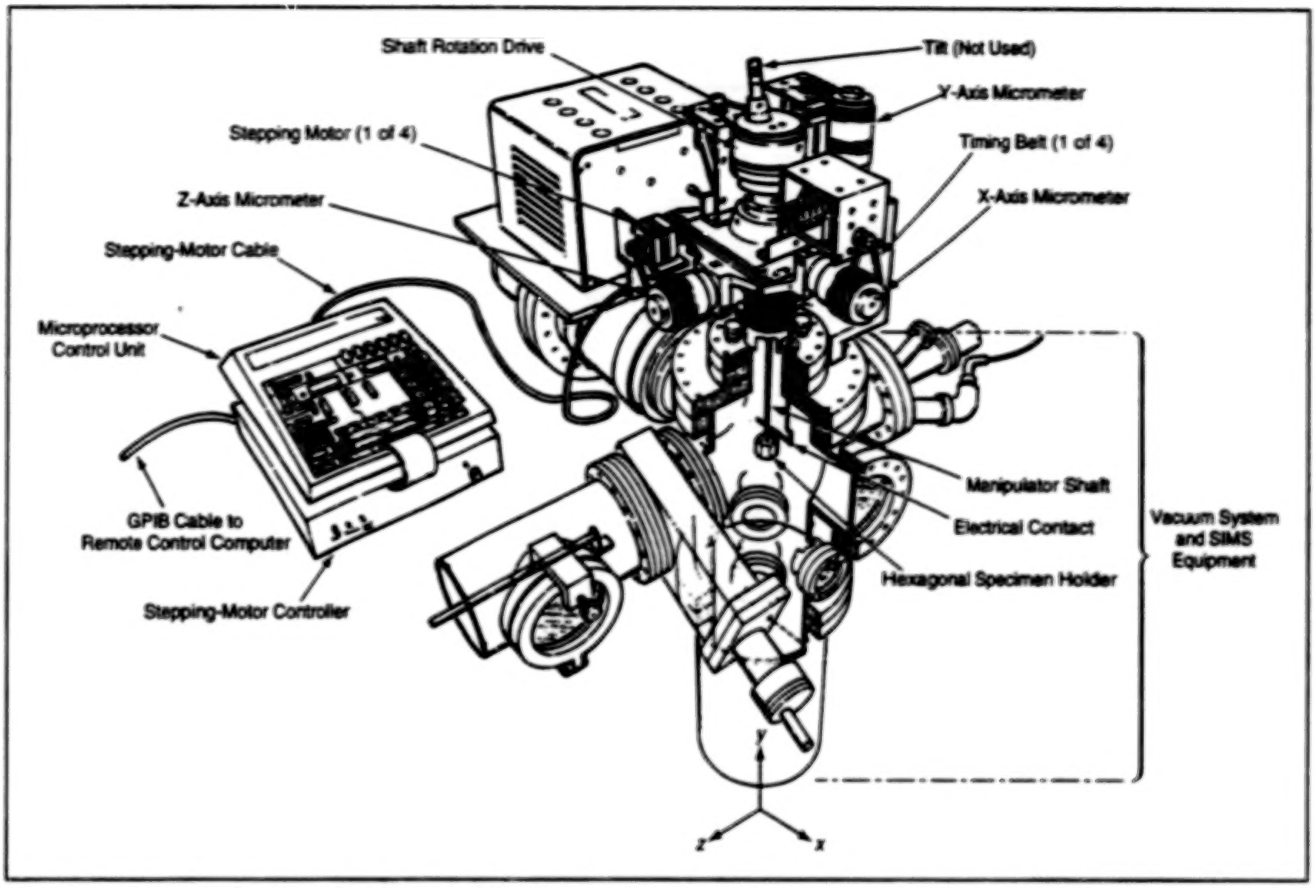


Figure 2. Conventional and Paired-Step Excitations produce different responses.

Automated Positioner for a Specimen in a Vacuum Chamber

This apparatus is made from relatively inexpensive parts.

Lewis Research Center, Cleveland, Ohio



The **Vacuum-Chamber Specimen Positioner** contains four stepping motors — one for a rotational degree of freedom and one for each of three translational degrees of freedom.

A custom-built apparatus positions a specimen in a vacuum system in three translational and one rotational degree of freedom. The apparatus operates under manual control, local microprocessor control, or remote computer control via a general-purpose interface bus (GPIB), the specific control option being selectable by the technician. It is used, for example, to position and orient a specimen for secondary-ion mass spectroscopy (SIMS). The cost of parts to construct the system (excluding the computer and a specimen manipulator) was $800 in 1991 — less than one tenth the cost of a general-purpose commercial vacuum manipulator system at that time.

The apparatus includes a separate stepping motor to generate movement in each of the four degrees of freedom. The stepping motor for each translational degree of freedom drives a micrometer stage. The stepping motors are compact biphase motors with 100 steps per revolution. Their positional and step-to-step accuracy is +5 percent. Timing belts and matching pulleys increase both the precision and the torque available to drive the micrometer stages for the translational degrees of freedom. A pulley drive with a ratio of 3.6:1 is used for the rotational degree of freedom. The net resolutions are 1 μm per step in translation and 1° per step in rotation. For simplicity, no switches, optical encoders, or similar hardware for absolute positioning is included. Therefore, it is necessary to give the computer program the initial coordinate settings at start-up.

The microprocessor control unit is based on the 8-bit Motorola MC6802 microprocessor. It includes a 17-key keyboard and a 6-digit, seven-segment light-emitting-diode (LED) display for standard input and output operations. It contains 2.5 Kbytes of random-access and read-only memory.

The software for both the local and remote modes of computer control is about 2 Kbytes long and resides in the read-only memory. When the technician initiates operation by pressing a "run" button switch on a controller box, the software initializes the settings of a data-communication interface circuit, displays the GPIB address of the microprocessor unit, assigns specific control functions to the keys on the keyboard, and displays the present value of the angular coordinate. The technician can then provide input from the keyboard, or the remote control computer can supply input in the form of previously defined bus commands.

The repeatability of positioning achievable by the apparatus was measured in an experiment in which a silicon specimen was bombarded with a 0.250-μm-wide beam of oxygen ions in one spot, then the apparatus was used to move the specimen in a pattern, stopping along the way to bombard the specimen similarly in other spots. The pattern was chosen in such a way as to produce, then remove backlash in two of the three degrees of translational freedom. At the end, the specimen was returned to its

original nominal position and bombarded again. The second bombardment crater at the original position was collocated with the first; the only difference was that the crater became larger in the second bombardment.

This work was done by Sheila G. Bailey of **Lewis Research Center** *and Carlos Vargas-Aburto and Dale R. Liff of Kent State University. Further information is contained in a TSP [see page 1].*
LEW-15904

Brake Stops Both Rotation and Translation

A single actuator energizes both braking actions.

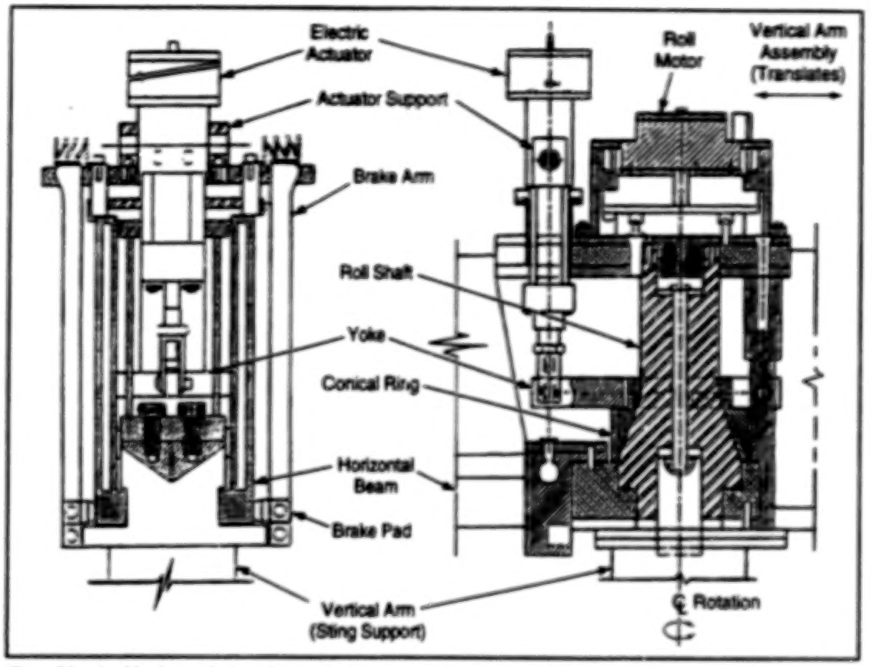
Langley Research Center, Hampton, Virginia

A combination of braking and positioning mechanisms allows both rotation and translation before the brake is engaged. These mechanisms are designed for use in positioning a model airplane in a wind tunnel. A modified version could be used to position a camera on a tripod.

The brake is fast and convenient to use; it contains a single actuator that energizes the braking actions against both rotation and translation. The braking actuator is electric, but a pneumatic actuator could be used instead. The brake is compact and lightweight, applies locking force close to the load, and presents minimal cross section to airflow.

The combination of braking and positioning mechanisms includes a vertical arm that is held up by a horizontal arm. The vertical arm holds a rod (called a "sting" in the wind-tunnel industry) on which the model is mounted. When the brake is not engaged, the vertical arm can translate along the horizontal arm and can rotate. An electric motor that is part of the positioning mechanism rotates the vertical arm to position the model as required.

When the required position has been reached, the brake is engaged: the brake actuator pushes downward on a yoke, forcing a conical ring onto a tapered portion of a roll shaft, thereby imposing friction against rotation. The reaction force from the engagement of the ring and roll shaft pushes the actuator upward, pressing serrated brake pads into contact with serrations on the horizontal arm, thereby locking against translation. Until deliberately disengaged, the brake remains engaged, even during a power failure.



The Single Motion of the Actuator presses the conical ring against the conically tapered section of the roll shaft. This action simultaneously stops both translation of the mechanism along the horizontal arm and rotation of the vertical arm.

This work was done by Johnny W. Allred and Vincent J. Fleck, Jr., of **Langley Research Center**. *Further information is contained in a TSP [see page 1].*

This invention is owned by NASA, and a patent application has been filed. Inquiries concerning nonexclusive or exclusive license for its commercial development should be addressed to the Patent Counsel, Langley Research Center [see page 1]. Refer to LAR-14738.

Books and Reports

Human Interfaces in Teleoperations and Virtual Environments

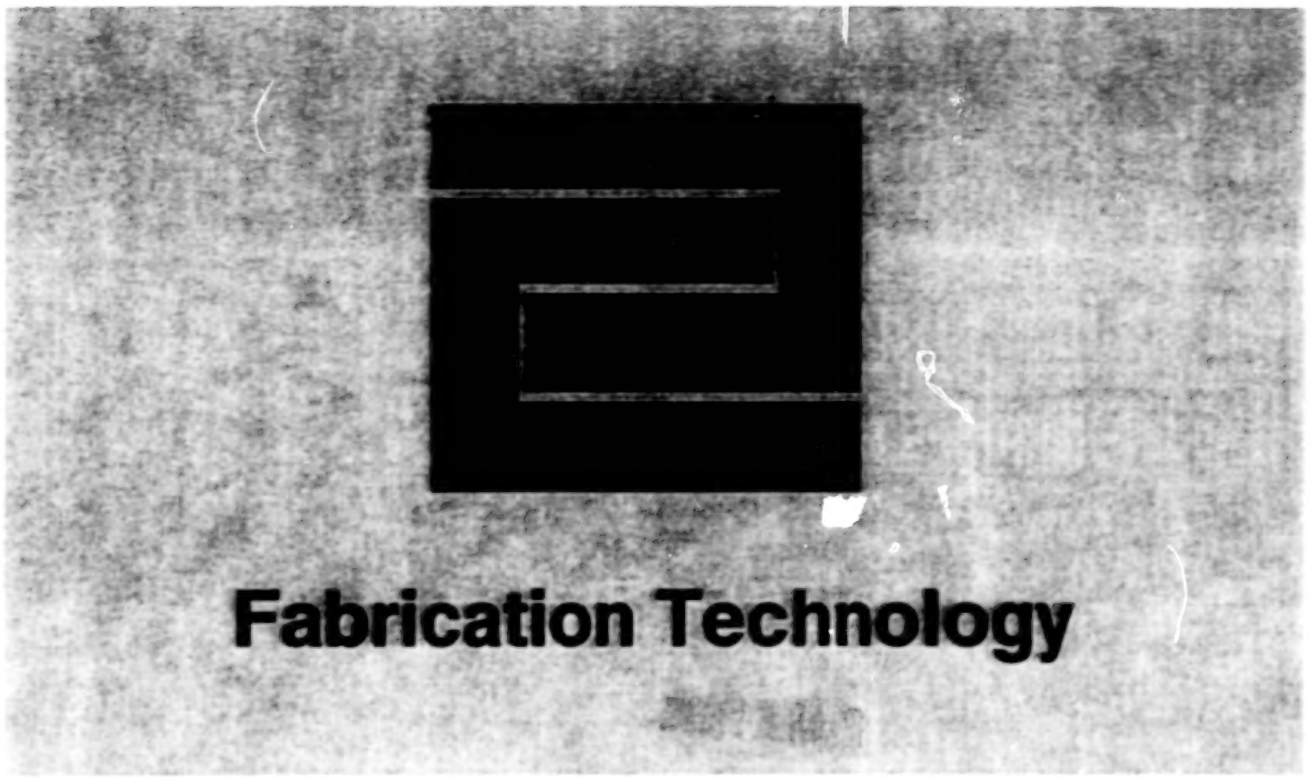
A conference report contains a compilation of papers relating to interactions between humans and machines from the perspectives of (1) telepresence and sensorimotor adaptation, (2) measurement and evaluation of performance, and (3) design principles and predictive models. Topics discussed include neural networks, sensory technology, display, and feedback controls. The report covers the state of the art of remote sensing and control by humans for space or other operations.

This work was done by Nathaniel I. Durlach, Thomas B. Sheridan and Stephen R. Ellis of **Ames Research Center**. *To obtain a copy of the report, "Human Machine Interfaces for Teleoperators and Virtual Environments," see TSP's [page 1].*
ARC-13302

Historical Survey of Flight-Testing Accidents

A report presents a study of flight-testing accidents, with emphasis on limitations imposed by human factors. The study covers the history of flight testing from early lighter-than-air craft (including balloons) to vertical take-off airplanes to the space shuttle. The results show that new aircraft and new pilots are not immune to old problems. Inadequacy of pilot skill and training, unintentional errors, and willingness to take unnecessary risks were found to be frequent causes of accidents. One of the lessons learned in the study is that plans designed to cope with otherwise unexpected events can help reduce accidents.

This work was done by Seth B. Anderson of **Ames Research Center**. *To obtain a copy of the report, "Lessons Learned From An Historical Look At Flight Testing," see TSP's [page 1].*
ARC-13320



Fabrication Technology

Hardware, Techniques, and Processes

61 Embedding Optical Fibers in Cast Metal Parts

61 Improved Method of Bending Concentric Pipes

Books and Reports

62 Composite-Material Propfan Blades for a Wind-Tunnel Model

BLANK PAGE

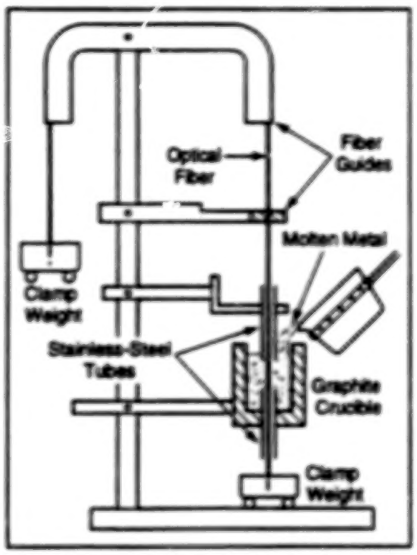
Embedding Optical Fibers in Cast Metal Parts

Use of metal strain reliefs eliminates breakage of fibers during casting process.

Lewis Research Center, Cleveland, Ohio

A technique for embedding fused silica optical fibers in cast metal parts has been devised. An optical fiber could be embedded in a flange, fitting, or wall of a vacuum or pressure chamber, for example, to provide a hermetically sealed feedthrough for optical transmission of measurement or control signals. For another example, an optical-fiber temperature sensor could be embedded in a metal structural component to measure strain or temperature inside the component.

In previous attempts at embedding optical fibers in cast metal parts, the fibers broke at and near the surfaces of the parts, most likely as a result of stresses introduced into the fibers by contraction of the metal during cooling to room temperature after casting. The present technique for embedding the fibers prevents breakage by providing for relief of the cooldown stresses.



The Optical Fiber Is Embedded by Casting the metal part around it. Stainless-steel tubes around the fiber are also embedded to relieve stresses.

As shown in the figure, a fiber to be embedded in a cast metal part is first slipped into two narrow tubes made of a metal (typically of stainless steel) that has a melting temperature greater than that of the metal to be cast. The tubes are positioned so that they will stick partly in and partly out of the cast object. The tubes relieve the stresses on the parts of the fiber near the surfaces.

This work was done by William N. Gibler, Robert A. Atkins, Chung E. Lee, and Henry F. Taylor of Texas A & M University for **Lewis Research Center**. *Further information is contained in a TSP [see page 1].*

LEW-15233

Improved Method of Bending Concentric Pipes

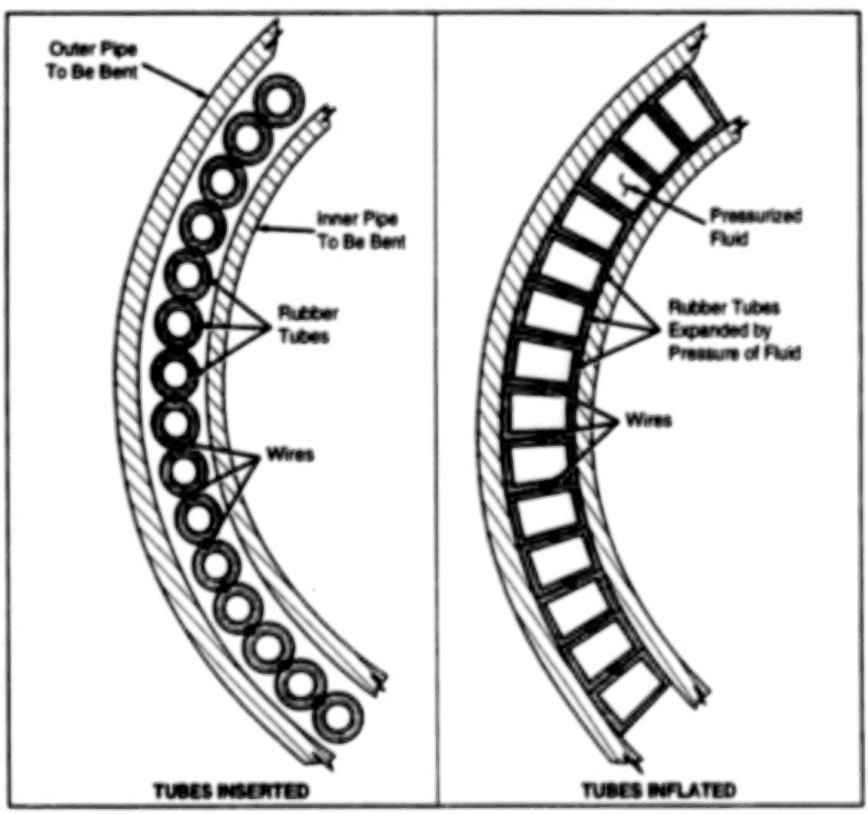
Bending could be done faster and more cleanly, and it could be largely automated.

NASA's Jet Propulsion Laboratory, Pasadena, California

A proposed method for bending two concentric pipes simultaneously while maintaining the void between them would replace the present tedious, messy, and labor-intensive method. The proposed method would enable bending to be done faster and more cleanly, and would be amenable to automation of a significant portion of the bending process on computer numerically controlled (CNC) tube-bending machinery.

In the present method, one fills the interpipe gap with fine metal shot, seals the gap at the ends of the pipes, bends the pipes in a bending machine, unseals the pipes, and cleans out the shot. All of these steps are performed manually and/or by machinery under manual control.

In the proposed method, a CNC machine would first insert, between the concentric pipes to be bent, an array of rubber tubes stiffened by axial wires. A relatively incompressible liquid would be pumped into the rubber tubes and pressurized so that the rubber tubes would fill the gap completely (see figure). The array would be held together at one end by a solid rubber block. At the other end, each rubber tube would be sealed,



An Array of Rubber Tubes would be inserted in the gap between concentric pipes. The tubes would then be inflated with a relatively incompressible liquid to fill the gap.

after pressurization, with a clamping plunger.

The CNC machine would then bend the concentric pipes to the desired curvature. During bending, the inflated tubes would maintain the gap between the pipes, preventing buckling. After bending, the CNC machine would release the clamping plunger to release the pressurized liquid and would remove the tubes from the bent pipes. As the tubes emerged from the bent pipes, the wire stiffeners would restore the rubber tubes to straightness. There would be no shot or other solid residue to clean up.

This work was done by James E. Schroeder of Caltech for **NASA's Jet Propulsion Laboratory**. *Further information is contained in a TSP [see page 1].*

In accordance with Public Law 96-517, the contractor has elected to retain title to this invention. Inquiries concerning rights for its commercial use should be addressed to

William T. Callaghan, Manager
Technology Commercialization
JPL-301-350
4800 Oak Grove Drive
Pasadena, CA 91109

Refer to NPO-19089, volume and number of this NASA Tech Briefs *issue, and the page number.*

Books and Reports

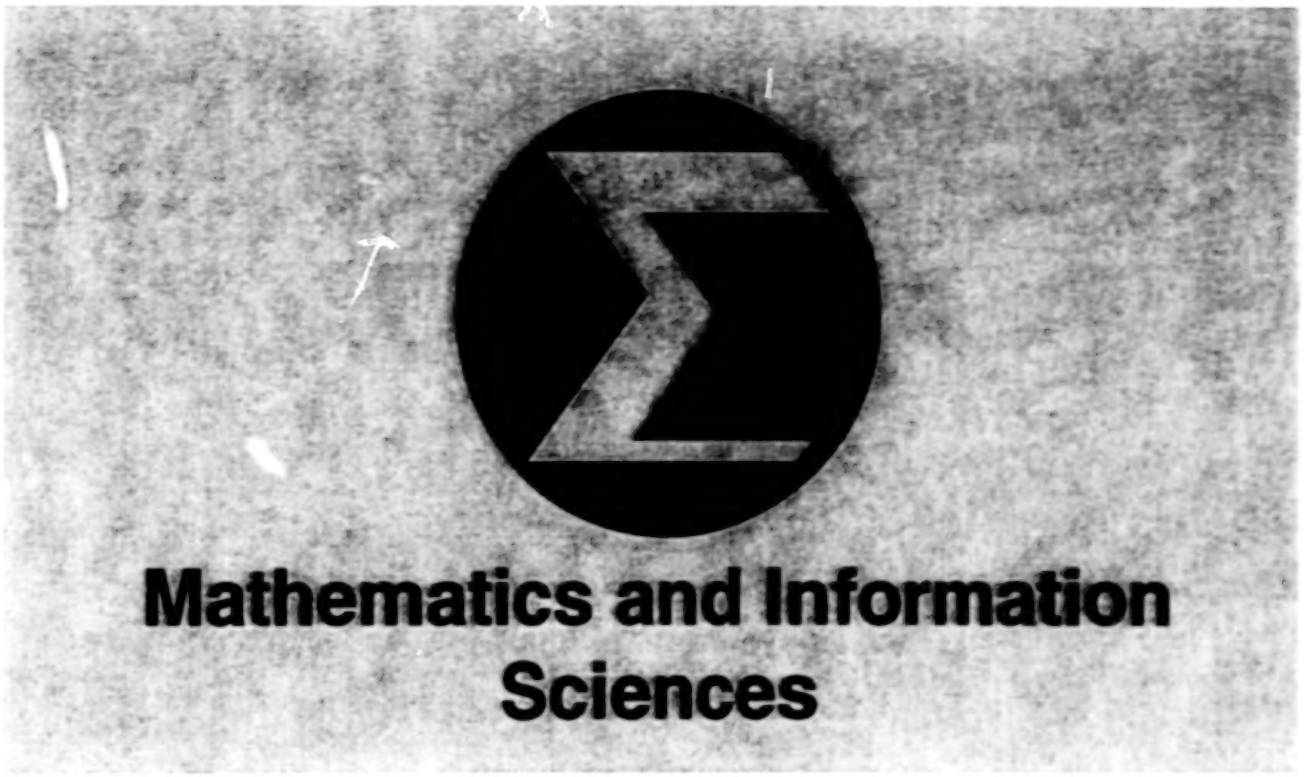
Composite-Material Propfan Blades for a Wind-Tunnel Model

Design and fabrication are described.

A report discusses the design and the sequence of operations performed in fabricating a set of graphite-fiber/epoxy-matrix composite propfan blades. The blades were used in wind-tunnel experiments on a 0.55-scale model of a cruise missile, as part of an investigation of the feasibility of advanced unducted-propfan propulsion systems for cruise missiles. The report describes the major phases of fabrication of the blades, including the machining of metal master blades, fabrication of molds from the master blades, cutting of graphite-fiber/epoxy prepreg sheets to form plies, stacking of plies to obtain preforms, assembly of pressure- and suction-side preforms into unitary blade preforms, curing the preforms in molds, final light finishing, and inspection. Altogether, 18 blades of each of four designs were fabricated by use of the same techniques.

This work was done by E. Brian Fite of **Lewis Research Center**. *To obtain a copy of the report, "Fabrication of Composite Propfan Blades for a Cruise Missile Wind Tunnel Model," see TSP's [page 1].*

Inquiries concerning rights for the commercial use of this invention should be addressed to the Patent Counsel, Lewis Research Center [see page 1]. Refer to LEW-16088.



Mathematics and Information Sciences

Hardware, Techniques, and Processes

65 Pseudogradient Training for a Class of Neural Networks
66 Extracting Periodic Signals From Irregularly Sampled Data

Books and Reports

66 Linear Prediction of Stationary Sequences of Vectors
67 Telemetry Frame Processor

BLANK PAGE

Pseudogradient Training for a Class of Neural Networks

Step activation functions impart stability.

NASA's Jet Propulsion Laboratory, Pasadena, California

Developmental second-order recurrent neural networks of a special type have been modified to enhance their stability in the face of inputs beyond the range of the inputs on which they are trained. Second-order recurrent neural networks contain product feedback units and can be trained, by use of example inputs and outputs, to act as finite-state automatons. The particular second-order recurrent neural networks in question learn grammars in the sense that they are trained to generate binary responses ("legal" vs. "illegal") to input training sequences of ones and zeros, each sequence being marked "legal" or "illegal" according to the grammar to be learned.

During the training of an unmodified network of this type, one presents the network with randomly chosen training strings of various lengths up to some maximum length, and, for each string, seeks to reduce the error in the response of the network by adjusting the network weights (the strengths of the synaptic connections between neurons) according to a gradient descent of an error measure in weight space. The error measure is defined with respect to the output (activation) of one of the neurons in the network that is designated as an indicator neuron: The correct activation of the indicator neuron is 1 if the input string is legal and 0 if it is illegal. The error measure is proportional to the square of the difference between the actual and correct activations.

As training progresses, the unmodified network attempts to form clusters of points in activation space as its internal representation of states. Once training has been completed, the unmodified network acts like a state machine in that its activation point jumps from one cluster to another when presented with input bits one by one, provided that the string of input bits is no longer than the longest training string. However, when presented with longer input strings, the network behaves unstably in that the activation points move out from the clusters: in essence, the unmodified network "forgets" where the individual states are in activation space.

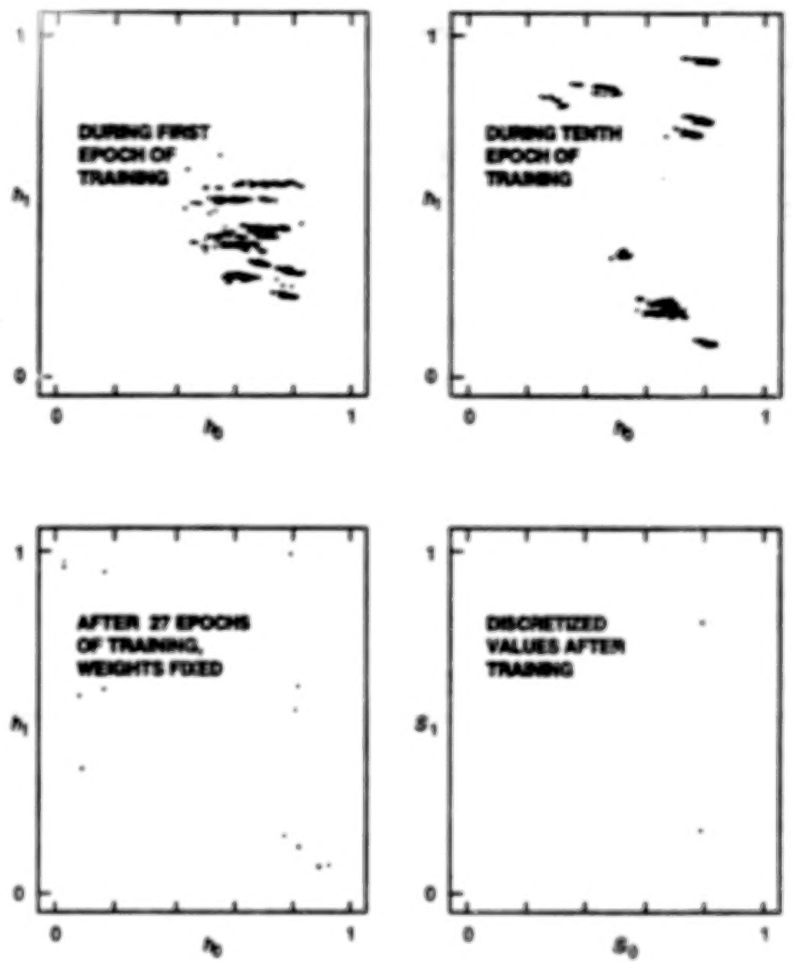
Therefore, two modifications have been made to enable the network to learn stable states; that is, to form clusters such that activation points for long strings also converge to central points within the clusters (see figure). The first modification is replacement of the standard sigmoid activation function

$$f(x) = \frac{1}{1+e^{-x}}$$

with the step function

$$D(x) = \begin{cases} 0.8 \text{ if } x \geq 0 \\ 0.7 \text{ if } x < 0 \end{cases}$$

where x is the sum of weighted excitations applied to the input terminal of a neuron. This modification, by itself, would prevent learning by the gradient-descent method because the nondifferentiability of $D(x)$ would make it impossible to examine the effect of small changes in weights on the error measure.



These Plots Are Activation-Space Records of a four-hidden-unit second-order recurrent neural network. The plots were recorded during and after training the network according to a grammar called "Tomita Grammar #4." The symbols h_0 and h_1 denote the continuous activation values according to the sigmoids; the symbols S_0 and S_1 denote the discretized (step-function) values.

Accordingly, the second modification is the introduction of a pseudogradient method: the sigmoid activation function is used in place of the step function to calculate a gradient (the pseudogradient), which is used only as a guide to locating the steps in activation space and adjusting the weights. The pseudogradient method may also be useful as a basis for training neural networks of other types that involve hard-limiting threshold activation functions.

This work was done by Zheng Zeng, Rodney M. Goodman, and Padhraic J. Smyth of Caltech for **NASA's Jet Propulsion Laboratory**. *Further information is contained in a TSP [see page 1].*

NPO-18956

Extracting Periodic Signals From Irregularly Sampled Data

Successive approximations are formed in Fourier space.

NASA's Jet Propulsion Laboratory, Pasadena, California

An algorithm extracts periodic signals from sparse, irregularly sampled sets of measurement data. The algorithm pertains to data that are processed via fast Fourier transforms (FFTs). The data can represent signal components with initially unknown frequencies that span a large spectral range and can include frequencies that are not integer multiples of the minimum FFT frequency.

The algorithm was developed to satisfy a need, frequently encountered in the observational sciences, to find periodic signal components with unknown frequencies in samples of data acquired at uneven intervals, sometimes with gaps between the intervals. The gaps give rise to spurious signal components in the FFTs at frequencies that correspond to side lobes and intermodulation products of the signals and gaps. Moreover, the data samples include noise components that mask the periodic signals.

The essence of the algorithm is an iterative procedure of successive refinement of a candidate signal, in which one seeks a least-squares best fit between (a) the FFT obtained from the sampled measurement data and (b) the FFT obtained from the candidate signal sampled (by computational simulation) in the same way as that of the actual data. The steps of the algorithm can be summarized as follows:

1. Compute the FFT from the actual noise-corrupted sampled measurement data (hereafter called "the original FFT").
2. Identify candidate highest peaks in the original FFT, and use them as a guide in computing an initial candidate signal.
3. Compute the samples of the candidate signal, then compute the FFT of the candidate signal from these samples.
4. Following a least-squares best-fit procedure, modify the candidate signal so as to minimize a quadratic measure of the difference between its FFT and the original FFT.
5. If further refinement is desired, use the modified candidate signal in steps 3 and 4. Repeat as many times as desired or until all identifiable frequency components and their amplitudes have been incorporated into the candidate signal, meaning that the candidate signal contains all identifiable periodic components of the actual sampled signal.

This work was done by Jaroslava Z. Wilcox of Caltech for **NASA's Jet Propulsion Laboratory**. *No further documentation is available.*
NPO-19546

Books and Reports

Linear Prediction of Stationary Sequences of Vectors

Transformations that yield computationally efficient schemes are proposed.

A report discusses a direct approach to the linear prediction of a stationary sequence of vectors. It derives a set of equations that constitutes a minimal-order linear predictor. Using this approach, it proposes two specific computationally efficient schemes to predict vectors in a sequence.

To state the problem meaningfully, it is necessary to define some terms:
Let the covariance function of a zero-mean, full-rank stationary sequence of vectors $\mathbf{y}_n \in R^m$ be given by

$$R_k = E\left\{\mathbf{y}_n \mathbf{y}_{n-k}^T\right\}$$

where E denotes the expectation operation. Suppose that there exists a positive integer P and a set of scalars $a_1, \ldots, a_{p-1}, a_0 = 1$, such that for any $n \geq P$

$$\sum_{k=0}^{P-1} a_k R_{n-k} = 0$$

When $\mathbf{y}_n$ is generated by a finite-dimensional linear system driven by white noise, this second equation is satisfied. The Hankel covariance matrix is defined by

$$\begin{bmatrix} R_1 R_2 \ldots R_p \\ R_2 R_3 \ldots R_{p+1} \\ \cdot \\ \cdot \\ \cdot \\ R_1 R_{p+1} \ldots R_{2p-1} \end{bmatrix}$$

Given the foregoing specifications, the prediction problem is one of estimating the values of $\mathbf{y}_{n+k}$, given the values of $\mathbf{y}_{n-1}$, when $k = 0, 1, 2, \ldots$.

The approach taken in this study, inspired by Akaike's coordinate-free realization concepts, is based on simple geometric principles. It involves the suggestion of an explicit coordinate-dependent characterization of the class of all minimal-order linear predictors, in terms of linear transformations on the Hankel covariance matrix associated with the sequence. In contrast with previous approaches, it does not give rise to Riccati or Lyapunov equations. The selection of particular transformation matrices defines specific techniques for the construction of predictors.

In the first of two specific constructions, the predictor is essentially defined by maximal sets of linearly independent rows and columns of R. A procedure for the selection of a maximal set of such rows and columns is presented. This procedure can be extended to the construction of a linear predictor or a minimal realization from a sample covariance sequence by use of a recently proposed statistical rank-test method.

The second of two specific constructions involves the specification of some of the intermediate transformation matrices in such a way as to diagonalize the product of these matrices with R. In this construction, the predictor is specified exactly in terms of matrices derived from R and the transformation matrices. While this construction is computationally more effective than the previous one is, it cannot, at present, be extended by statistical inference to the case in which only a sample covariance sequence is given.

This work was done by Yoram Baram of **Ames Research Center**. *To obtain a copy of the report, "Linear Prediction of Stationary Vector Sequences," see TSP's [page 1].*

This invention is owned by NASA, and a patent application has been filed. Inquiries concerning nonexclusive or exclusive license for its commercial development should be addressed to the Patent Counsel, Ames Research Center [see page 1]. Refer to ARC-12352.

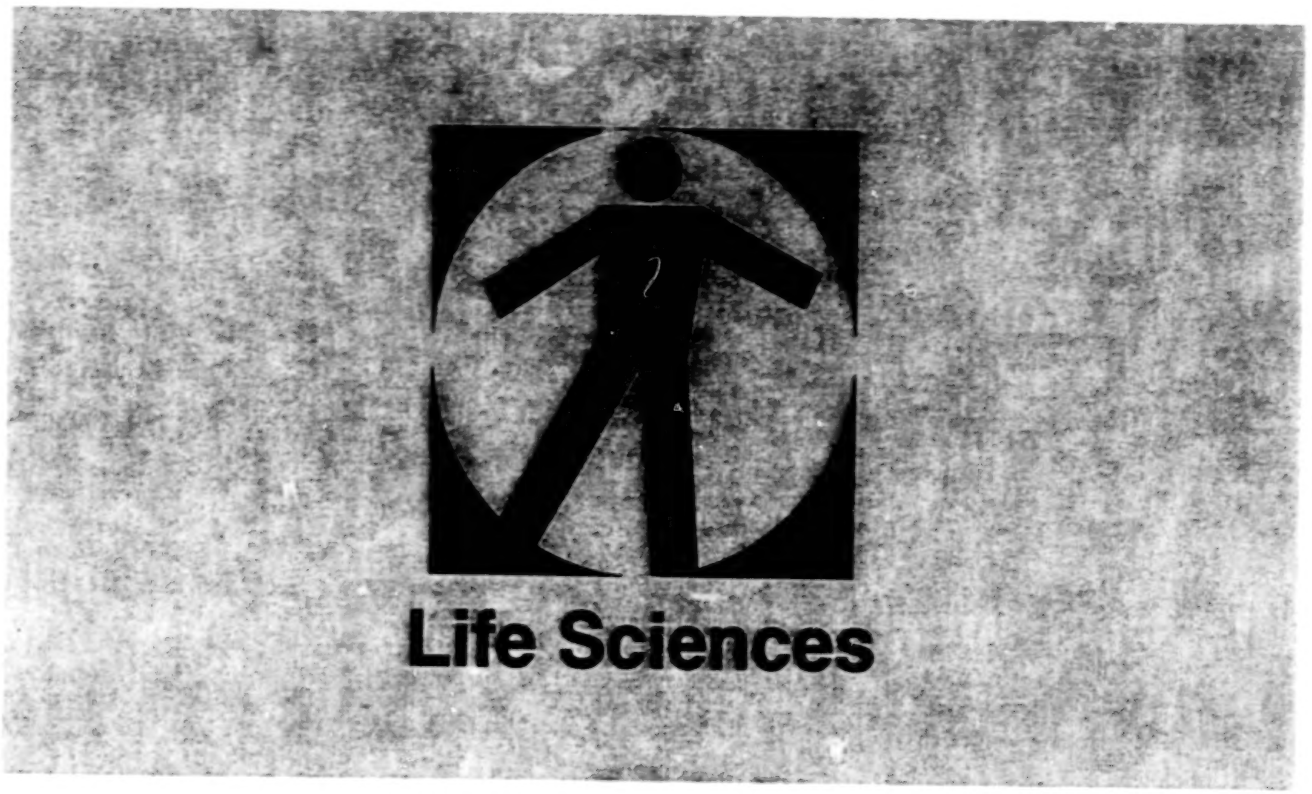
Teiemetry Frame Processor

A report describes a program for creating and editing telemetry frames on a personal computer. The program is menu-driven and can create or edit digital telemetry manually or automatically by occurrence of an event. A stream of telemetric data can be used to test the operation of hardware and software parts of the telemetry-receiving station. The program would be useful in satellite-data-processing facilities like remote-sensing stations.

This work was done by Steve E. Lewis of McDonnell Douglas for **Kennedy Space Center**. *To obtain a copy of the report, "Digital Telemetry (TLM) Frame Building Software (TLMBLDR.EXE)," see TSP's [page 1].*

Inquiries concerning rights for the commercial use of this invention should be addressed to the Patent Counsel, Kennedy Space Center [see page 1]. Refer to KSC-11763.

BLANK PAGE



Hardware, Techniques, and Processes

71 Hip Implant Modified To Increase Probability of Retention
71 Portable Immune-Assessment System

BLANK PAGE

Hip Implant Modified To Increase Probability of Retention

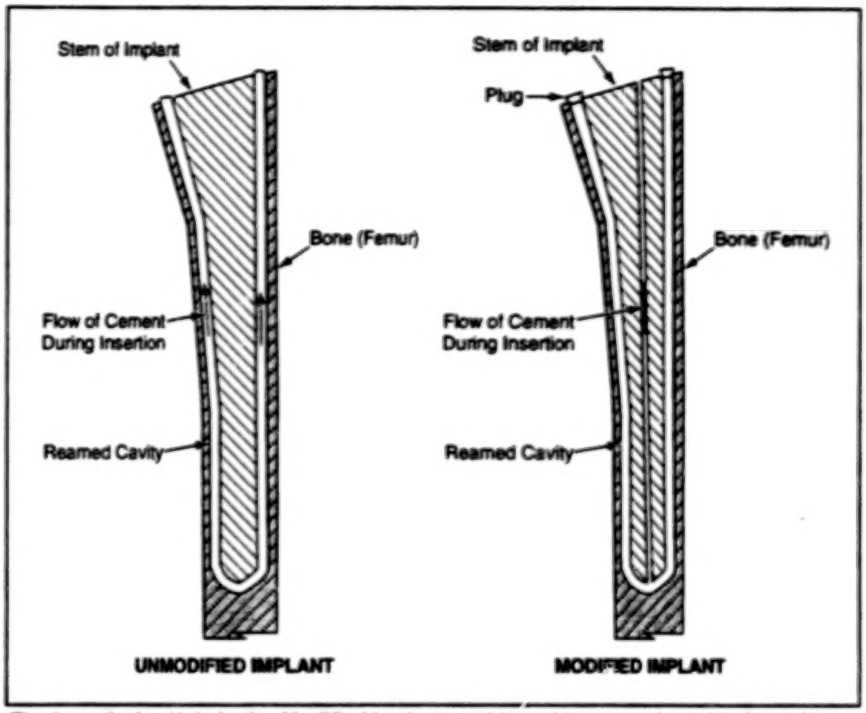
The modification would alter the flow of cement to reduce structural imperfections.

Marshall Space Flight Center, Alabama

A modification in the design of a hip implant has been proposed to increase the likelihood of retention of the implant in the femur after hip-repair surgery. In so doing, the modification would decrease the likelihood of the patient distress and the expense associated with a repetition of surgery after a failed implant procedure. As explained below, the modification is intended to provide a more favorable flow of a cement that is used to bind the implant in the proximal extreme end of the femur, thereby reducing structural flaws that can cause early failure of the implant/femur joint.

An unmodified implant of the type in question includes a solid stem that is inserted into an axial cavity that has been reamed into the proximal end of the femur (see figure). Immediately prior to insertion of the implant, bone cement is placed in the cavity. Then as the stem is inserted, it displaces the adhesive, and the excess adhesive flows to the opening at the top of the bone. According to a numerical simulation, the flow is laminar and characterized by boundary layers, vortices, and other features that can impart structural imperfections that persist as the cement solidifies.

The modified implant would resemble the unmodified implant except that its stem would not be entirely solid; the modified implant would contain a lengthwise hole. The gap between the stem of the implant and the bone would be plugged so that the cement could not escape there, then the implant would be pushed slowly into the cement-filled cavity. The excess cement would be forced to flow out through the lengthwise hole. There would be less flow between the cavity wall and the outer surface of the modified insert than in the case of the unmodified insert. Thus, the unfavorable flow patterns and the resulting structural imperfections should be reduced.



The Lengthwise Hole in the Modified Implant would provide a more favorable flow of bone cement during insertion, reducing the severity of structural imperfections that remain after the flow stops and persist as the cement hardens.

This work was done by Francisco Canabal III of **Marshall Space Flight Center**. *Further information is contained in a TSP [see page 1].*

This invention is owned by NASA, and a patent application has been filed. Inquiries concerning nonexclusive or exclusive license for its commercial development should be addressed to the Patent Counsel, Marshall Space Flight Center [see page 1]. Refer to MFS-28987.

Portable Immune-Assessment System

A portable immune-assessment system has been developed for use in rapidly identifying infections or a contaminated environment. The system combines a few specific fluorescent reagents for identifying immune-cell dysfunction, toxic substances, buildup of microbial antigens or microbial growth, and potential identification of pathogenic microorganisms using a fluorescent microplate reader linked to a laptop computer. The unique feature of the fluorescent-based analysis system is that by using a few specific dyes for cell metabolism, DNA/RNA conjugation, specific enzyme activity, or cell constituents, one can make an immediate, onsite determination of a person's health or of contamination of the environment.

This work was done by Duane L. Pierson of **Johnson Space Center**, *and Raymond P. Stowe and Saroj K. Mishra of KRUG Life Sciences. Further information is contained in a TSP [see page 1].*
MSC-22399

END

DATE FILMED

01/25/96